Measurements of $\mathcal{B}(D_s \to \ell\nu_\ell)$ and f_{D_s} using data collected from the BaBar experiment.

Aidan Randle-Conde
School of Engineering and Design
Brunel University

June 2010

Thesis submitted to Brunel University for the degree of Doctor of Philosophy

Abstract

This thesis presents measurements of the branching fractions $\mathcal{B}(D_s \to \ell\nu_\ell)$ and measurements of the pseudoscalar decay constant, f_{D_s}, using all the data acquired at the BaBar detector at SLAC National Accelerator Laboratory, which were collected from September 1999 to April 2007, and comprised $531\,\text{fb}^{-1}$. The following measurements are made: $\mathcal{B}(D_s \to \mu\nu_\mu) = (6.11 \pm 0.38 \pm 0.33) \times 10^{-3}$, $\mathcal{B}(D_s \to \tau\nu_\tau) = (5.06 \pm 0.34 \pm 0.50) \times 10^{-2}$, and a limit $\mathcal{B}(D_s \to e\nu_e) < 1.46 \times 10^{-4}$ is obtained. Using these measurements a value of $f_{D_s} = 252 \pm 6 \pm 7 \pm 1\,\text{MeV}$ is obtained, where the first uncertainties account for the statistical limitations of the data, the second uncertainties account for the systematic uncertainties, and the third uncertainties account for uncertainties associated with other physical constants (dominated by the lifetime of the D_s meson).

Declaration

This thesis contains original research using data obtained by the BaBar detector at the SLAC National Accelerator Laboratory. The author's work includes reconstruction of the final states and the subsequent determination of the branching fractions and values of f_{D_s}.

The reconstruction and optimisation of the tag D mesons and Λ_c baryons were performed by Graham Jackson. The reconstruction and optimisation of the $DKX\gamma$ system and the measurement of the yield of D_s mesons were performed by Jose Benitez.

Assistance and advice were provided by Drs Jonathon Coleman, Mark Convery, Shane Curry, William Dunwoodie, George Lafferty, Owen Long, and Steve Sekula. Further assistance was provided by Drs Elisa Guido, Nicola Neri, Milind Purohit, and Abi Soffer.

The following software was used in this analysis, but was not developed by any of the analysts: `ROOT`, the beta framework, `Roofit`, `StatPatternRecognition`. The analysts (Jose Benitez, Graham Jackson and the author) wrote the `DRecoilToolsUser` package in its entirety for this analysis.

The study of radiation damage to the electromagnetic calorimeter is original research. The author did not contribute to the design or assembly of the radFET system, nor to the design, assembly or maintenance of the electromagnetic calorimeter.

In addition to the research concerning the branching fractions $\mathcal{B}(D_s \to \ell\nu_\ell)$ and the radFET study, the author also contributed to the events selection and documentation for a study of $\mathcal{B}(B \to \tau\nu_\tau)$.

Acknowledgements

'These points of data make a beautiful line.

And we're out of beta, we're releasing on time'

Still alive, Jonathon Coulton

Special thanks go to Drs Francois Le Diberder and Mike Roney for making the final five months at SLAC possible. I am forever grateful for this chance. Thanks also go to the Science and Technology Facilities Council for funding this adventure, and to Susan Blackwell and Geraldine Burgess.

I am extremely grateful to the following people for their assistance with the work presented thesis:

- Jose, who has been invaluable form start to finish.
- Graham, you helped me far more than you'll ever realise.
- Katie, for keeping it real with the K^0_S mesons. Stay in particle physics, K?
- Steve, the first person I met at SLAC, and a constant source of inspiration. We'll do great things together.
- Akram, for all your supervisory help.
- Profs Tony Doyle, Peter Hobson, and John Stonham for a lively viva.
- Matt, who taught me (nearly) everything I needed to know about BaBar.
- Jong and Martin for help with the radFETs.
- Silke, you never ceased to amaze me.

I'm also grateful for the people who kept him sane throughout the whole process:

- Manuel, thanks for letting me drag you to the craziest places I've ever seen.
- Eugenia, the pinkest physicist I know.
- Wells, you'll owe me $20 yet! Well done with SASS.
- The SLAC crew (Andy, Brad, Corry, David, Debbie, Ellie, Jack, Jean, Jeff, Jen, Jim, Kevin, Kim, Mark, Michael, Sudan, Tim, Tom, and anyone else I missed.)
- The UCL crowd.
- Jack and Gwen, for helping with the transition to CERN.

And some older friends still:

- Dad, Mum, Jon, and Grandma, obviously.
- Layla, Dylan, and Rhiannon. Three of the most creative, bizarre and lovely siblings I could hope for.
- The Oxford old guard, who were always there when I needed them the most.
- Rami, without whom I would have been completely lost these past few years.
- Jeremy, for finding me a home and keeping it warm.
- Dougie, for all your help and support in the final few weeks.
- Phill, one of the warmest, most honest and funniest people I've ever met. You brightened up my time at Brunel.
- Rach, you were there in the first shaky days of B_s^0 mixing and made it a whole lot more fun.
- Nik and Michael, for allowing me to pay rent in the form of chocolate and wine.

The teachers who inspired me: Maggie Miller, Mark Ingham, Dorothy Grundy, Lance Marsden, Steve Jones, Peter Read and Justin Wark.

This thesis is dedicated to the memory of Dylan Graham Randle-Conde. Though he would not understand the content, he would be happy knowing that I got to explore California under the guise of 'hard sums', and that I had a change to glimpse at the mysteries of reality. I know you'd be proud of the life I've lived since you left us.

Contents

List of Tables

List of Figures

Chapter 1

Introduction

This thesis presents measurements of the branching fractions $\mathcal{B}(D_s \to \ell\nu_\ell)$ and a study of the dose absorbed by the electromagnetic calorimeter at BaBar. Chapters 2 and 3 introduce the theory relevant to the branching fraction studies. Chapter 2 gives an overview of the Standard Model of particle physics in its current state. Chapter 3 describes the motivation behind the study of the branching fractions presented, with a review of the current experimental and theoretical status of the measurements.

Chapter 4 describes the BaBar detector, its components and operation, as well as a summary of the data collected. Chapter 5 describes the study of the dose absorbed by the electromagnetic calorimeter of BaBar detector.

Chapter 6 outlines techniques used in the analysis. Chapters 7 and 8 describe the details of the event reconstruction and yield extraction. Chapter 9 gives the systematic uncertainties and the validation studies that were performed for the branching fraction studies.

Chapter 10 summarises the results with the uncertainties and gives interpretations of these results. Chapter 11 concludes the work and provides a context and outlook for the results of the research.

The analysis technique used for the determination of $\mathcal{B}(D_s \to \ell\nu_\ell)$ is a novel approach for the BaBar experiment, requiring sophisticated reconstruction techniques of charm quark hadronisation events.

Charge conjugation is implied throughout this thesis, unless otherwise noted.

Chapter 2

The Standard Model

2.1 Overview

This purpose of this chapter is to outline the theory and models used to describe interactions of particles according the Standard Model of particle physics. This chapter introduces the forces and particles of the Standard Model and explains how these give rise to the phenomena seen in experiment from first principles, giving a suitable review for readers not familiar with the Standard Model. In addition this chapter introduces concepts which inform the analysis strategy, as well as providing some background information relevant to the BaBar experiment as a whole.

2.2 Historical background

The Standard Model describes the interactions of fundamental particles. The history of modern particle physics dates back to 1897 when the electron was discovered in cathode ray tube experiments (Thomson 1897). In the following years this discovery was followed by the observation of the proton, neutron and neutrino in 1919 (Rutherford 1919), 1932 (Chadwick 1932), and 1956 (Cowan 1956). In 1932 the positron was first seen (Anderson 1933), confirming the existence of antimatter, as predicted by the Dirac equation (Dirac 1928). The discoveries of the muon in 1936 (Street 1937) during experiments with cosmic rays provoked much discussion. It was established that the muon had similar properties to the electron and was the first observation of the second generation of matter. The following decades saw the discoveries of additional mesons and baryons. In 1956 Lee showed that certain de-

cays violated parity (Lee 1956), which was followed by the discovery of charge-parity violating interactions in the neutral kaon system in 1964 (Wu 1964). With a growing number of observed baryonic and mesonic states, theorists developed the parton model of hadronic matter, where each baryon is composed of three valence quarks and each meson is composed of valence quark-antiquark pairs (Feynman 1969). In recent decades six quarks and six leptons have been discovered, as well as four gauge bosons (Amsler 2008*b*).

2.3 The forces

There are three fundamental forces in the Standard Model, which are the strong, the weak and the electromagnetic. The strong force couples to colour. The electromagnetic force couples to charge. The weak force couples to weak isospin. Gravity plays no role in the Standard Model.

2.3.1 Relative couplings

In the Standard Model the forces each have a characteristic running coupling. The relative coupling strengths are a non-trivial function of energy of a system. A useful way to compare the relative couplings of the forces is by comparing the values of α_s, α_{em} and α_w, which are the strong coupling, electromagnetic coupling and weak coupling. The strong coupling is conventionally written as $\alpha_s(\mu)$, where μ is a mass scale. At a mass scale of $\mu = 10\,\mathrm{GeVc}^{-2}$ the strong coupling is $\alpha_s \simeq 0.175$ (Amsler 2008*b*). At similar energies the electromagnetic coupling is $\alpha_{em} \simeq 7.30 \times 10^{-3}$ and the weak coupling is $\alpha_w \simeq 1.17 \times 10^{-3}$.

2.4 The fermions

In the Standard Model there are twelve fundamental fermions which are arranged in three generations. This arrangement is phenomenological and is not predicted by theory. The fermions are further divided into quarks and leptons.

2.4.1 Quarks

Quarks interact via the strong, weak and electromagnetic forces. The two lightest quarks are the up quark (u) and the down quark (d). The remaining four quarks are

the charm quark (c) and the top quark (t) which are up-type, and the strange quark (s) and the bottom quark (b) which are down-type. The properties of the quarks are given in table 2.1.

Table 2.1: Properties of the quarks (Amsler 2008*b*).

Quark	Charge (e)	Approximate mass (GeVc^{-2})
u	$\frac{1}{3}$	$(1.5 - 3.3) \times 10^{-3}$
c	$\frac{1}{3}$	$1.16 - 1.34$
t	$\frac{1}{3}$	$169 - 173$
d	$-\frac{2}{3}$	$(3.5 - 6.0) \times 10^{-3}$
s	$-\frac{2}{3}$	$0.07 - 0.13$
b	$-\frac{2}{3}$	$4.13 - 4.37$

2.4.2 Leptons

Leptons do not interact via the strong force. The leptons are further divided into charged leptons (which interact via the weak and electromagnetic forces) and the neutrinos (which interact via the weak force). The properties of the leptons are given in table 2.2.

Charged leptons

The charged leptons are the electron (e), muon (μ) and tau (τ). The principle of leptonic universality states that (aside from mass effects) the couplings of the interactions of the three different leptons with the gauge bosons and other fermions are independent of the generation of the lepton. To date no violation of the principle of leptonic universality has been observed (Amsler 2008*b*). In the limit where the masses of the electron and muon are small compared to the mass of the $\Upsilon(1S)$ meson ($m_{\Upsilon(1S)} = 9460.3 \pm 0.3\,\mathrm{MeV}$ (Amsler 2008*b*)), the ratio of the branching fractions $R_{e\mu} = \mathcal{B}(\Upsilon(1S) \to e^+e^-)/\mathcal{B}(\Upsilon(1S) \to \mu^+\mu^-)$ should be equal to unity. Current measurements give $R_{e\mu} = 0.96 \pm 0.05$ (Kobel 1992). The current limits on lepton family violation include $\mathcal{B}(\mu \to e\gamma) < 1.2 \times 10^{-11}$ (Brooks 1999), $\mathcal{B}(\tau \to e\gamma) < 1.1 \times 10^{-7}$ (Hayasaka 2008) and $\mathcal{B}(\tau \to \mu\gamma) < 4.5 \times 10^{-8}$ (Hayasaka 2006).

Neutrinos

Neutrinos have no charge and therefore do not interact via the electromagnetic interaction. The masses of the neutrinos are very small and (to a good approximation in experiments with charged leptons and quarks) can be ignored. Interactions between neutrinos and other matter are extremely rare.

There are three flavour eigenstates of neutrino: electron neutrino (ν_e), muon neutrino (ν_μ) and tau neutrino (ν_τ). Lepton flavour is conserved in all Standard Model interactions. The flavour eigenstates of the neutrinos are not the mass eigenstates of the neutrinos, so neutrinos can change flavour while in flight. This process is known as neutrino mixing.

Table 2.2: Properties of the leptons (Amsler 2008*b*).

Lepton	Charge (e)	Mass (GeVc^{-2})
e^-	-1	$(5.11 \times 10^{-4}) \pm (1.3 \times 10^{-11})$
μ^-	-1	$(0.105) \pm (4 \times 10^{-9})$
τ^-	-1	$(1.78) \pm (1.7 \times 10^{-4})$
ν_e	0	$< 1 \times 10^{-9}$
ν_μ	0	$< 1 \times 10^{-9}$
ν_τ	0	$< 1 \times 10^{-9}$

2.5 The gauge bosons

The gauge bosons mediate the interactions of particles. To date there are four known gauge bosons and these are listed in table 2.3.

2.5.1 Gluons

Gluons mediate the strong force. There are eight gluons which form an SU(3) multiplet. The gluons themselves are coloured, leading to self-coupling. Gluons are massless in the standard model. Due to the self-coupling nature of the gluons the strong force is short-range.

2.5.2 Photons

The electromagnetic force is mediated by photons, which couple to charge. The photons are massless as required by gauge invariance. The photons do not carry charge, so there is no self coupling and the electromagnetic force is a long range force. The symmetries of electromagnetism forms a U(1) group.

2.5.3 Massive weak bosons

The weak force is mediated by the massive weak bosons, $W^{\pm}$ and Z^0. The $W^{\pm}$ boson is charged so interactions between a quark and a $W^{\pm}$ will always change the flavour of the quark. Similarly interactions between a lepton and a $W^{\pm}$ will always change the charge of the lepton. In the Standard Model the Z^0 cannot change the flavour of any particles.

Table 2.3: Properties of the gauge bosons (Amsler 2008*b*). (A small gluon mass is not precluded.)

Force	Boson	Charge (e)	Mass (GeVc^{-2})
Strong	g	0	0 (Theoretical)
Electromagnetic	γ	0	$< 1 \times 10^{-27}$
Weak	Z	0	91.2 ± 0.002
	$W^{\pm}$	± 1	80.4 ± 0.03

2.6 Quantum mechanics

The Standard Model relies on the frameworks of quantum mechanics and group theory. Interactions are represented by transitions of wavefunctions and symmetries are represented by properties of groups.

2.6.1 Symmetries

The Standard Model is expected to show certain symmetries under certain conditions. Each symmetry arises from invariance under a given transformation. Neother's theorem states that if a symmetry exists there is (in general) an observable quantity which remains constant under the transformation (Noether 1918).

Parity

The strong and electromagnetic forces are invariant under a parity transformation, P, which inverts spatial coordinates:

$$P : \underline{r} \rightarrow \underline{r}' = -\underline{r} \tag{2.1}$$

Since a system must be unchanged under two parity transformations, the eigenvalues of the parity transformation are ± 1. The eigenvalues of angular momentum (defined as $L = \underline{r} \times \underline{p}$) are eigenstates of parity. The parity of a state with total angular momentum L is:

$$P = (-1)^L \tag{2.2}$$

Charge conjugation

Charge conjugation refers to the changing of the signs of the electric charges of a system. The strong and electromagnetic forces are invariant under the charge conjugation transformation, C.

Since both P and C are multiplicative transformations they can be applied in succession to give a CP transformation. Under certain circumstances CP symmetry is violated.

2.6.2 Lagrangian mechanics

For a system of a finite number of particles the time evolution can be determined using the Euler-Lagrange condition. For a given Lagrangian functional, L, with known boundary conditions, in parameter space with coordinates q the Euler-Lagrange condition gives:

$$\frac{\partial L}{\partial q} = \frac{\mathrm{d}}{\mathrm{d}t}\left(\frac{\partial L}{\partial \dot{q}}\right) \tag{2.3}$$

where $\dot{q}$ is the time derivative of the coordinate q. The action, defined as $s = \int L \mathrm{d}t$ is extremal.

In the absence of interactions the Lagrangian functional for a given field, ϕ, is:

$$L = \frac{1}{2}\partial_\mu \phi \partial^\mu \phi - \frac{1}{2}m^2\phi^2 \tag{2.4}$$

where the Einstein summation convention is assumed over the index μ and m is the mass of the particle associated with the field.

The Hamiltonian functional, H, is related to the Lagrangian functional by:

$$H = L - p\dot{q} \tag{2.5}$$

where p is the conjugate momentum of the coordinate q. The Hamiltonian functional will then describe the energy of the system, so for energy eigenstates it will be invariant with respect to time. The Lagrangian is a Lorentz invariant quantity, whereas the Hamiltonian is not Lorentz invariant.

2.6.3 Lorentz invariant wave equations

In the Standard Model particles can be represented by wavefunctions. These equations must be invariant under the Poincaré group of transformations.

Properties of the wavefunctions

The wavefunction represents a probability density for the particle at a given point in spacetime. The probability density, ρ, is given by the square of the wavefunction, ψ. In Dirac bra-ket notation:

$$\rho = \langle \psi^{\star} | \psi \rangle \tag{2.6}$$

where ρ is the time component of the four-vector probability current, j.

A wavefunction is an eigenfunction of a operator, $\hat{A}$, with an eigenvalue a if $\hat{A}|\psi\rangle = a|\psi\rangle$.

A wavefunction can be expressed as a superposition of orthonormal basis states. The wavefunction can then 'mix' between more than one orthonormal base states.

The wavefunction exists in a conjugate space where the momenta of the particles is determined by the spatial derivatives of the wavefunction. The momentum operator is $\hat{p}^{\mu} = -i\hbar\frac{\partial}{\partial x_{\mu}}$, and other mechanical operators take analogous forms.

The Dirac equation

Particles can be described by the Dirac equation acting on a field ψ:

$$i\frac{\partial \psi}{\partial t} = \left(-i \cdot \alpha\nabla + \beta m\right)\psi \tag{2.7}$$

Since the solutions to the Dirac equations are invariant under rotation, one would expect that the angular momentum of the wavefunction be constant in the absence

of interactions, in accordance with Noether's theorem:

$$[\hat{H}, \hat{J}] = 0 \tag{2.8}$$

where $\hat{J}$ is the angular momentum operator.

However if one takes the classical definition of orbital angular momentum, $\hat{L} = \hat{r} \times \hat{p}$, then the commutation relation becomes non-zero:

$$\begin{aligned} [\hat{L}, \hat{H}] &= [\hat{R} \times \hat{p}, \hat{\alpha} \cdot \hat{p}] && (2.9) \\ &= [\hat{r}, \hat{\alpha} \cdot \hat{p}] \times \hat{p} && (2.10) \\ &= i\hat{\alpha} \times \hat{p} && (2.11) \end{aligned}$$

In order to preserve conservation of angular momentum there must be another quantity, $\hat{S}$, such that $\hat{J} = \hat{L} + \hat{S}$. This angular momentum is an inherent property of the wavefunction of the particle and is referred to as spin. Fermions have half integer spin and bosons have integer spin. Fermions can be described by Fermi-Dirac statistics, where the wavefunctions of identical particles are antisymmetric with respect to exchange. Bosons can be described by Bose-Einstein statistics, where the wavefunctions of particles are symmetric with respect to exchange.

Choice of picture

In general, both the wavefunction of a system of particles and the associated eigenvalues of operators will have a time dependence. The choice of basis states for the wavefunctions determines how this time dependence is expressed. In the Standard Model the interaction picture is used where time evolution of the system is described by a matrix which relates the wavefuntions to each other. This matrix is called the S matrix. This picture has the advantage that the time evolution of the interaction potential is included in the definition of the field, ϕ.

Antiparticles

For each particle in the Standard Model there is a corresponding antiparticle. The state of an antiparticle is obtained by performing a charge-conjugation and parity transformation on the wavefunction of a particle. In addition to the 12 known fermions (u, d, c, s, t, b, e^-, ν_e, μ^-, ν_μ, τ^-, ν_τ) there are 12 antifermions ($\bar{u}$, $\bar{d}$, $\bar{c}$, $\bar{s}$, $\bar{t}$, $\bar{b}$, e^+, $\bar{\nu}_e$, μ^+, $\bar{\nu}_\mu$, τ^+, $\bar{\nu}_\tau$). The internal numbers of antiparticles are of the opposite sign of

those of the corresponding particles.

2.6.4 Electromagnetism

The electromagnetic interaction couples charges in a one dimensional charge space. Therefore the operators representing electromagnetic interactions can be characterised by the group of U(1) transformations. The U(1) group has a single member which takes the form $U_1(\theta) = \mathrm{e}^{i\theta}$. Under this transformation the wavefunction, ψ, gains a complex phase:

$$\psi \rightarrow U_i(\theta)\psi = \mathrm{e}^{i\theta}\psi \tag{2.12}$$

If θ is a function of position, x, then the momentum operator, $\hat{p}_\mu = -i\hbar\partial_\mu$, is no longer invariant with respect to such a gauge transformation:

$$\begin{aligned} \hat{p}_\mu\psi &= -i\hbar\partial_\mu\psi & (2.13)\\ \hat{p}_\mu\psi' &= -\mathrm{e}^{i\theta}i\hbar\partial_\mu\psi + \hbar\partial_\mu\theta\mathrm{e}^{i\theta}\psi & (2.14)\\ &\neq \hat{p}_\mu\psi & (2.15) \end{aligned}$$

Local gauge invariance requires the introduction of a field to accommodate such transformations and this field is the electromagnetic field, A_μ, which transforms under a gauge transformation, with a covariant derivative, D_μ, as:

$$\begin{aligned} A'_\mu &= A_\mu - \partial_\mu\alpha(\underline{r}) & (2.16)\\ \partial_\mu \rightarrow D_\mu &= \partial_\mu - iqA_\mu & (2.17) \end{aligned}$$

2.6.5 Quantum chromodynamics

In quantum chromodynamics (QCD) there are three basis vectors which represent the three strong force colours, r, g, b. The number of colours is determined experimentally. The operations which transform one vector to another form an SU(3) group. Combining the vectors gives nine possible interactions, which separate into an octet and a non-interacting singlet.

A common choice of representation of generators for the octet is the Gell-Mann matrices, λ_i, given in table 2.4. These matrices represent the exchange of gluons. In this choice of representation the three colours form the fundamental representation with $r = |100\rangle$, $g = |010\rangle$ and $b = |001\rangle$.

Table 2.4: The Gell-Mann matrices.

$$\lambda_1 = \begin{pmatrix} 0 & 1 & 0 \\ 1 & 0 & 0 \\ 0 & 0 & 0 \end{pmatrix} \quad \lambda_2 = \begin{pmatrix} 0 & -i & 0 \\ i & 0 & 0 \\ 0 & 0 & 0 \end{pmatrix} \quad \lambda_3 = \begin{pmatrix} 1 & 0 & 0 \\ 0 & -1 & 0 \\ 0 & 0 & 0 \end{pmatrix}$$

$$\lambda_4 = \begin{pmatrix} 0 & 0 & 1 \\ 0 & 0 & 0 \\ 1 & 0 & 0 \end{pmatrix} \quad \lambda_5 = \begin{pmatrix} 0 & 0 & -i \\ 0 & 0 & 0 \\ i & 0 & 0 \end{pmatrix}$$

$$\lambda_6 = \begin{pmatrix} 0 & 0 & 0 \\ 0 & 0 & 1 \\ 0 & 1 & 0 \end{pmatrix} \quad \lambda_7 = \begin{pmatrix} 0 & 0 & 0 \\ 0 & 0 & -i \\ 0 & i & 0 \end{pmatrix} \quad \lambda_8 = \frac{1}{\sqrt{3}} \begin{pmatrix} 1 & 0 & 0 \\ 0 & 1 & 0 \\ 0 & 0 & -2 \end{pmatrix}$$

To ensure gauge invariance the covariant derivative transforms as:

$$D_\mu = \partial_\mu - iX_a G^a_\mu \tag{2.18}$$

SU(3) is not an Abelian group, so in general the operators do not commute. This leads to commutation terms which do not vanish, leading to triple and quartic couplings. The gluons exhibit self-coupling, which when combined with the coupling strength of the strong force leads to confinement; it takes an infinite amount of energy to separate two coloured objects in such a way as to create net colour locally. (In such a situation a quark-antiquark pair is produced and the system will evolve into another state.)

Quark systems

Since there are no isolated coloured systems in the Standard Model and quarks carry colour there must be systems of quarks which are allowed and systems of quarks which are forbidden in the Standard Model. Recalling that antiparticles and particles have opposite internal numbers means that a quark-antiquark system can have zero net colour, such as in the state $|q'\rangle|\bar{q}\rangle$, with colour wavefunction $|r\rangle|\bar{r}\rangle$. Similarly a system of three quarks can have zero net colour, such as in the state $|q\rangle|q'\rangle|q''\rangle$, with colour wavefunction $|r\rangle|g\rangle|b\rangle$. In the quark model systems are limited to those which are comprised of combinations of $q\bar{q}$ systems (mesons) and qqq systems (baryons)

(Amsler 2008*b*). Although exotic systems such as $qqqq\bar{q}$ and $q\bar{q}q\bar{q}$ are allowed in the Standard Model, there is no compelling evidence of such systems existing (Amsler 2008*c*).

The lowest mass baryonic states in the Standard Model are the proton (p) and the neutron (n) with quark content uud and udd respectively. The wavefunctions of the quarks can be expressed as a product of the space, flavour, spin and colour parts:

$$\psi = \psi(r)\psi_{flavour}\chi_{spin}\psi_{colour} \tag{2.19}$$

There is a particle with larger mass, a spin of 3/2 and quark content uuu, called the Δ^{++}. Since its spatial, spin and flavour wavefunctions are symmetric with respect to exchange of up quarks the colour part of the wavefunction must be antisymmetric with respect to exchange of quarks.

2.6.6 Quark flavour in mesons

Isospin

The two lightest quarks (u and d) have small masses compared to the masses of the lightest quark-antiquark systems. As the strong force is independent of the flavour of the quarks the up and down quark doublet (u, d) exhibits a useful symmetry with eigenvalues of isospin $(1/2, -1/2)$. This symmetry is formally known as isospin and it is almost exact. It can be characterised by the SU(2) group of transformations, which has 3 generators. The four states form an isospin triplet and a singlet. The states are identified in terms of overall isospin, I, and the third component of isopsin, I_3, which in this choice of representation commutes with I. Combining the (u, d) doublet with its partner $(\bar{d}, -\bar{u})$ gives the isospin eigenstates, as shown in table 2.5. The three pions (π^+, π^0, π^-) are the lightest mesons. The other state, η_3, is not observed in experiment.

SU(n) flavour mesons

More flavours of quarks can be added to form different symmetry groups, but as the quark mass terms become progressively larger the symmetry becomes progressively more broken. Extending the symmetry group to include the strange quark gives nine mesons which are arranged in an SU(3) octet and a singlet. The third and eighth Gell-Mann matrices commute, giving two observable quantum numbers and two states

Table 2.5: Properties of the SU(2) flavour group of ground state mesons.

State	I	I_3	Meson	Mass ($\mathrm{MeVc^{-2}}$)
$u\bar{d}$	1	1	π^+	139
$\frac{1}{\sqrt{2}}\left(u\bar{u}-d\bar{d}\right)$	1	0	π^0	135
$d\bar{d}$	1	-1	π^-	139
$\frac{1}{\sqrt{2}}\left(u\bar{u}+d\bar{d}\right)$	0	0	η_3	

Table 2.6: Properties of the SU(3) flavour group of ground state mesons.

State	I	I_3	S	Meson	Mass ($\mathrm{MeVc^{-2}}$)
$u\bar{s}$	1/2	1/2	1	K^+	494
$d\bar{s}$	1/2	$-1/2$	1	K^0	498
$u\bar{d}$	1	1	0	π^+	139
$\frac{1}{\sqrt{2}}\left(u\bar{u}-d\bar{d}\right)$	1	0	0	π^0	135
$d\bar{d}$	1	-1	0	π^-	139
$s\bar{d}$	1/2	1/2	-1	$\bar{K^0}$	498
$s\bar{u}$	1/2	$-1/2$	-1	K^-	494
$\frac{1}{\sqrt{2}}\left(u\bar{u}+d\bar{d}+s\bar{s}\right)$	0	0	0	η_3	
$\frac{1}{\sqrt{6}}\left(u\bar{u}+d\bar{d}-2s\bar{s}\right)$	0	0	0	η_8	

with the same quantum numbers. This allows wavefunctions which overlap with two of the states, leading to mixing.

Identifying the strangeness, S, with the presence of an $\bar{s}$ quark gives the states shown in table 2.6. This set of mesons contains the isospin triplet as a subset. Four new states are identified as the charged and neutral kaons. The final two states, η_3 and η_8, are not mass eigenstates. They mix to form the η ($m_\eta \sim 548\,\mathrm{MeVc^{-2}}$) and the η' ($m_{\eta'} \sim 958\,\mathrm{MeVc^{-2}}$).

In a similar manner, higher energy mesons states can be constructed with larger angular momenta. Extending this model to include the charm quark gives an SU(4) representation, as shown in figure 2.1. This model can likewise be extended to SU(5) to include the bottom mesons, although this is difficult to display in two dimensions.

The lifetime of the top quark is shorter than the lifetime of all known ground state mesons, so forming an SU(6) system of mesons in order to include the top quark is not useful.

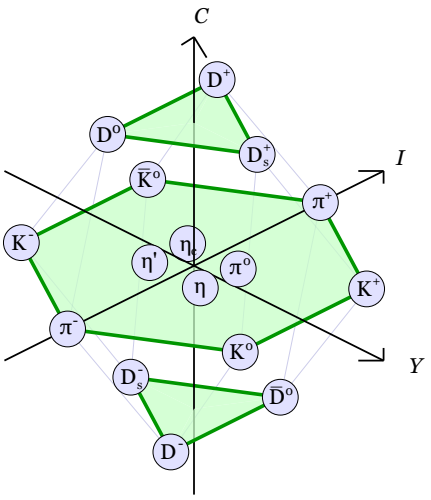

Figure 2.1: The SU(4) group of ground state mesons.

Mesons consistent with the states (or their admixtures) in the SU(5) systems of mesons for angular momentum and parity, $J^P = 0^-, 1^-$, have been observed in experiments (although some states are still awaiting experimental confirmation of their expected angular momentum, J, and parity, P). Other meson states have been observed in experiment and there is ongoing discussion concerning the nature (and in some cases the existence) of some of these states.

At BaBar a large quantity of $\Upsilon(4S)$ mesons were produced. The mass of this meson is $10.58\,\mathrm{GeVc}^{-2}$, which is above the $b\bar{b}$ production threshold, leading to large numbers B mesons being produced.

Baryons

As outlined above the lowest mass baryonic states cannot contain the same flavour for all three quarks. Combining the four lightest quarks using the SU(4) symmetry group gives an icosaplet of baryons. These states are shown in figure 2.2. At the time of writing many of these states are not well understood and their use in analysis should remain tentative. The following particles are listed by the Particle Data Group as "Existence is certain, and properties are at least fairly well explored": p, n, Σ^+, Σ^0,

Σ^-, Λ, Σ_c^{++}, Σ_c^+, Σ_c^0, Σ_c^-, Λ_c^+ (Amsler 2008*b*).

When quarks are created from e^+e^- collisions, to preserve quantum numbers the quarks are always produced in quark-antiquark pairs. Therefore whenever a baryon is produced there must also be an antibaryon present.

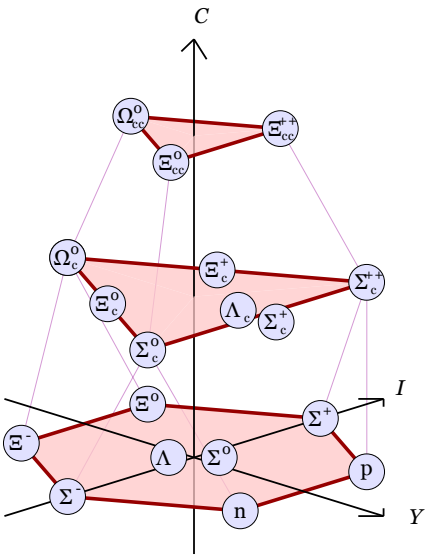

Figure 2.2: The SU(4) group of ground state baryons.

2.6.7 Weak interactions

In analogy to isospin, the weak isospin expresses how the fermions couple to the $W^\pm$ and Z^0 bosons. The fermions form pairs of weak isospin doublets when coupling to the $W^\pm$ boson:

$$\begin{pmatrix} u' \\ d' \end{pmatrix} \begin{pmatrix} c' \\ s' \end{pmatrix} \begin{pmatrix} t' \\ b' \end{pmatrix} \begin{pmatrix} \nu_e \\ e \end{pmatrix} \begin{pmatrix} \nu_\mu \\ \mu \end{pmatrix} \begin{pmatrix} \nu_\tau \\ \tau \end{pmatrix} \tag{2.20}$$

where the u', d', c', s', t' and b' states represent admixtures of pure u, d, c, s, t and b states.

The weak interaction is characterised by the SU(2) group with three generators. These correspond to the W^+, W^- and Z^0 bosons. The representation of the group is chosen such that the up-type quark admixtures are pure quark states ($u' = u$, $c' = c$, $t' = t$).

In the Standard Model the Z^0 boson does not change fermion flavour. The Z^0 boson and the photon have identical quantum numbers, so the amplitudes of the two particles can interfere in interactions.

2.7 Quark mixing and the Cabibbo-Kobayashi-Maskawa matrix

The Cabibbo-Kobayashi-Maskawa matrix describes how the quarks mix when interacting with the $W^{\pm}$ boson (Kobayashi & Maskawa 1973). In the Standard Model the down-like quarks mix according to the Cabibbo-Kobayashi-Maskawa matrix:

$$\begin{pmatrix} d' \\ s' \\ b' \end{pmatrix} = \begin{pmatrix} V_{ud} & V_{us} & V_{ub} \\ V_{cd} & V_{cs} & V_{cb} \\ V_{td} & V_{ts} & V_{tb} \end{pmatrix} \begin{pmatrix} d \\ s \\ b \end{pmatrix} \tag{2.21}$$

where d', s', b' are the weak isospin eigenstates of the quarks and d, s and b are the strong flavour eigenstates of the quarks. In order to preserve normalisation the Cabibbo-Kobayashi-Maskawa matrix must be unitary.

The Cabibbo-Kobayashi-Maskawa matrix can be parameterised by three angles (θ_{12}, θ_{13} and θ_{23}) and one non-vanishing phase (δ):

$$V = \begin{pmatrix} C_{12}C_{13} & S_{12}C_{13} & S_{13}\mathrm{e}^{-i\delta} \\ -S_{12}C_{23} - C_{12}S_{23}S_{13}\mathrm{e}^{i\delta} & C_{12}C_{23} - S_{12}S_{13}S_{23}\mathrm{e}^{i\delta} & S_{23}C_{13} \\ S_{12}S_{23} - C_{12}S_{23}S_{13}\mathrm{e}^{i\delta} & -C_{12}C_{23} - S_{12}S_{13}S_{23}\mathrm{e}^{i\delta} & C_{23}C_{13} \end{pmatrix} \tag{2.22}$$

where $C_{12} = \cos\theta_{12}$, $S_{12} = \sin\theta_{12}$, $C_{13} = \cos\theta_{13}$, $S_{13} = \sin\theta_{13}$, $C_{23} = \cos\theta_{23}$, $S_{23} = \sin\theta_{23}$.

The relative sizes of the matrix elements are found by experiment to be (Amsler

2008*b*):

$$V = \begin{pmatrix} 0.97419 \pm 0.00022 & 0.2257 \pm 0.0010 & 0.00459 \pm 0.00016 \\ 0.2256 \pm 0.0010 & 0.97334 \pm 0.00023 & 0.0415^{+0.0010}_{-0.0011} \\ 0.00874^{+0.00026}_{-0.00037} & 0.0407 \pm 0.0010 & 0.999133^{+0.000044}_{-0.000043} \end{pmatrix} \tag{2.23}$$

A useful parameterisation that shows the relative sizes of the elements (noting that $s_{13} \ll s_{23} \ll s_{12} \ll 1$) is the Wolfenstein parameterisation (Wolfenstein 1983):

$$V = \begin{pmatrix} 1 - \frac{1}{2}\lambda^2 & \lambda & A\lambda^3 (\rho - i\eta) \\ -\lambda & 1 - \frac{1}{2}\lambda^2 & A\lambda^2 \\ A\lambda^3 (1 - \rho - i\eta) & -A\lambda^2 & 1 \end{pmatrix} + O(\lambda^4) + \ldots \tag{2.24}$$

where λ is smaller than 1 and represents the Cabibbo mixing angle for the first two generations of quarks and A, ρ and η are all real and of order 1. ρ and η are approximations of $\bar{\rho}$ and $\bar{\eta}$, which are parameters of the Standard Model, as shown in figure 2.3.

The unitarity condition implies that for any two rows or columns in the Cabibbo-Kobayashi-Maskawa matrix $\sum_i V_{ij} V_{ik}^\star = \delta_{jk}$ and $\sum_j V_{ij} V_{kj}^\star = \delta_{ik}$. A triangle can be constructed on the complex plane using this condition. The most commonly chosen condition is $V_{ud} V_{ub}^\star + V_{cd} V_{cb}^\star + V_{td} V_{tb}^\star = 0$. Dividing through by $|V_{cd} V_{cb}^\star|$ gives a triangle with vertices $(0,0)$, $(1,0)$, $(\bar{\rho}, \bar{\eta})$, as shown in fig 2.3. The three angles are then $\alpha = \arg\left(-\frac{V_{td} V_{tb}^\star}{V_{ud} V_{ub}^\star}\right)$, $\beta = \arg\left(-\frac{V_{cd} V_{cb}^\star}{V_{ud} V_{ub}^\star}\right)$, $\gamma = \arg\left(-\frac{V_{ud} V_{ub}^\star}{V_{cd} V_{cb}^\star}\right)$.

Experimental results can be used to overconstrain the unitarity triangle. If the triangle does not converge to a single apex at $(\bar{\rho}, \bar{\eta})$ this implies that there are new physics processes beyond the Standard Model. Current measurements of the Cabibbo-Kobayashi-Maskawa parameters provide no clear evidence of such effects.

2.7.1 Flavour mixing

The quark content of neutral mesons can change in time as interactions with $W^\pm$ boson change the flavour of quarks. This process is known as flavour oscillation. Flavour oscillation has been observed in all neutral mesons containing s, c or b quarks.

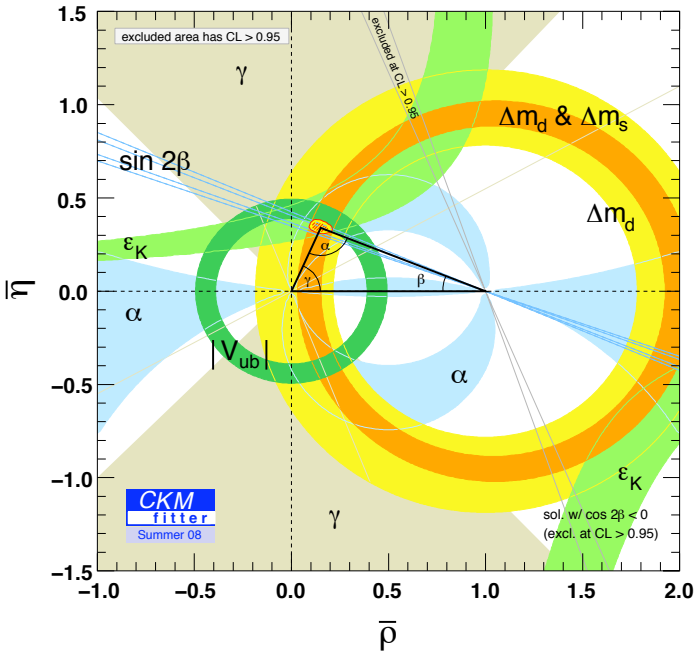

Figure 2.3: The CKMFitter global fit to the unitary triangle. (Charles 2005)

Flavour oscillation involving c and b quarks, although theoretically very interesting, are not a significant factor in this analysis.

The neutral kaon system

The neutral kaons decay via the weak interaction. Experiments show that the states of the neutral kaons in flight are almost pure CP eigenstates and are not eigenstates of quark flavour. Figure (2.4) shows the Standard Model processes which give flavour mixing in the neutral kaon system. The two observed neutral kaon states are labelled K_S^0, which has a lifetime of $8.953(5) \times 10^{-11}$ s, and K_L^0, which has a lifetime of $5.116(20) \times 10^{8}$ s. If CP effects are negligible then the CP eigenstates can be used to represent neutral kaons. These states are found to show maximal strangeness mixing:

$$|K_L^0\rangle \simeq |K_{CP-odd}\rangle = \frac{1}{\sqrt{2}}\left(|K^0\rangle + |\bar{K}^0\rangle\right) \tag{2.25}$$

$$|K_S^0\rangle \simeq |K_{CP-even}\rangle = \frac{1}{\sqrt{2}}\left(|K^0\rangle - |\bar{K}^0\rangle\right) \tag{2.26}$$

Therefore it is impossible to determine the strangeness of a neutral kaon at the point of production by observing only the decay products of that meson.

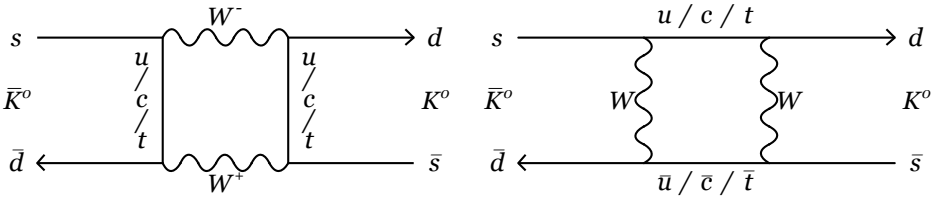

Figure 2.4: Feynman diagram showing neutral kaon oscillations.

2.8 Summary

This chapter has introduced the concepts of the Standard Model which are relevant to this analysis, including the nature of the fundamental fermions and their interactions. The Standard Model provides an excellent description of the interactions of particles and forces. The formalisms of quantum mechanics, group theory and quantum field theory provide an internally consistent framework which respects the Poincaré group of transformation and gauge symmetries, which has been outlined in this chapter. This chapter closed with a discussion of hadronic matter and the Cabibbo-Kobayashi-Maskawa matrix, which describes the content and properties of mesons.

Chapter 3

Leptonic decays of mesons

3.1 Overview

This chapter outlines the motivation for the study of the branching fractions $\mathcal{B}(D_s \to \ell\nu_\ell)$ and the decay constant f_{D_s}. The first section discusses the Standard Model expectation for the branching fractions. A short review of the literature summarises current experimental measurements and theoretical expectations for f_{D_s}. The scope for discovery of new physics is then briefly discussed, and the chapter concludes with remarks about the choice of analyses and the merits of using the BaBar experiment.

3.2 Introduction

The leptonic decays of mesons provide access to experimentally clean measurements of the decay constants of the mesons as well as the relevant Cabibbo-Kobayashi-Maskawa matrix elements. figure 3.1 shows the leading order Standard Model process for the decay of a pseudoscalar meson, D_s to leptons, μ, ν_μ. The final states of leptonic decays are free from hadronic resonances and final state quark-gluon interactions which can make analogous hadronic decay modes difficult to study.

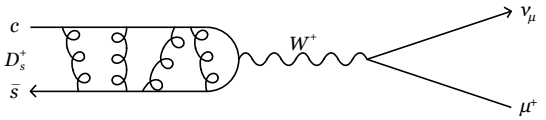

Figure 3.1: Feynman diagram for the decay $D_s \to \mu\nu_\mu$.

In the Standard Model the branching fraction for a charged pseudoscalar meson

(a meson with $J^P = 0^-$), P, to leptons is given by (Amsler 2008*a*):

$$\mathcal{B}(P^+ \to \ell^+ \nu_\ell) = \frac{M_P}{8\pi} f_P^2 G_F^2 |V_{qq'}|^2 m_\ell^2 \left(1 - \frac{m_\ell^2}{M_P^2}\right)^2 \tag{3.1}$$

where M_P is the mass of the meson, m_ℓ is the mass of the charged lepton, f_P is the decay constant of the meson, G_F is the Fermi coupling constant, and $V_{qq'}^\star$ is the Cabibbo-Kobayashi-Maskawa matrix element corresponding to the quark content of the meson. (Here the neutrino in the final state is assumed to be massless.)

3.2.1 Decay constants

The decay constant for a pseudoscalar meson of quark content $q'\bar{q}$ in Dirac Bra-ket notation is

$$\langle 0|q'\gamma_\mu\gamma_5\bar{q}|P(p)\rangle = i f_P p_\mu \tag{3.2}$$

where $\gamma_\mu\gamma_5$ describe the weak current, and p is the momentum of the pseudoscalar meson (Follana 2007). Equation 3.2 relates the decay constant to the overlap of the wavefunctions of the quark-antiquark pair (Bogdan 2008).

3.2.2 Motivation

If the magnitude of the relevant Cabibbo-Kobayashi-Maskawa matrix element is well known then by measuring the leptonic branching fraction of a pseudoscalar meson one can determine the decay constant with high precision. Conversely, if one can precisely estimate the decay constant of a pseudoscalar meson, it is possible to determine the magnitude of the relevant Cabibbo-Kobayashi-Maskawa element.

3.2.3 Current status of experimental theory and theoretical expectations

In recent years, disagreements between experimental results and theoretical expectations in the leptonic decays of heavy flavour mesons have arisen. At the time of writing there is no consensus about the physical processes that contribute to these disagreements.

Recent experimental measurements of f_{D_s}

A number of different experiments have published experimental measurements of f_{D_s}. Figure 3.2 shows recent measurements of f_{D_s} listed by the Particle Data Group, as well as the world average as calculated by the Particle Data Group. Recent publications of experimental results have shown a movement in the world average of f_{D_s} towards the theoretical expectation. However, as the results have moved closer, the uncertainties have become smaller, leading to serious disagreement.

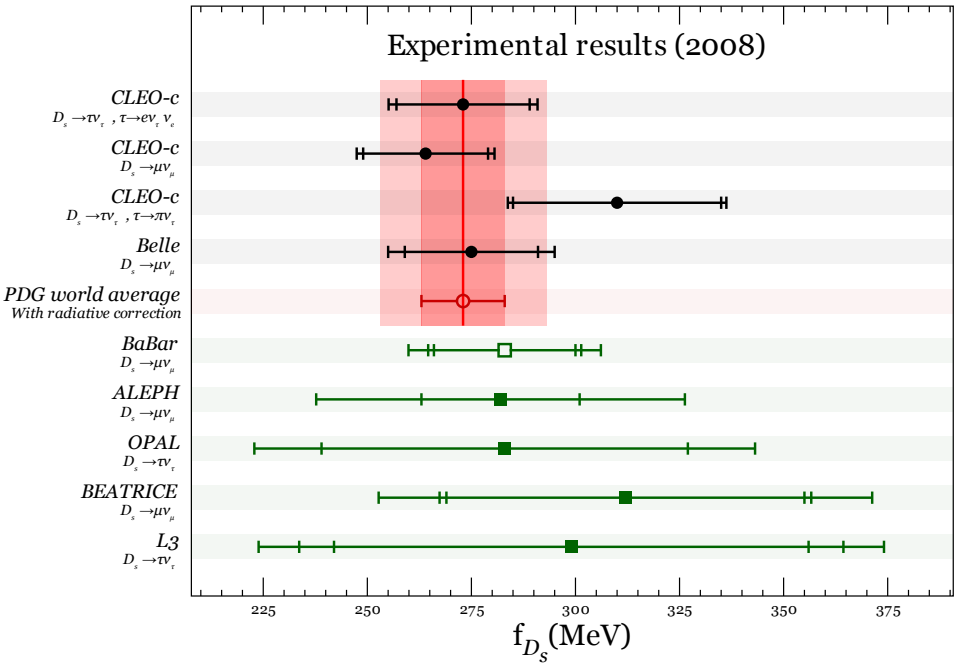

Figure 3.2: Current experimental results for the value of f_{D_s} from various experiments. The Particle Data Group world average is shown in the vertical pink bands. The inner band indicates one standard deviation around the mean value and the outer band indicates two standard deviations around the mean value. Measurements contributing to the world average are shown with solid circles. The world average is shown with a hollow circle. Other measurements are shown with squares. The previous BaBar measurement (which this result supersedes) is shown with a hollow square. The first error bars show the statistical uncertainties for the measurements. The second error bars show the statistical and systematic uncertainties, added in quadrature for the measurements. The third error bars (where present) show the statistical, systematic and normalisation uncertainties, added in quadrature for the measurements. (Ecklund 2008) (Artuso 2007) (Widhalm 2008) (Aubert 2007) (Heister 2002) (Abbiendi 2001) (Alexandrov 2000) (Acciarri 1997)

Recent unquenched lattice quantum chromodynamics calculations

Much work has been already been undertaken to calculate expectations of the decay constants of pseudoscalar mesons using unquenched lattice quantum chromodynamics calculations. Recently, the uncertainties of unquenched lattice quantum chromodynamics calculations have become sensitive to new physics beyond the Standard Model.

Figure 3.3 shows recent theoretical expectations of f_{D_s} from various collaborations. The pink bands show the experimental world average, with the bands demarking one and two standard deviations around the mean. Attention is drawn to the expectation calculated by the HPQCD and UKQCD groups. This expectation differs from the experimental world average by three standard deviations. Using the same technique, the HPQCD and UKQCD groups can calculate an expectation for f_D which agrees very well with the current experimental world average.

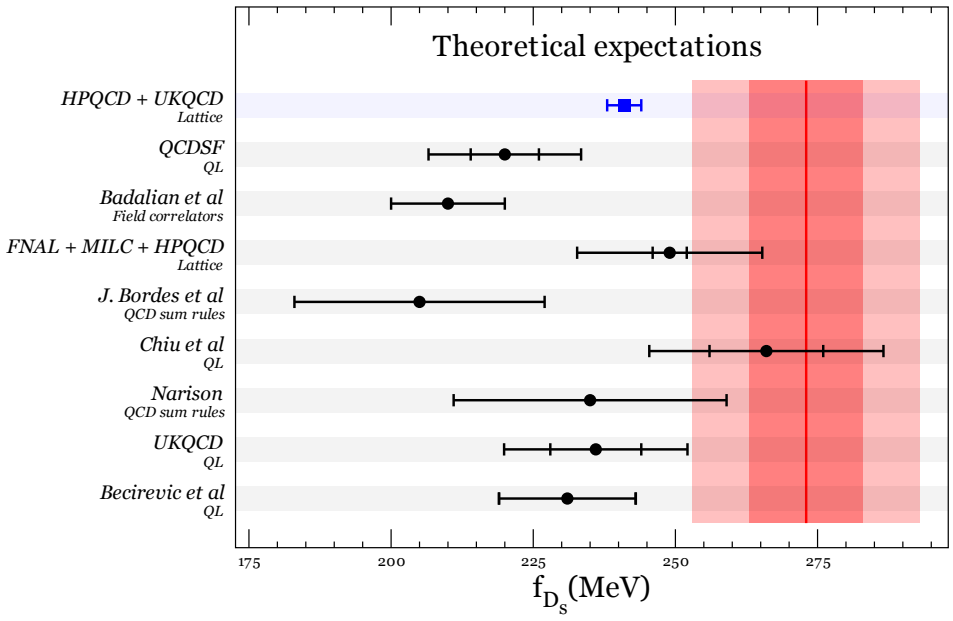

Figure 3.3: Current theoretical expectations for the value of f_{D_s} from various collaborations. The Particle Data Group world average is shown in the vertical pink bands. The inner band indicates one standard deviation around the mean value and the outer band indicates two standard deviations around the mean value. Older expectations are shown with circles. The expectation shown with a blue square denotes a recent result from Follana et al which disagrees with experimental results by three standard deviations. (Follana 2007) (Khan 2007) (Badalian 2007) (Aubin 2005) (Bordes 2005) (Chiu 2005) (Narison 2000) (Lellouch & Lin 2001) (Becirevic 1999)

In 2007 Follana *et al* (Follana 2007) published a new result for the calculation of f_D and f_{D_s} using unquenched lattice quantum chromodynamics calculations. They

give $f_D = 207(4)\,\mathrm{MeV}$ and $f_{D_s} = 241(3)\,\mathrm{MeV}$. Compiling these results alongside recent experimental measurements, Bogdan et al present a discrepancy in excess of 3σ between unquenched lattice quantum chromodynamics calculations and experimental results (Bogdan 2008).

3.3 Sensitivity to new physics

A number of particles have been hypothesised which could affect the branching fractions of leptonic decays of heavy flavour mesons. If one has confidence in unquenched lattice quantum chromodynamics expectations and experimental results, and if the disagreement between them remains, then one must conclude there are effects which the Standard Model with its current parameters cannot explain. Here the author outlines some of the possible hypothesised particles that could account for such a disagreement.

3.3.1 Additional weak bosons

In the Standard Model there is a charged weak boson, $W^{\pm}$, which couples approximately with strength G_F^2. The coupling of the $W^{\pm}$ boson in terms of the weak coupling, g_W, and the mass of the $W^{\pm}$ boson, M_W, is:

$$G_F = \frac{\sqrt{2} g_W^2}{8 M_W^2} \tag{3.3}$$

Additional weak bosons may exist which have the same couplings as the $W^{\pm}$ boson, but a larger mass. Such hypothetical particles are labelled W' and current lower limits on their masses give $M_{W'} > 1000\,\mathrm{GeVc}^{-2}$.(Amsler 2008*b*)

3.3.2 Supersymmetric particles

A supersymmetric model predicts that there are additional particles which can mediate interactions between known particles. Direct searches for supersymmetric particles have yielded large lower limits on mass ($M_\chi > 46\,\mathrm{GeVc}^{-2}$ (95% confidence)). In most supersymmetric models a new quantum number, R, is expected to be preserved, leading to R parity.

3.3.3 Higgs bosons

Although the Standard Model includes a Higgs boson, such a particle has not been observed, despite direct and indirect searches. In an extended supersymmetric formulation (known as the minimal supersymmetric model (Hou 1993)), a charged Higgs boson could couple to the vertices of a leptonic decay of a meson, interfering with the $W^{\pm}$ boson and changing the branching fraction. The coupling of a Higgs boson

is model dependent and whether an interference term enhances or suppresses a given branching fraction depends on the parameters of the associated Higgs field.

In a particular Higgs field model a Higgs boson propagator could interfere with the $W^{\pm}$ boson propagator in the decay of a pseudoscalar meson, P, giving rise to a factor R_H which has the form:

$$R_H = 1 - \tan^2\beta \frac{M_P^2}{m_H^2} \tag{3.4}$$

where $\tan\beta$ is the ratio of the vacuum expectation values of the masses of the charged and neutral Higgs bosons, M_P is the mass of the pseudoscalar meson, and M_H is the mass of the charged Higgs boson. The branching fraction then scales with R_H^2. $\tan\beta$ is a free parameter of the model, giving rise to the possibility of an enhanced or suppressed branching fraction. The model outlined here is known as the minimal supersymmetric model, and the leading order process contributing to $D_s \to \mu\nu_\mu$ is shown in figure 3.4.

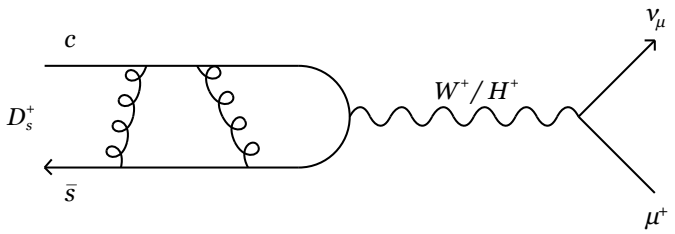

Figure 3.4: Feynman diagram for the decay $D_s \to \mu\nu_\mu$, showing interference from a Higgs particle.

Current limits on the masses of charged Higgs bosons come from direct and indirect searches. Indirect searches include the decay $B \to \tau\nu_\tau$. The current limit on the Higgs boson mass listed by the Particle Data Group is $M_H > 79.3\,\mathrm{GeVc}^{-2}$ (95% confidence) or larger.

3.3.4 Leptoquarks

Leptoquarks are hypothesised particles that could violate quark number and lepton number, but not violate fermion number. A typical leptoquark interaction is shown in fig (3.5). The current lower limit on the masses of first generation pair-produced leptoquarks masses is $M_X > 256\,\mathrm{GeVc}^{-2}$ (95% confidence).

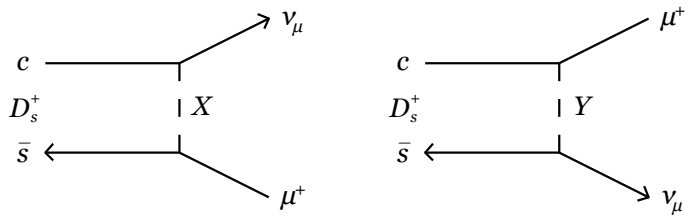

Figure 3.5: Feynman diagram for the decay $D_s \to \mu\nu_\mu$, showing possible contribution from leptoquarks.

Table 3.1: Current limits on hypothesised particles (Amsler 2008*b*).

Particle	Lower limit on mass (GeVc^{-2})
Additional weak bosons	$1000\,\mathrm{GeVc}^{-2}$
Higgs bosons	$79.3\,\mathrm{GeVc}^{-2}$ (95% confidence)
Leptoquarks	$256\,\mathrm{GeVc}^{-2}$ (95% confidence)
Supersymmetric particles	$46\,\mathrm{GeVc}^{-2}$ (95% confidence)

3.3.5 Current limits on hypothesised particles

Many searches for hypothesised particles have been performed (Amsler 2008*b*). The lower limits on masses from direct searches are outlined in table 3.1. At the time of writing these limits reflect the ability of past and present energy frontiers in experiments. The Large Hadron Collider at the European Organization for Nuclear Research (CERN) is expected to provide access to higher energy environments in the near future, allowing direct searches into higher energy regimes. Any interpretation of the current experiment and theoretical status favouring one model over another would be tentative and premature.

3.4 Feasibility of study

The choice of analysis is informed by various factors concerning the feasability of the study. For the analysis to be effective it must be able to provide precise determination of, or stringent limits on the leptonic branching fractions of the D_s meson. This section outlines the various factors which affect the feasability of the analysis.

3.4.1 Kinematic factors

When studying leptonic decays it is desirable to measure a branching fraction that has a final state with a single lepton while also having a statistically significant yield. When considering which mode is optimal it is necessary to consider the kinematic properties of the final state.

Helicity suppression

The decay of a pseudoscalar meson to a leptonic final state exhibits helicity suppression. Helicity suppression arises in the regime where neutrinos are massless, as they will occupy the eigenstates of chirality. The chirality eigenstates refer to the projection of the particle's spin onto its momentum in the rest frame of the parent particle. Ultra relativistic particles occupy the chiral eigenstates. Since the charged lepton has non-negligible mass it is necessarily less relativistic than the neutrino in the meson rest frame. The ratio of helicity suppression is easily predicted in the Standard Model and scales with the square of mass of the lepton.

Helicity suppression can be avoided by requiring that a photon is radiated in the final state. The relaxation in helicity suppression is in many cases comparable to the additional suppression due to the coupling to the electromagnetic interaction.

Phase space suppression

The branching fraction of a decay is proportional to the phase space of the final state. For a leptonic decay the phase space available to the lepton and neutrino is given by the factor $(1 - m_l^2/M_P^2)^2$. The phase space for the decay $D_s \to \tau\nu_\tau$ is very small compared to the other leptonic f_{D_s} decays.

Final state neutrinos

Final states which have a single neutrino have the potential to be experimentally very clean, as a distribution of the mass of the neutrino candidate recoiling against other particle candidates should be very close to zero, with a resolution close to that of the detector performance. Final states with two neutrinos will have a spectrum for the invariant mass of the two neutrinos, leading to a more complicated analysis with potentially larger backgrounds.

Table 3.2: Predictions for ratios of leptonic branching fractions of the D_s meson based solely on kinematic factors

Final state	$\tau^+\nu_\tau$		$\mu^+\nu_\mu$		$e^+\nu_e$
Relative ratio	1	:	0.1	:	2×10^{-6}

Choice of study

Given the kinematic factors the ratios of the expected branching fractions for the heavy flavour mesons can be predicted and are shown in table 3.2.

This analysis investigates all three leptonic decays of the D_s meson.

3.4.2 Choice of absolute branching fraction measurement

Some previous analyses have published the branching fractions $D_s \to \ell\nu_\ell$ relative to another branching fraction (usually $D_s \to \phi\pi$). This method is not ideal for two reasons:

- Any uncertainty on the branching fraction $D_s \to \phi\pi$ must be included in the final estimation of uncertainties. The uncertainty on $D_s \to \phi\pi$ is relatively large (7.8% relative uncertainty.)
- The final state of the $\phi\pi^+$ system is predominantly $K^+K^-\pi^+$. However, there are other intermediate states which can give the same final state. The contribution from $f_0(980)$ mesons is not negligible. Ordinarily one would not expect such effects to be important, but $f_0(980)$ mesons have a characteristic width of $(0.04-0.10)\,\mathrm{GeVc}^{-2}$. Predictions of the contributions of the decays $\phi \to K^+K^-$ and $f_0(980) \to K^+K^-$ would require a detailed Dalitz plot analysis.

Additionally, the Particle Data Group does not include measurements of relative branching fractions in their world averages for $D_s \to \ell\nu_\ell$.

These factors informed the choice to perform an absolute measurement of the branching fractions $\mathcal{B}(D_s \to \ell\nu_\ell)$.

3.4.3 Choice of experiment

The study of $\mathcal{B}(D_s \to \ell\nu_\ell)$ requires precise measurements of momenta and energy, as well as reliable identification of particles species. When reconstructing neutrinos it is also desirable to have knowledge of the centre of mass frame energy so that the mass

of the neutrino candidates can be inferred from the invisible four-momentum in the physics event. As outlined in subsequent chapters the BaBar experiment fulfills these requirements, making it an excellent choice for the branching fractions studied in this thesis.

3.5 Summary

Leptonic decays of mesons are expected to be experimentally clean probes of quantum chromodynamical processes that gives rise to the decay constants of mesons. In particular, the value of f_{D_s} is seen as a stringent test of current understanding of quantum chromodynamics. Recent experimental measurements and theoretical expectations have shown disagreement suggesting one of the following scenarios:

1. the experimental results are inaccurate
2. the expectations for the decay constants are inaccurate
3. there are processes beyond the Standard Model which contribute to the disagreement seen.

This analysis is being performed to provide additional constraints which will either bring the experimental world average closer to the theoretical expectation, or increase the tension between the two.

Chapter 4

The BaBar detector and the PEP-II collider

4.1 Overview

This chapter introduces the BaBar hardware, including the PEP-II accelerator and the data acquisition system. After a brief discussion of the concepts used in the detection of particles, the BaBar detector and PEP-II accelerator are both described and their goals outlined. Each of the subsystems in the detector is described in turn, with discussion of important technical details. The interactions of different particles with the detector, including background processes, are discussed, highlighting the most relevant aspects of the detector for each species of particle. The data acquisition system, including the triggering hardware and software, are described and the chapter concludes with a review of the data collected using the BaBar detector.

4.2 Interactions of in charged particles in media

Using simple and well understood physical processes it is possible to determine the species of a particle by observing how it interacts with the fields and material it encounters. The following physical processes aid particle species identification, and the BaBar detector was built with these concepts in mind.

4.2.1 Motion in a magnetic field

Moving charged particles in a magnetic field, $\vec{B}$, will be affected by the Lorentz force, $\vec{F}_L$

$$\vec{F}_L = \vec{v} \times \vec{B} \tag{4.1}$$

where $\vec{v}$ is the velocity of the charged particle. If the path of a charged particle in this field is known then its charge and momentum can be determined by measuring the curvature of the resulting helix, where the radius of curvature, ρ, is related to the particle's momentum which is transverse to the magnetic field, p_T, charge, q and the strength of the magnetic field, B, by

$$\rho = \frac{p_T}{qB} \tag{4.2}$$

4.2.2 Ionisation of media

As a charged particle passes through a medium it may ionise particles in that medium, or create electron-positron pairs. This can leave deposits of charge which may be trapped by the medium, or free charges which can propagate in local electric and magnetic fields.

4.2.3 Energy loss

As a charged particle passed through the detector it would lose energy due to interactions at a characteristic rate. The energy loss is dependent upon the momentum of the particle and is generally expressed as a function of distance traversed, $\frac{\mathrm{d}E}{\mathrm{d}x}$. Data recorded using the BaBar detector give the $\frac{\mathrm{d}E}{\mathrm{d}x}$ curves shown in figure 4.1.

Energy loss can be described by the Bethe formula (Bethe 1930):

$$\frac{\mathrm{d}E}{\mathrm{d}x} = -\frac{4\pi}{mc^2}\frac{Z}{A\beta^2}\left(\frac{q^2}{4\pi\varepsilon_0}\right)^2\left(\ln\left(\frac{2mc^2\beta^2\gamma^2}{I}\right) - \beta^2\right) \tag{4.3}$$

where the symbols for physical constants have their usual meanings, Z is the charge of the nuclei of the medium, q is the charge of the incident particle, and I is the mean excitation energy of the atoms in the medium.

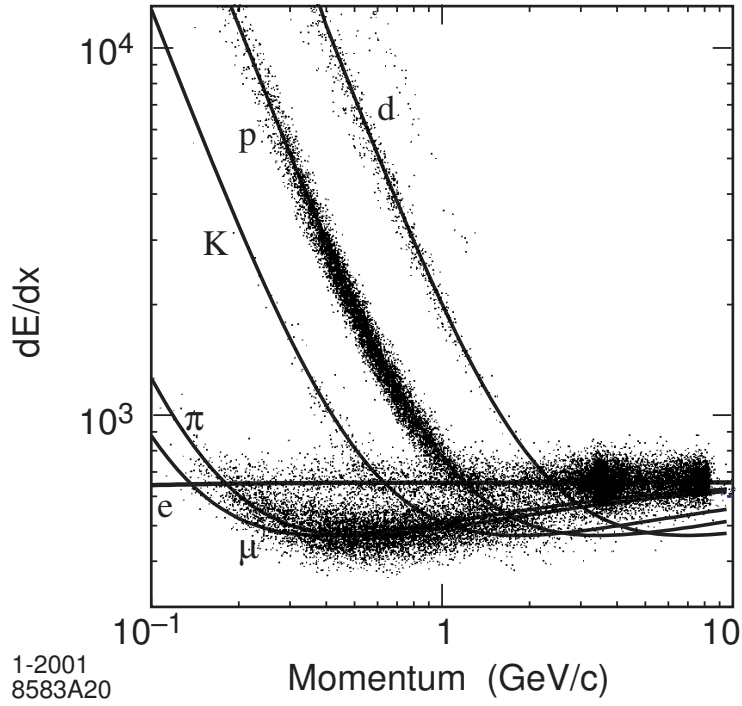

Figure 4.1: Energy loss as a function of momentum. (Aubert 2002)

4.2.4 Čerenkov radiation

As a charged particle passes through a medium it will generally interact with the medium and emit light. If the particle passes through the medium faster than the speed of light in that medium then a conical wavefront of light is emitted. The opening angle of this wavefront, θ, is related to the speed of the particle relative to the speed of light (in vacuo), β, by the relation

$$\cos\theta = \frac{1}{n\beta} \tag{4.4}$$

where n is the refractive index of the medium.

Combining the information about the particle's speed, β, and momentum, $p = \beta\gamma m$ it is possible to determine the particle's mass, m.

4.2.5 Radiation depth

As a photon passes through a medium it loses energy at a predictable rate. The rate of loss of energy is approximately exponential, and the radiation length describes the distance traversed as the photon loses half of its energy. By measuring the energy deposited in a given depth of medium it is possible to determine the energy of the

incident photon.

4.2.6 Conservation of four-momentum

As outlined in section 2.6.1 the energy and momentum of a closed system is conserved as a result of invariance under temporal and spatial translation. The conservation of four-momentum is useful with the BaBar experiment, where the invariant mass of the beams is a well known quantity.

4.3 The PEP-II collider

The BaBar experiment requires well known centre of mass frame energy in order to make precision measurements of Standard Model parameters. To obtain a precise centre of mass frame energy an electron-postitron collider is required. The PEP-II collider is an asymmetric electron-positron collider designed to operate at energies around the $\Upsilon(4S)$ resonance. The design luminosity is $L = 3\times10^{33}\,\mathrm{cm}^{-2}\mathrm{s}^{-1}$, although performance has exceeded this value on several occasions. The centre of mass frame energy can be varied and under normal operation the centre of mass energy has been set to the $\Upsilon(2/3/4S)$ resonances and 'OffPeak' ($\simeq 40\,\mathrm{MeV}$ below the $\Upsilon(4S)$ resonance). The electron beam had an energy of 9.0 GeV and the positron beam had an energy of 3.1 GeV, giving a Lorentz boost of $\beta\gamma = 0.56$. This boost makes the analyses of time dependent (and CP-violating) effects possible. It also necessitates the distinction between the forward and backward ends of the detector, placing constraints on the geometry of the design. Over the course of the experiment the PEP-II collider delivered $557\,\mathrm{fb}^{-1}$ of integrated luminosity (Seeman 2008).

4.4 The BaBar detector and its geometry

The BaBar experiment has many physics goals, including the study of $CP-$violating asymmetries in the neutral B system, precision measurements of many of the parameters of the Standard Model (including the Cabibbo-Kobayashi-Maskawa matrix elements) and decays of bottom and charm mesons and tau leptons. The BaBar detector has been designed to satisfy several stringent criteria required by these analyses, including:

- excellent reconstruction efficiency at low momentum
- fine momentum resolution
- excellent energy and angular resolution for neutral particles over a large energy range
- very good vertex resolution, both transverse and parallel to the beam direction
- excellent and unambiguous particle identification for electrons, muons, charged pions, charged kaons and protons over large ranges of momenta
- effective, selective and redundant triggers

- reliable, low noise electronics that can tolerate a high radiation environment for many years

The various parts of the detector fulfilled these requirements, providing information about the position and dynamics of various particles. The small region of space where the electron and positron beams met is called the interaction region. During its operation the detector components, listed in order of distance from the interaction region, were:

- Silicon vertex tracker
- Drift chamber
- Detector of internally reflected Čerenkov light (DIRC)
- Electromagnetic calorimeter
- Instrumented flux return

In addition to these components the detector relied on the following systems for its operation:

- Superconducting coil
- Level 1 hardware based trigger system
- Level 3 software based trigger system

The layout of the various components is shown in figures 4.2 and 4.3.

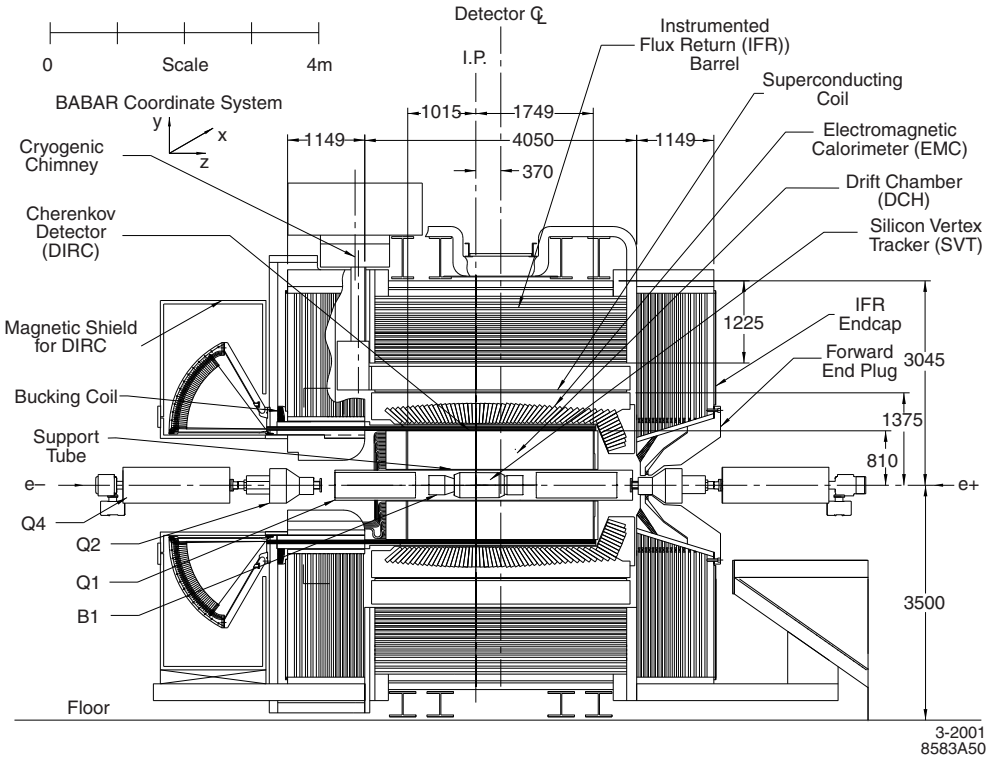

Figure 4.2: The longitudinal layout of the BaBar detector. (Aubert 2002)

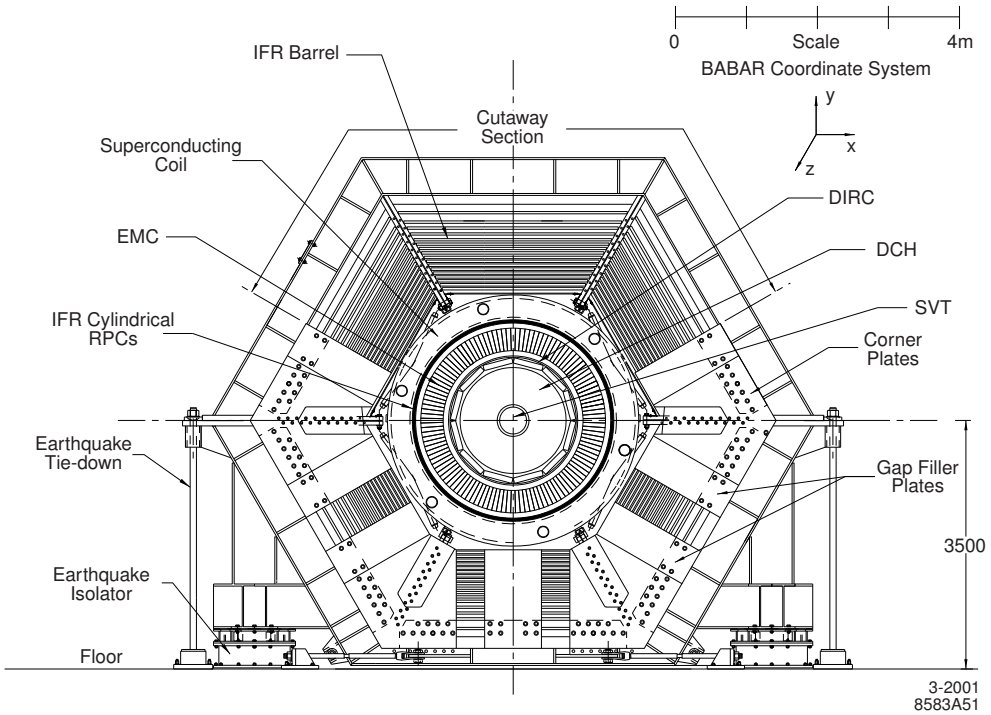

Figure 4.3: The axial layout of the BaBar detector. (Aubert 2002)

4.5 Silicon vertex tracker

The purpose of the silicon vertex tracker is to provide precise reconstruction of charged particles' trajectories and decay vertices close to the interaction point. The silicon vertex tracker is composed of 5 layers of silicon strips, each of which has two sets of sensors. The inner sides of the sensors give measurements of the z component of momenta and the outer sides of the sensors give measurements of the ϕ component of momenta.

4.5.1 Design and requirements

The silicon vertex tracker is vital for measurements of time dependent $CP-$asymmetry analyses, requiring a mean resolution of $80\,\mu$m in the z direction and a mean resolution of $\sim 100\,\mu$m in the transverse direction. Many of the decay products of heavy charm mesons have very low momentum, requiring excellent standalone tracking for particles with $p < 120\,\mathrm{MeVc}^{-1}$, the minimum momentum that can be measured reliably by the drift chamber. The silicon vertex tracker provides good measurement of tracks angles, which is required for the design resolution of DIRC.

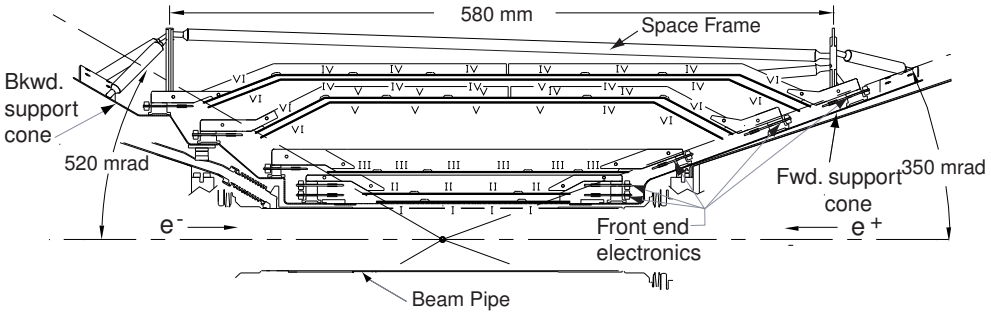

Figure 4.4: The layout of the silicon vertex tracker. (Aubert 2002)

The acceptance and angular coverage in the θ direction are limited by PEP-II instrumentation. The forward end of the silicon vertex tracker is in close proximity to a B1 permanent magnet and the coverage extends as far as $\theta = 20°$ in the forward direction. Due to the Lorentz boost of the CM frame the coverage in the backward direction extends as far as 150°, as shown in figure 4.4. To gain complete coverage in the ϕ direction the sensors of the three inner layers are angled by 5°, giving a small region of overlap. This also makes alignment easier. The sensors in outer two layers

are not angled, but are each split into two sub-layers of slightly different radii. This provides small regions of overlap and thus full angular coverage in the ϕ direction, as shown in figure 4.5.

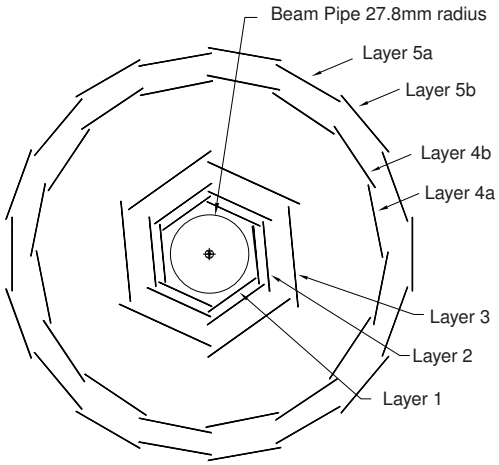

Figure 4.5: The cross-section of the silicon vertex tracker. (Aubert 2002)

4.5.2 Details of strip design

The silicon vertex tracker sensors are composed of asymmetric $p - n$ junction semiconductor detectors, giving fine granularity and hence excellent resolution. As an ionising particle passes through the junction it creates electron-hole pairs along its flight path. The number of electron-hole pairs created is proportional to the energy lost by the ionising particle. The potential difference across the detector causes the electrons to drift towards the anode and the holes to drift towards the cathode. The drifting electrons and holes are collected and the charge accumulated creates a current pulse on the electrode. The charge accumulated is proportional to the integral of the current pulse generated.

4.6 Drift chamber

The drift chamber allows the detection of charged particles, providing accurate information about the particles' trajectories and momenta with high precision. The drift chamber is cylindrical in shape, with an inner radius of 23.6 cm, an outer radius of 80.9 cm and a length of 276.4 cm. The layout is shown in figure 4.6. Particles traversing the drift chamber between 17.2° and 152.6° of the z axis will pass at least half of the layers of the drift chamber. These angles are indicated in figure 4.6

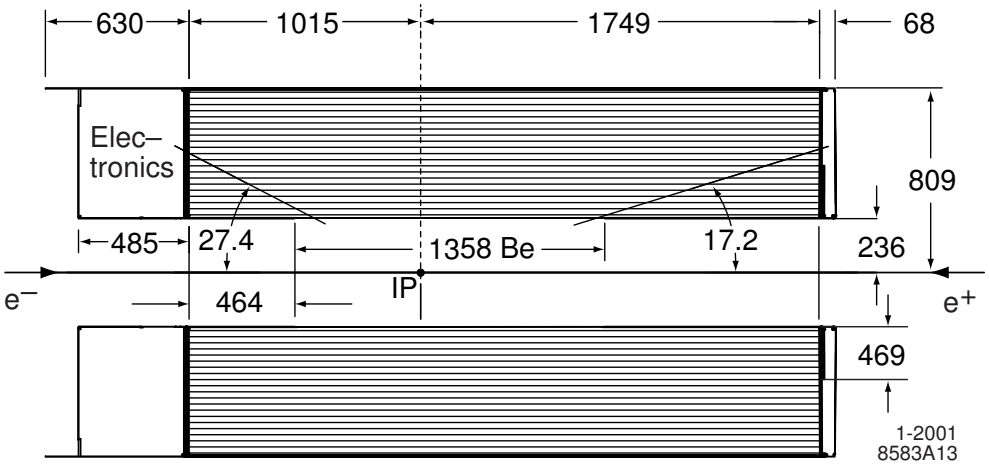

Figure 4.6: The layout of the drift chamber. (Aubert 2002)

The drift chamber contains 40 layers of small hexagonal cells, containing 28, 768 wires which respond to passing ionizing particles.

4.6.1 Design and requirements

The drift chamber provides useful information about charged particles that pass through the susbsystem over a large range of momenta. The drift chamber can use energy loss measurements to discriminate between charged pions and kaons. (A resolution of $\sim 7\%$ up to momenta of $700\,\mathrm{MeVc}^{-1}$ is sufficient.) The discrimination in the low momenta regime complements the discrimination in the high momenta regime in the DIRC.

Some neutral particles (such as the K_S^0) decay after passing through the silicon vertex tracker and the decay vertices of such particles must be determined solely from information provided by the drift chamber. Therefore the drift chamber is designed to provide logitudinal position of flight paths to a resolution of $\sim 1\,\mathrm{mm}$.

4.6.2 Details of cell design

There are 40 layers of hexagonal cells, of which 24 layers contain wires which are arranged at small angles to the $z-$axis (to provide information about the longitudinal position of particle trajectories). The wires are made of aluminium and held in a 80 : 20 mixture of helium : isobutane gas. This reduces multiple scattering inside the drift chamber, resulting in less than $0.2X_0$ of material, where X_0 is the radiation depth of the electromagnetic calorimeter.

There are 7104 drift cells in total. The layers of cells are arranged into 'superlayers', each consisting of four layers. The angles of the wires with the $z-$axis vary with the superlayers. The innermost superlayer has wires parallel to the $z-$axis. The wires in subsequent superlayers alternate between making positive, negative and zero angles with the $z-$axis in the range $45\,\text{mrad} - 76\,\text{mrad}$.

The cells are approximately hexagonal in shape with dimensions 11.9 mm in the radial direction and approximately 19.0 mm in the azimuthal direction. The hexagonal shape of the cells provides a good approximation to circular symmetry for a large portion of a cell. In each cell there is a sense wire at the centre and six field wires at the corners of the hexagonal profile. The field wires were grounded while the sense wires were held at a potential difference of 1960 V. The resulting drift time isochrones are approximately circular close to the sense wire, as shown in figure 4.7. The isochrones become progressively less circular the further they are from the sense wires.

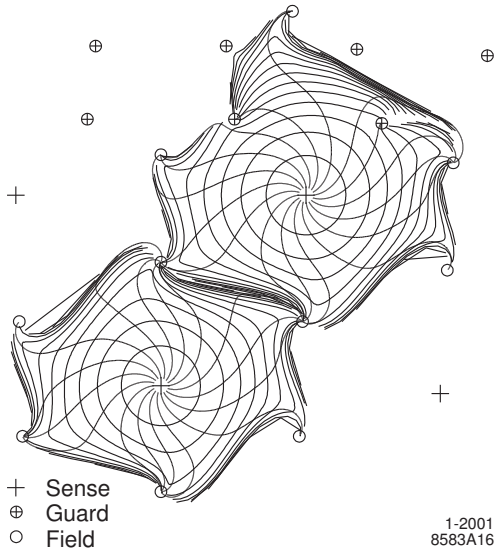

Figure 4.7: Drift time isochrones in two adjacent drift cells. The physical size of a cell depends upon the position within the detector. A typical size of cell is $19\,\text{mm} \times 11\,\text{mm}$. (Aubert 2002)

4.7 Detector of internally reflected Čerenkov light

The DIRC is a novel Čerenkovdetector developed for the BaBarexperiment. The DIRC occupies a thin radial region of space between the drift chamber and electromagnetic calorimeter while the bulk of the DIRC is located at the backward end of

the detector, to save space, as is evident in figure 4.8.

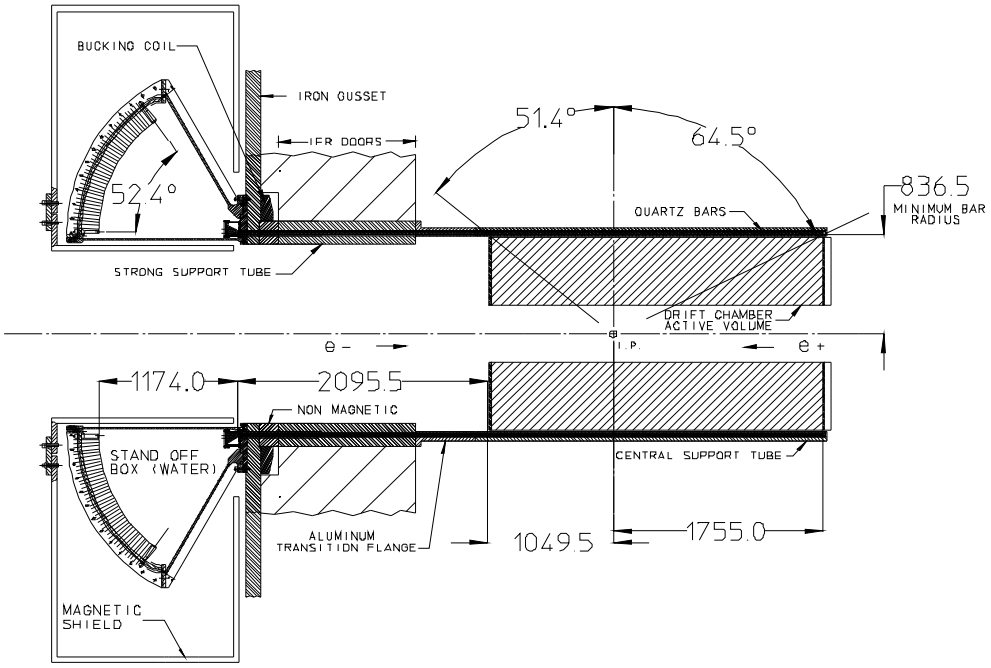

Figure 4.8: The layout of the DIRC. (Aubert 2002)

4.7.1 Design and requirements

The DIRC is designed to give excellent particle identification of charged particles while occupying as little volume as possible (hence reducing the cost of the calorimeter.) The DIRC needs to be able to discriminate charged kaons from other particles at momenta below 1 GeV. Studies show that charged pions and charged kaons can be separated using the DIRC with a separation significance of 4.2σ. At a mean charged kaon selection efficiency of $96.2 \pm 0.2\%$ the misidentification rate of charged pions is $2.1 \pm 0.1\%$ (Aubert 2002). The width of the DIRC must be small in order to reduce the energy lost before a particle traverses the electromagnetic calorimeter.

Charged particles pass through a thin twelve sided barrel composed of rows of twelve silica bars. Sufficiently fast particles will generate Čerenkov light with Čerenkov angle $\cos\theta_C = 1/n\beta$ where $\beta = v/c$ is the speed of the particle and c is the speed of light in vacuo. The silica has a relatively high refractive index ($n = 1.473$) so the threshold speed for generation of Čerenkov light is low. The Čerenkov light is then internally reflected at the surfaces of the silica bars and makes its way to the backward end of the detector where it meets the standoff box. There is a mirror at the forward end of the silica barrel so that all Čerenkov light will eventually reach

the backward end of the DIRC barrel.

The standoff box consists of a cone, a cylinder and 12 sectors of photo multiplier tubes. Each sector contains about 6,000 l of purified water, which is used as it is inexpensive and has a refractive index ($n \simeq 1.346$) close to that of fused silica, reducing the amount of light which is internally reflected at the silica-water boundary. The chromacity index of pure water is also close to that of fused silica, resulting in very low dispersion at the silica-water boundary.

The DIRC is sensitive to wavelengths of light as low as $\sim 300\,\text{nm}$. This limit comes from the epoxy used to glue the silica bars together. The silica bars internally reflect more than 0.9992 of the light with each reflection.

4.8 Electromagnetic calorimeter

The purpose of the electromagnetic calorimeter is to measure the energy of electromagnetic showers. The electromagnetic calorimeter is composed of two sections, the barrel and the endcap. The barrel is cylindrical and has polar coverage $26.8° < \theta < 141.8°$. The endcap is conical and has polar coverage $15.8° < \theta < 26.8°$. Both the barrel and endcap have full coverage in the azimuthal angle. The layout of the electromagnetic calorimeter is shown in figure 4.9.

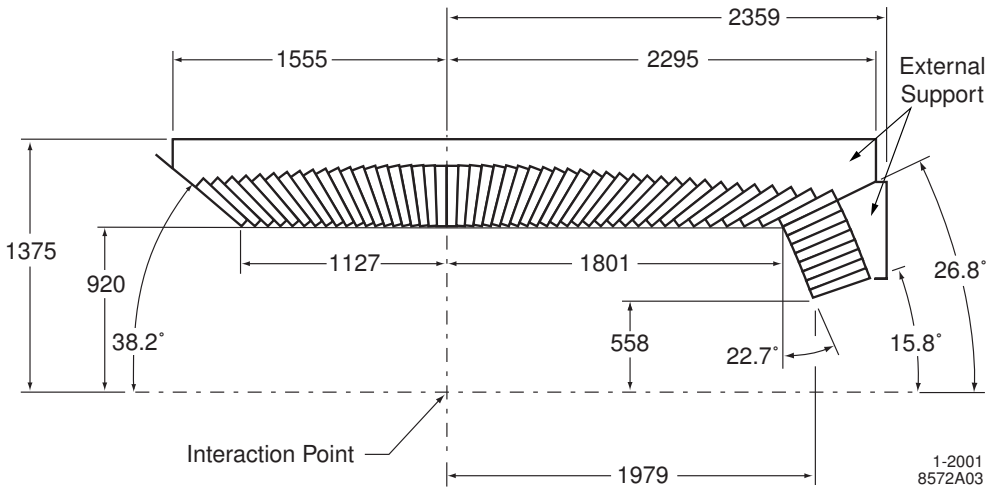

Figure 4.9: The layout of the electromagnetic calorimeter. (Aubert 2002)

The electromagnetic calorimeter contains an array of 6580 Thallium doped CsI crystals which scintillate as particles pass through. The resulting showers are detected by two silicon PIN photodiodes at the end of each crystal.

4.8.1 Design and requirements

The physics analyses that use the BaBar detector require excellent efficiency, accuracy and resolution for the energy and the angular position of electromagnetic showers. The energy range for the showers is $20\,\mathrm{MeV} < E_{shower} < 9\,\mathrm{GeV}$. The energy resolution of the calorimeter is given by two terms added in quadrature:

$$\frac{\sigma_E}{E} = \frac{a}{\sqrt[4]{E}} \oplus b \tag{4.5}$$

where E and σ_E are the energy and root mean square uncertainty of the energy of an incident photon. The energy dependent term results from photon statistics as well as electronic noise in the detector. The constant term is a result of non-uniformity in the collection of light and is influenced by leakage and the absorption properties of the crystals. Both a and b are of the order $\sim 1\%$. Studies show the values of a and b fitted over a large energy range to be:

$$\frac{\sigma_E}{E} = \frac{(2.32 \pm 0.30)\%}{\sqrt[4]{E(\mathrm{GeV})}} \oplus (1.85 \pm 0.12)\% \tag{4.6}$$

The angular resolution is characterised as:

$$\sigma_\theta = \sigma_\phi = \frac{c}{\sqrt{E}} + d \tag{4.7}$$

where the angular resolution is dependent on the transverse crystal size, distance from the interaction point and incident energy. The angular resolution can be related to the resolution of the position, with a resolution of $\sim 1\,\mathrm{mm}$ corresponding to $\sim 1\,\mathrm{mrad}$. Studies of π^0 and η decay show the angular resolution to be:

$$\sigma_\theta = \sigma_\phi = \left(\frac{(3.87 \pm 0.07)}{\sqrt{E(\,\mathrm{GeV})}} + 0.00 \pm 0.04 \right) \mathrm{mrad} \tag{4.8}$$

4.8.2 Details of crystal design

The electromagnetic calorimeter crystals are trapezoidal in shape with lengths varying from 29.6 cm in the backward direction and 32.4 cm in the forward direction. A typical crystal is shown in figure 4.10. The length varies in order to reduce leakage from higher energy particles. A typical area for the front face of a crystal is $4.7 \times 4.7\,\mathrm{cm}^2$ while the back area is typically $6.1 \times 6.0\,\mathrm{cm}^2$. The transverse size and number of crystals is chosen such that the transverse size is comparable to the Molière radius, giving

excellent angular resolution, while at the same time limiting the number of crystals and readout channels needed.

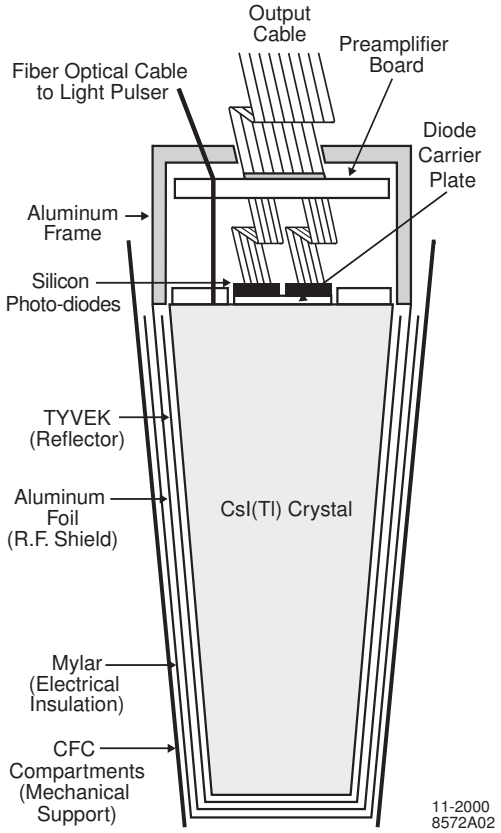

Figure 4.10: The design of a typical electromagnetic calorimeter crystal assembly. (Aubert 2002)

Minimising the probability of pre-showering is an important factor in the detector design. The barrel and outer five rings of the endcap are shadowed by less than $0.3 - 0.6X_0$ of material before the front faces of the crystal. The support structure for the crystals is located behind the rear faces of the crystals whereas the front faces of the crystals have a thin gas seal. The faces of the crystals are polished so that most light incident on the inner surfaces is internally reflected. Transmitted light is partly recovered by surrounding the crystals in two layers of diffuse white reflector. The physical properties of the crystals are shown in table 4.1.

The crystals act as a light guide to collect the light at the photodiodes which are mounted at the rear surface. Two photodiodes are attached to the rear face of each crystal. The photodiodes measure $2 \times 1\,\mathrm{cm}^2$. The photodiodes are not attached to the crystals directly, but are glued to a transparent polystyrene substrate.

Table 4.1: Properties of the CsI(Tl) crystals in the electromagnetic calorimeter. [Properties of the CsI(Tl) crystals in the electromagnetic calorimeter. (Aubert 2002)]

Parameter	Value
Radiation length (X_0)	1.85 cm
Molière radius	3.8 cm
Density	$4.5\,\mathrm{g\,cm^{-3}}$
Light yield	$50,000\,\gamma\,\mathrm{MeV^{-1}}$
Light yield temperature coefficient	$0.28\,\%\,^{\circ}\mathrm{C^{-1}}$
Peak emission λ_{max}	565 nm
Refractive index (λ_{max})	1.8

4.9 Instrumented flux return

The purpose of the instrumented flux return is to identify muons and neutral hadrons with high efficiency (where charged hadrons are efficienctly and reliably identified using the silicon vertex tracker, drift chamber, and DIRC). The instrumented flux return consists of a series of resistive plate chambers which are sandwiched between plates of steel. The instrumented flux return is designed to give a large solid angle coverage as well as providing a high muon background rejection over a large range of momenta ($p > 1\,\mathrm{GeVc^{-1}}$).

4.9.1 Design and requirements

The instrumented flux return is split into three main regions: the barrel, the forward doors and backward doors. The instrumented flux return has hexagonal symmetry about the $z-$axis. In addition to these regions, there is a cylindrical region just outside the electromagnetic calorimeter. The instrumented flux return contained 19 resistive plate chamber layers in the barrel and 18 resistive plate chamber layers in the doors. The six barrel regions each contained 57 resistive plate chamber modules, and each pair of doors contained 216 resistive plate chamber modules. There were 32 resistive plate chamber modules in the cylindrical region, giving a total of 806 resistive plate chamber modules. The purpose of the cylindrical region was to detect particles exiting the electromagnetic calorimeter. The layout of the instrumented flux return is shown in figure 4.11 and in table 4.2.

The resistive plate chambers were located in gaps between plates of steel, whose

widths varied in thickness (2 cm thick for the innermost plates, 10 cm thick for the outermost plates). The spacing between the plates varies from 3.5 cm in the inner layers of the barrel to 3.2 cm in other regions.

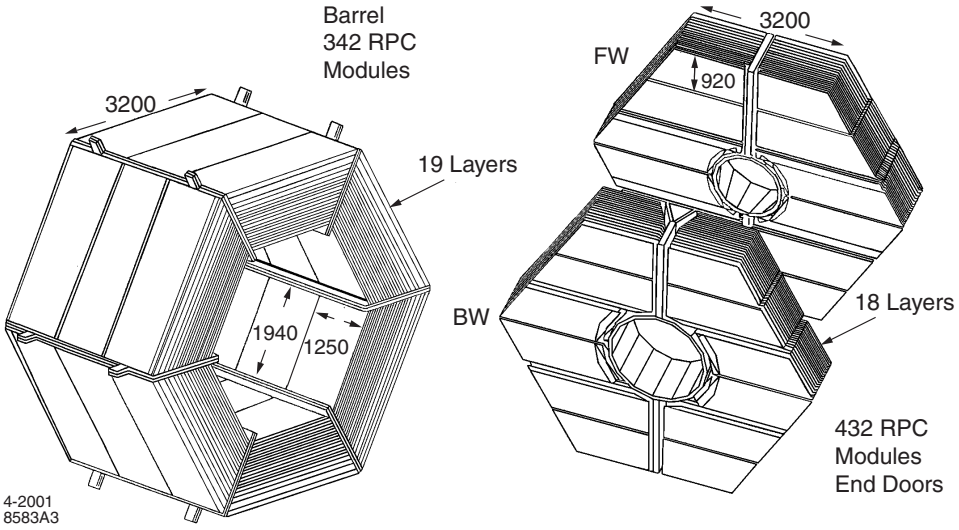

Figure 4.11: The layout of the instrumented flux return. (Aubert 2002)

4.9.2 Details of resistive plate chambers design

The resistive plate chambers were designed to create as little dead space in the angular coverage as possible. As a result there were 25 different shapes and sizes of resistive plate chamber in the instrumented flux return. The size of a resistive plate chamber is limited by the maximum size of the materials available ($320 \times 130\,\mathrm{cm}^2$). Given these constraints it was necessary to join two or three resistive plate chambers to cover the full extent of the gaps between the steel plates.

In the barrel region there were three resistive plate chamber modules in each gap, with 32 strips running perpendicular to the $z-$axis (to measure the z coordinate of a particle flight path) and 96 strips in the orthongal direction (to measure the ϕ coordinate of a particle flight path). In the doors, each half-door was divided into three sections. Each section was covered by two resistive plate chambers with strips running in the vertical and horizontal directions. In the cylindrical region the layers were split into four sections in the ϕ coordinate and each section had four sets of two single gap resistive plate chambers. The inner layer had helical strips that run parallel to the diagonals of the module. The outer layer had strips parallel to the z and ϕ directions.

Table 4.2: Arrangement of the resistive plate chambers in the instrumented flux return.

Arrangement of the resistive plate chambers in the instrumented flux return. (Aubert 2002)

Region	Number of sectors	Coordinate	Number of layers	Number of strips	Strip length (mm)	Strip width (mm)
Barrel	6	ϕ	19	96	3500	$19.7 - 32.8$
		z	19	96	$1900 - 3180$	38.5
Doors	4	y	18	6×32	$1240 - 2620$	28.3
		x	18	3×64	$100 - 1800$	38.0
Cylinder	4	ϕ	1	128	3700	16.0
	4	z	1	128	2110	29.0
	4	u	1	128	$100 - 4220$	29.0
	4	v	1	128	$100 - 4230$	29.0

4.9.3 Upgrade

After the first years of running the resistive plate chambers degraded, leading to poor performance. The resistive plate chambers were replaced with a series of limited streamer tubes in largely the same configuration. Six layers of brass were added to improve pion and muon separation without significant change to the magnetic properties of the instrumented flux return.

4.10 Passage of particles through the detector

It is informative to explore how different particles pass through the BaBar detector and interact with the various components. These interactions can be used to reconstruct a candidate trajectory, allowing one to form hypotheses about the presence of particles in the event. Particles are generally not at rest in the laboratory frame and the term "in flight" refers to the period of time between a particle's creation and decay.

Although the muon and charged pion (and to a lesser extend the charged kaon) are not stable, their flight lengths are typically longer than the dimensions of the tracking systems of the detector.

4.10.1 Passage of heavy mesons

Heavy mesons decay via the weak interaction, with lifetimes of the order 10^{-12} s. When the accelerator delivers beams at energies greater than the $b\bar{b}$ production threshold, pairs of B mesons from the decay $\Upsilon(4S) \to B\bar{B}$ have a Lorentz boost of $0.49 < \beta\gamma < 0.63$ in the laboratory frame. A typical length of flight for a B meson is $0.23 < d < 0.30$ mm in this frame. Charm mesons that arise from decay of these B mesons have a Lorentz boost of $\beta\gamma < 2.47$. Similarly, charm mesons produced via the interaction $e^+e^- \to c\bar{c} \to DX$ have a Lorentz boost of $\beta\gamma < 2.64$. As a result, heavy mesons do not interact directly with the detector and their presence must be inferred from the daughter particles' interactions.

4.10.2 Passage of stable, charged particles

Stable, charged particles (electrons, muons, charged pions, charged kaons and protons) will interact with the tracking subsystems (the silicon vertex tracker and drift chamber) as they pass through the detector. If the location and time of the various interactions are known a candidate trajectory can be reconstructed. These trajectories are helical in shape, due to the presence of the magnet. The direction of the curvature of the helix is used to identify the charge of the particle candidate.

A physics event is defined as an interaction of the e^+e^- particles from the beams which results in either the generation of other particles, or in the scattering of the e^+e^- pair. Figure 4.12 shows a typical event display for a physics event with charged particles.

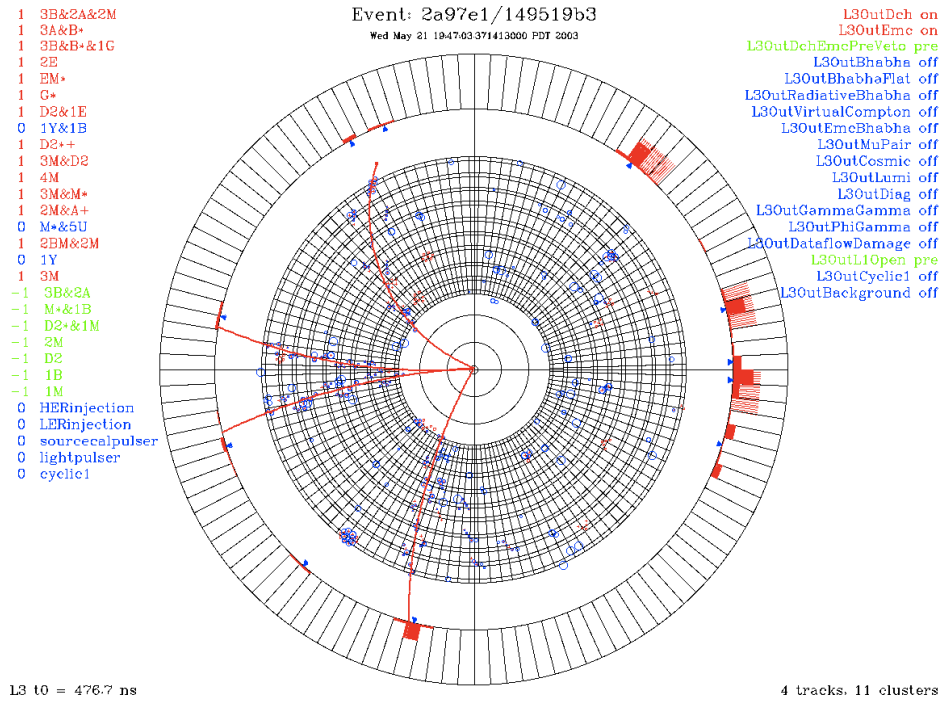

Figure 4.12: A typical event in the BaBar detector. The event display shows a cross section of the BaBar detector, including the drift chamber and electromagnetic calorimeter. Blue circles indicate hits in the drift chamber. Red rectangles indicate energy deposition in the electromagnetic calorimeter, with the height of the rectangle indicating the size of the energy deposition, where the full height of a crystal corresponds to 2 GeV. (*The BaBar Collaboration* 2010)

4.10.3 Passage of leptons

Neutrinos interact with matter in the detector very rarely and this rate of interaction can be neglected for all BaBar analyses.

The tau lepton typically does not remain in flight long enough to be observed directly in the detector. Therefore the discussion of the passage of leptons through the detector will be limited to electrons and muons. Leptons can originate from direct production ($e^+e^- \to \ell^+\ell^-$) or from weak decays of heavier particles (usually $A \to B\ell\nu_\ell$, where A and B are any systems of particles allowed by conservation laws).

Electrons

Electrons which pass through the silicon vertex tracker and drift chamber will leave information which can be used to reconstruct a candidate trajectory consistent with an electron mass hypothesis. In addition to the tracking information, electrons can be identified by the interactions with the electromagnetic calorimeter. Electrons deposit nearly all of their energy (via Bremsstrahlung radiation) as they pass through the

crystals. Combining information about the energy deposition from the electromagnetic calorimeter with information about the candidate momentum from the tracking system allows good discrimination between electrons and other charged particles. The lateral moments of the energy deposition in the electromagnetic calorimeter can be used to improve discrimination. Electron showers tend to have a smaller angular spread than hadronic showers. Electrons rarely reach the instrumented flux return.

Muons

Like electrons, muons will interact with the tracking systems, allowing the reconstruction of a candidate trajectory consistent with a muon mass hypothesis. Muons will also deposit energy in the electromagnetic calorimeter but will deposit a smaller fraction when compared to the electron (due to the mass dependence in the Bethe-Bloch equation describing energy loss due to Bremsstrahlung radiation). Most muons will reach the instrumented flux return with many reaching every layer of the instrumented flux return. Combining information from the tracking systems, the $\frac{\mathrm{d}E}{\mathrm{d}x}$ information from the electromagnetic calorimeter and the information from the instrumented flux return is usually sufficient to identify a high momentum muon. Lower momentum muons tend to reach the instrumented flux return but do not penetrate to the final layers. Information about energy loss in the instrumented flux return combined with information from the tracking systems and electromagnetic calorimeter is usually enough to identify a muon.

4.10.4 Passage of charged hadrons

Charged pions

The origin of charged pions in the detector is not always close to the interaction point, as K^0_S mesons may decay after flying for several centimetres. As a result a charged pion candidate trajectory need not extend as far as the silicon vertex tracker in all cases. Information from the drift chamber (and silicon vertex tracker if present) can be combined with information from the DIRC and instrumented flux return. A charged pion will typically not traverse the full depth of the instrumented flux return and the measured energy loss, $\frac{\mathrm{d}E}{\mathrm{d}x}$ can be used to discriminate against a muon hypothesis.

Charged kaons

Charged kaons act in a similar manner to charged pions. They will interact with the tracking subsystems and DIRC. Information from the drift chamber and DIRC provides good discrimination between charged kaon candidates and charged pion candidates. The DIRC provides excellent discrimination for high momentum candidate trajectories whereas the drift chamber provides excellent discrimination for lower momentum candidate trajectories. The time of flight for a charged kaon is 1.234×10^{-8} s ($= 3.71\,\mathrm{m}/c$ where c is the speed of light in vacuo) which is of the order of the width of the detector, so many charged kaons will not reach the instrumented flux return before decaying.

Protons

Protons passing through the drift chamber have a significantly large rate of energy loss compared to other particles at momenta below 1 GeV, allowing excellent discrimination between proton candidates and other particle candidates. At higher momenta the interactions with the DIRC combined with information from the drift chamber is usually enough to allow excellent discrimination between proton candidates and other particle candidates.

4.10.5 Passage of neutral hadrons

Neutral pions

The lifetime of the neutral pion is very short (8.4×10^{-17} s) so direct observation of the interactions of the neutral pion is not possible. The neutral pion decays almost exclusively to two photons, which are detected in the electromagnetic calorimeter and required to have an invariant mass consistent with that of a neutral pion.

K_S^0 mesons

The time of flight of a K_S^0 meson is 8.953×10^{-11} s. As a result K_S^0 mesons will tend to decay before interacting with the detector. As K_S^0 mesons are not charged they will not leave a candidate trajectory in the drift chamber. K_S^0 mesons are identified by their daughter particles, and are usually reconstructed from a pair of $\pi^+\pi^-$ mesons.

K_L^0 mesons

K_L^0 mesons have a much longer time of flight than the K_S^0 mesons and therefore they can interact with more than one subsystem. In particular a K_L^0 can interact with the electromagnetic calorimeter depositing energy, before interacting with the instrumented flux return losing more energy in the process.

Neutrons

The detection of neutrons has not motivated much activity over the course of the experiment. As a result, there is no algorithm for detection of neutrons and their detection plays no role in the majority of BaBar analyses.

4.10.6 Passage of photons

Photons interact almost exclusively with the electromagnetic calorimeter. Photons with low energies will deposit nearly all their energy in the electromagnetic calorimeter whereas photons with energies greater than $\sim 1\,\text{GeV}$ tend to deposit energy elsewhere, through leakage or interactions with detector matter. Given the lack of tracking information for photons, the electromagnetic calorimeter provides the only information about the direction of a photon candidate. Photon candidates can be seen on the right hand side of figure 4.12.

4.11 Other interactions

In addition to interactions from particles arising from e^+e^- collisions there are several other processes which can lead to interactions with the detector:

- interactions between particles in the beams and residual gas in the vacuum pipe
- interactions between photons and the detector material (pair production)
- Bhabha scattering of electrons and positrons in the beams
- passage of particles which ionise the electrons and protons in the detector material
- generation of hadronic matter as ionising particles interact with the detector material
- passage of cosmic rays through the detector

4.11.1 Beam-gas interactions

Interactions between the electron and positron beams and any residual gas in the vacuum tube were not uncommon during periods of running. Such interactions can lead to a large number of high momentum particles being created. Under such conditions data acquisition was temporarily halted and steps taken to eliminate such interactions (for example, tuning beam parameters). These interactions can lead to large amounts of damaging ionising radiation which can degrade crystals in the electromagnetic calorimeter. During running with a single beam the detector remained active to allow the study of these interactions and how they could affect data acquisition during normal running.

4.11.2 Pair production

Photons incident on the detector material can form pairs of fermions. Typically an electron-positron is produced, although high energy photons can also produce pairs of muons. Pair production can lead to the detection of candidate trajectories that do not originate from a primary or secondary vertex.

4.11.3 Bhabha scattering

Bhabha scattering occurs when electrons and positrons scatter at shallow angles. These interactions can be used to calibrate various detector subsystems in the high momenta regime. Figure 4.13 shows the BaBar event display for a two prong interaction, which is typical for a process such as $e^+e^- \to e^+e^-$.

4.11.4 Passage of ionising particles and generation of hadronic matter

As particles pass through the detector material they can ionise particles in the material of the detector, leading to the emission (and possible detection) of real protons and electrons. Very high energy particles can sometimes interact with the detector material to produce hadronic particles. Both processes can dramatically affect the flight path of the incident particle.

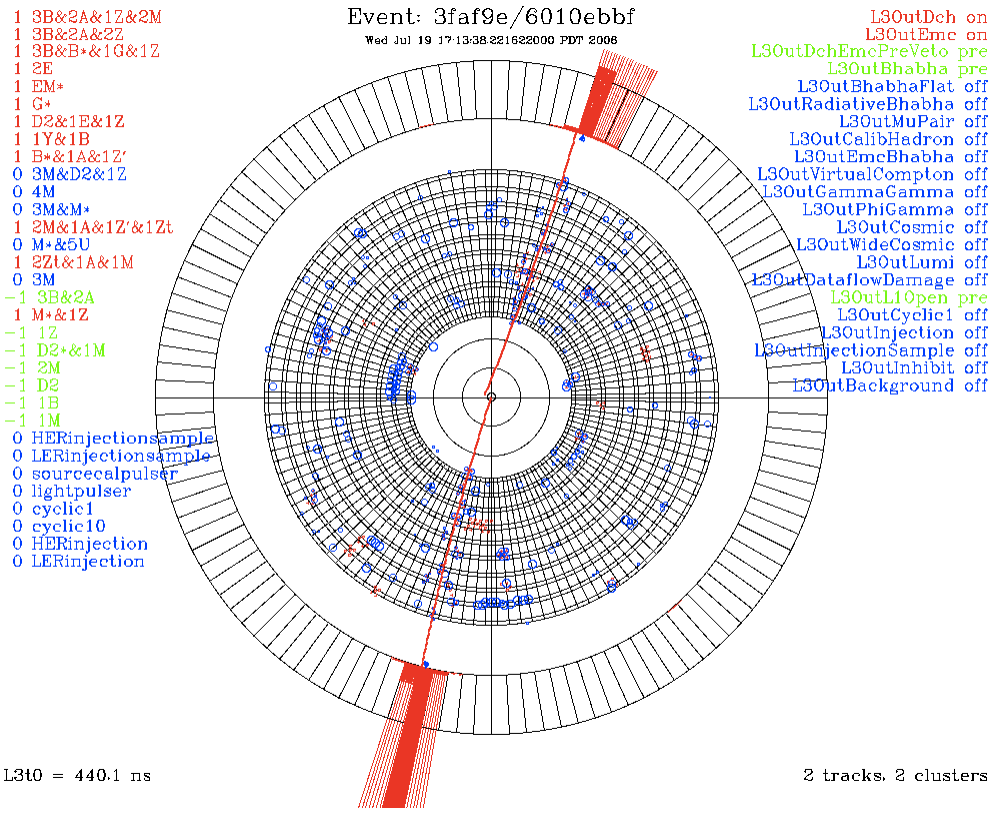

Figure 4.13: A typical two-prong event in the BaBar detector. The event display shows a cross section of the BaBar detector, including the drift chamber and electromagnetic calorimeter. Blue circles indicate hits in the drift chamber. Red rectangles indicate energy deposition in the electromagnetic calorimeter, with the height of the rectangle indicating the size of the energy deposition, where the full height of a crystal corresponds to 2 GeV. (*The BaBar Collaboration* 2010)

4.11.5 Cosmic rays

High energy particles from the upper atmosphere can interact with the detector. These interactions are easy to identify due to the direction of the incoming particle as well as the charge inbalance. During running with no beams the detector remained active to allow the study of cosmic rays. Cosmic rays can be used to calibrate various subsystems (for example, muon detection efficiencies).

4.12 Triggers

The rate of collisions at the PEP-II collider was so high that it was impractical to store information about every physics event candidate. This large rate of event candidates was anticipated in the design of the BaBar detector and to maintain a high efficiency of data acquisition with manageable rates of information processing a two level trigger

was used to reject uninteresting event candidates.

4.12.1 Level 1 trigger

The Level 1 (hardware) trigger is a hardware based trigger intended to identify potentially interesting event candidates. The hardware trigger would take information from the drift chamber, electromagnetic calorimeter, and instrumented flux return. The drift chamber and electromagnetic calorimeter triggers were independent, which allowed excellent efficiency and makes studies of trigger efficiency possible. The instrumented flux return trigger can be used to trigger $\mu\mu$ event candidates and cosmic ray candidates. Every 134 ns the drift chamber electromagnetic calorimeter and instrumented flux return local triggers would send raw data (primitives) to the global trigger. If any valid primitives reached the global trigger, a hardware `accept` command would be issued and event readout would proceed.

Drift chamber trigger

Information from the drift chamber would be processed in two stages. In the first stage a series of track segment finder modules would be used to identify signals in neighbouring cells of the drift chamber. In each superlayer the third layer would be designated as a pivot layer. The track segment finder would compare different nearby cells and return a two bit number indicating whether that particular pivot cell had been used to identify: no acceptable track segment, a poor track segment, a track segment in three layers or a track segment in four layers. These two bit numbers would be passed to the binary link tracker, which would join the segments to form track candidates. The arrangements of cells around a pivot cell is shown in figure 4.14.

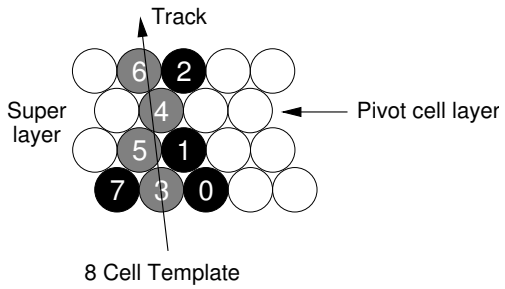

Figure 4.14: Outline of the track segment finder module. (Aubert 2002)

The binary link tracker would receive 320 bits every 134 ns corresponding to 320

Table 4.3: The different primitives returned by the drift chamber trigger. The values given for the threshold momenta show typical (adjustable) values. (Aubert 2002)

Primitive label	Description	Number of bits	Momentum threshold (MeVc^{-1})
B	Short track reaching fifth superlayer	16	120
A	Long track reaching tenth superlayer	16	180
A'	High transverse momentum track	16	800

supercells with 32 sectors in the ϕ direction and 10 sectors (corresponding to each superlayer) in the radial direction. Track candidates would be assessed from the innermost superlayer. A candidate that has signal in from the innermost superlayer to outermost superlayers would be classified as type A. In order to be classified as type A a track candidate must have signal in at least eight of the ten superlayers, and there must be no more than five supercells in the azimuthal direction between signals in adjacent superlayers. A candidate that has signal from the innermost superlayer to the fifth superlayer would be classified as type B.

The data would be summarised in two 16 bit ϕ maps (one for type A candidates and one for type B candidates) and sent to the global trigger. The transverse momentum discriminator would take information from high quality track segments and identify candidates with high transverse momentum. These would be classified type A'. The drift chamber primitives are summarised in table 4.3.

Electromagnetic calorimeter trigger

The crystals of the electromagnetic calorimeter would be divided into 280 towers, which correspond to 7 sectors in the θ direction and 40 sectors in the ϕ direction, with 240 towers in the barrel and 40 towers in the endcap. The towers in the barrel contain 24 crystals with 8 in the θ direction and 3 in the ϕ direction. The towers in the endcap contain $19 - 22$ crystals and form wedges in the ϕ direction.

The energies of all the crystals in each tower would be summed. To reduce backgrounds from electronic noise, each crystal would be required to show at least 20 MeV of energy in order to be included in the sum. Ten trigger processor boards would be used to combine these summed energies to determine the electromagnetic calorimeter trigger response. The energies of the towers in the ϕ sectors would be summed and

Table 4.4: The different primitives returned by the electromagnetic calorimeter trigger. The threshold energies show typical (adjustable) values. (Aubert 2002)

Primitive label	Description	Number of bits	Energy threshold (MeV)
M	Low energy	20	100
G	Intermediate energy	20	250
E	High energy	20	700
X	Endcap	20	100
Y	Backward barrel	10	1000

the tower would show signal if the energy exceeded a threshold. The energies of pairs of adjacent sectors in ϕ would be summed in the same way. Primitives for the barrel would be expressed in a 20 bit number, where each bit would correspond to a pair of ϕ sectors and the bit would be set to 1 if either sector showed signal. Primitives for the endcap would be expressed in the same manner, except that each bit would correspond to 4 ϕ sectors. A separate 10 bit number would be used for the backward end of the barrel. The electromagnetic calorimeter trigger would then return five primitives, which are outlined in table 4.4.

Instrumented flux return trigger

The instrumented flux return trigger was designed to identify events of the type $e^+e^- \rightarrow \mu^+\mu^-(\gamma)$ and cosmic rays. The instrumented flux return would be divided into ten sectors, with one sector for each of the barrel sextants, and one sector for each of the half doors. A muon candidate would be identified if four of eight layers in a given sector saw signal. The different possible topologies of interest for the instrumented flux return trigger are shown in table 4.5 and are passed to the global trigger as a 3 bit number.

Table 4.5: The different topologies of interest for the instrumented flux return trigger. (Aubert 2002)

Label	Description
$U = 1$	At least two muon candidates (Excluding $U = 5, 6, 7$)
$U = 2$	One muon candidate in the backward doors
$U = 3$	One muon candidate in the forward doors
$U = 4$	One muon candidate in the barrel
$U = 5$	Two back to back muon candidates in the barrel and one muon candidate in the forward doors
$U = 6$	One muon candidate in the barrel and one muon candidate in the forward doors
$U = 7$	Two back to back muon candidates in the barrel

Global hardware trigger

The global hardware trigger would take the primitives provided by the drift chamber, electromagnetic calorimeter, and instrumented flux return triggers. The hardware trigger would take this information and use a lookup table to determine whether to issue an `accept` command.

4.13 Level 3 trigger

The global Level 3 (software) trigger would take information from the detector for events which passed the hardware trigger selection criteria. The software for the software trigger would be run on an online computing farm. The hardware trigger would pass a 32 bit number in the form of a series input lines to the software trigger. If a given bit was set to 1 the software trigger would perform a given algorithm which would return a flag, indicating a pass or fail. Some flags would provide the software trigger with a veto.

One of the main roles of the software trigger is to remove Bhabha events, which are events of the type $e^+e^- \rightarrow e^+e^-(\gamma)$, where the electron and positron scatter, typically at low angles. Bhabha events would typically be identified as an event with a single track in the backward part of the barrel (the scattered positron) or from two track events where the tracks are back to back in the centre of mass frame. Events of the type $e^+e^- \rightarrow \gamma\gamma$ would be identified by two high energy clusters in the electromagnetic calorimeter which are back to back in the centre of mass frame frame.

Certain algorithms in the software trigger would use data exclusively taken from the drift chamber or electromagnetic calorimeter, which allows studies of the efficiencies of each subsystem. The software trigger would veto certain crystal measurements from the electromagnetic calorimeter by requiring a minimum energy of 20 MeV and requiring that measurements take place within 1.3μs of the electron-positron collision.

4.14 Data acquisition system

During normal running of the BaBar experiment the conditions of the BaBar detector and PEP-II accelerator would be monitored and recorded. Access to this information would allow experts perform maintenance of the various subsystems and resolve any

issues concerning data acquisition. The raw data were processed onsite at SLAC National Accelerator Laboratory and event reconstructions of the data were processed at a Tier A computing center at the University of Padova, Italy.

4.14.1 Online dataflow

The online dataflow system would be responsible for communicating with and controlling the front end electronics for the various subsystems. In addition, the online dataflow system would acquire the event data. This system would take the information from the hardware trigger and upon receiving an `accept` command, it would communicate with the subsystems' front end electronics to acquire the event data.

4.14.2 Online event processing

The online event processing system would be responsible for the processing of complete events, including the software required to operate the software trigger. This system would also provide information for data quality monitoring and online calibrations. The system was arranged into many software modules which would perform different tasks. This allowed one to write software and data monitoring offline, and investigate issues with the software offline. Additional data from the software trigger would be stored, allowing future reprocessing of data, if necessary.

4.14.3 Run control

During periods of data taking the BaBar detector was monitored at all times in shifts by at least two members of the BaBar Collaboration. The user interface provided access to a wide range of data concerning the state of the detector and of data quality. Much of the data were recorded automatically, while the physicists on shift provided on-site support in the event of data taking issues.

4.15 Running periods

Data were collected in running periods at the BaBar detector. A running period is a long stretch of time (typically months) with little or no interruption in data taking. For the purposes of this thesis the following running periods are defined in table 4.6. The integrated luminosity as a function of time is shown in figure 4.15. Several techniques are used to estimate the integrated luminosities of the various running

periods, each with their own uncertainties. This analysis does not require a precise knowledge of the luminosity, so these uncertainties are omitted in the determination of systematic uncertainties.

Table 4.6: Summary of the BaBar running periods. (*The BaBar Collaboration* 2010)

	Name	Energy (GeV)	Date	Integrated luminosity (fb^{-1})
Run 1	OnPeak	10.58	1999/10/20 to	22.4 ± 0.16
	OffPeak	10.54	2000/10/29	2.9 ± 0.02
Run 2	OnPeak	10.58	2001/02/06 to	66.7 ± 0.48
	OffPeak	10.54	2002/06/30	8.1 ± 0.06
Run 3	OnPeak	10.58	2002/11/17 to	35.1 ± 0.25
	OffPeak	10.54	2003/06/29	2.8 ± 0.02
Run 4	OnPeak	10.58	2003/09/09 to	107.2 ± 0.70
	OffPeak	10.54	2004/07/31	11.7 ± 0.07
Run 5	OnPeak	10.58	2005/04/16 to	141.0 ± 0.93
	OffPeak	10.54	2006/08/17	16.4 ± 0.10
Run 6	OnPeak	10.58	2007/01/18 to	82.9 ± 0.50
	OffPeak	10.54	2007/09/04	8.8 ± 0.06
Run 7	$\Upsilon(3S)$ OnPeak	10.36	2007/12/03 to	28.0 ± 0.20
	$\Upsilon(2S)$ OnPeak	10.02	2008/04/07	13.6 ± 0.10
			Total OnPeak	432.9
			Total OffPeak	47.8
			Total $\Upsilon(3S)/\Upsilon(2S)$	41.6
			All runs	522.3

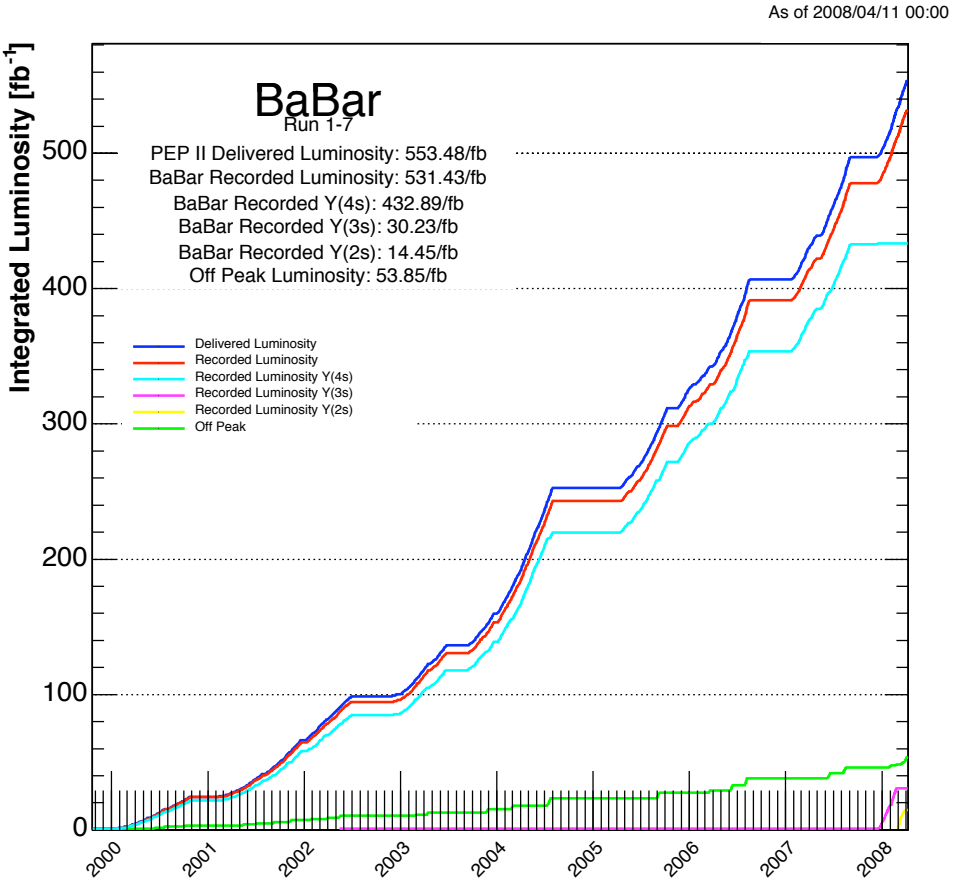

Figure 4.15: The integrated delivered and recorded luminosities at the BaBar detector. The different components, from top to bottom, are the luminosity where: PEP-II was operating (dark blue), data were taken (red), data were taken at the $\Upsilon(4S)$ resonance (light blue), data were taken $\sim 40\,\text{MeV}$ below the $\Upsilon(4S)$ resonance (green), data were taken at the $\Upsilon(3S)$ resonance (pink), and data were taken at the $\Upsilon(2S)$ resonance (yellow). (*The BaBar Collaboration* 2010)

Chapter 5

The electromagnetic calorimeter radiation monitoring system

5.1 Overview

This chapter outlines the hardware service task that the author completed as a member of the BaBar Collaboration. This service work concerns the radiation monitoring system for the BaBar electromagnetic calorimeter. The chapter opens with a motivation for the study, including a discussion of the dominant processes which make this study necessary. The operation of the hardware is discussed in detail, followed by a description of the data readout and storage techniques. The analysis of the absorbed dose is discussed, and the systematic uncertainties on the doses are outlined. The chapter concludes with an outlook for future work and how this study can inform other experiments.

5.2 Motivation

The performances of the crystals in the electromagnetic calorimeter are sensitive to degradation from ionising radiation. As particles and photons pass through the crystals they can ionise the CsI(Tl) atoms. These interactions can lead to changes in the behaviour of the crystals, such as colour centres resulting in changes in light

transmission in the crystals. These changes affect the energy resolution in the crystals and decreasing light yield, leading to larger uncertainties in shower energies. Therefore it is important to measure the dose absorbed by the crystals in the electromagnetic calorimeter. The electromagnetic calorimeter radiation monitoring system was designed to measure the absorbed dose throughout the electromagnetic calorimeter throughout the lifetime of the experiment. 116 radiation sensitive field effect transistors (radFETs) were placed throughout the detector.

5.3 Sources of radiation

The most significant source of radiation in the electromagnetic calorimeter accounting for 45% of all background, came from interactions between particles in the beams and residual gas particles in the vacuum during injection from the PEP-II accelerator. Other sources include Bhabha scattering processes, passage of particles produced at the interaction point and cosmic rays.

5.4 radFETs and their operation

The radFETs are $p-$channel metal oxide semiconductor field effect transistors which collect positive space charge (Holmes-Siedle 1986). A schematic overview of a radFET is shown in figure 5.1. As ionising radiation traverses the radFET, electron-positron pairs are produced. The positrons annihilate with electrons to form holes, which are then trapped in a silicon dioxide layer. This charge accumulates in defects in the SiO_2 layer, creating a negative image charge, and a corresponding shift in the threshold voltage of the radFET, ΔV. This shift in voltage can be measured by applying a constant current to the gate, as shown in figure 5.2. The voltage at the readout gate then reflects the dose absorbed by the radFET. When the voltage is read a small amount of charge at the SiO_2/Si oxide layer escapes, leading to a small change in the voltage. This effect is transitory and necessitates a short delay between switching the gate on and taking a reading (Camanzi 2001).

The relationship between the absorbed dose and voltage was obtained by irradiating some radFETs with known doses from samples of ^{60}Co source with intensities 2 Ci and 20 Ci (Camanzi 2001). The resulting calibration curve is shown in figure 5.3. In the region of interest ($\Delta V < 2$ V) the calibration curve can be modelled as a

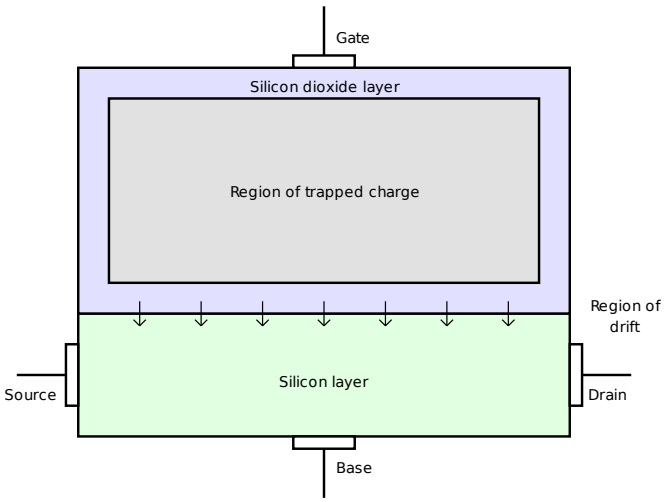

Figure 5.1: Schematic diagram of a radFET.

quadratic curve of the form:

$$D = \alpha \Delta V + \beta (\Delta V)^2 \tag{5.1}$$

where D is the absobed dose, $\alpha = 626.3 \pm 32.1\,\mathrm{radV}^{-1}$, and $\beta = 721.8 \pm 55.9\,\mathrm{radV}^{-2}$.

The radFETs are arranged in groups, each connected to a radFET monitoring board. As the dose on the radFETs increased the radFET monitoring board base voltages were changed so that the readout voltage remained sensitive to changes in dose.

5.4.1 Temperature dependence

The radFETs are reversibly sensitive to changes in temperature with a linear temperature dependence in the region $-20\,^{\circ}\mathrm{C} < \theta < 50\,^{\circ}\mathrm{C}$, with a temperature coefficient

$$k_T = -2.3 \pm 0.3\,\mathrm{mVK}^{-1} \tag{5.2}$$

The temperature in the detector is recorded so that this effect can be taken into account.

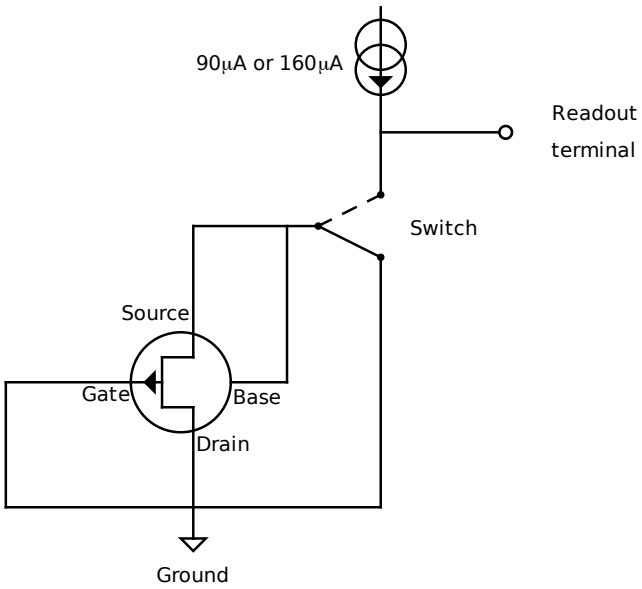

Figure 5.2: Readout principle of the radFETs. This diagram shows a radFET when not in use. The dashed line indicates the position of switch when the voltage is being read. (Khan 2005)

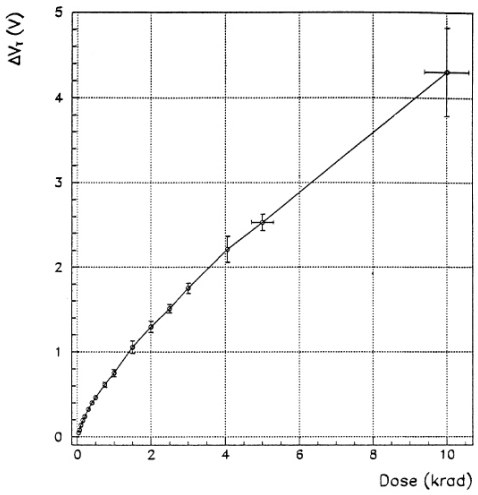

Figure 5.3: Calibration curve of the radFETs. (Camanzi 2001)

5.4.2 Hardware replacement

During the course of the experiment there have been a number of hardware faults in the electromagnetic calorimeter radiation monitoring system. Magnetic fields in the BaBar detector created shear forces on the wiring in some regions of the radFET system, breaking connections between components. During these times the radFETs

continued to accumulate dose, although it not possible to directly read the increase in dose in real time. In 2002 the radFET monitoring boards were replaced to overcome these issues.

5.4.3 Predicted and budgeted levels of dose

The BaBar Technical Design Report (Boutigny 2003) provided estimates for the expected dose absorbed by the radFETs during the course of the experiment. The estimates state that the barrel region of the electromagnetic calorimeter should receive approximately $1\,\mathrm{krad\,year^{-1}}$ and that the endcap region of the electromagnetic calorimeter should receive approximately $10\,\mathrm{krad\,year^{-1}}$. During normal running this was found to be an overestimate of the absorbed dose and the budgeted dose was adjusted to 10 krad for the whole experiment, with a dose per luminosity of $4 - 12\,\mathrm{rad\,fb^{-1}}$(Hrynova 2003).

5.4.4 Data readout procedure

Data were monitored and recorded whenever there would be an appreciable change in readout potential difference across a radFET. This change in potential difference was configurable and typically $\sim$ mV. This provided excellent radiation resolution while reducing electronic noise in the system. The data would then be stored to disk, with information about the time and the temperature of electromagnetic calorimeter.

5.5 Analysis of absorbed dose

The data from the radFETs are analysed as a function of time (with the dose read daily), delivered luminosity and region of the electromagnetic calorimeter. For the purposes of this study the electromagnetic calorimeter is divided into East and West halves in the barrel and endcap regions, where each region corresponds to a different radFET monitoring board. The data are corrected for temperature variations according to equation 5.2.

Due to changes in hardware and general maintenance the potential differences on the radFET monitoring boards would occasionally experience large discontinuities. These discontinuities are eliminated by subtracting the difference and adding the average daily dose absorbed for the relevant running period on a per radFET basis.

During periods of radFET monitoring board failure the radFETs attached to

the radFET monitoring board could not be read, although they would continue to accumulate dose. During these periods the absorbed dose is estimated by observing the change in dose on the other side of the detector in the East-West direction. This change in dose is multiplied by the ratio of changes of dose for both sides of the detector for the previous running period.

After applying these corrections the average absorbed doses in each region are shown in figure 5.4 as a function of time and in figure 5.5 as a function of delivered luminosity.

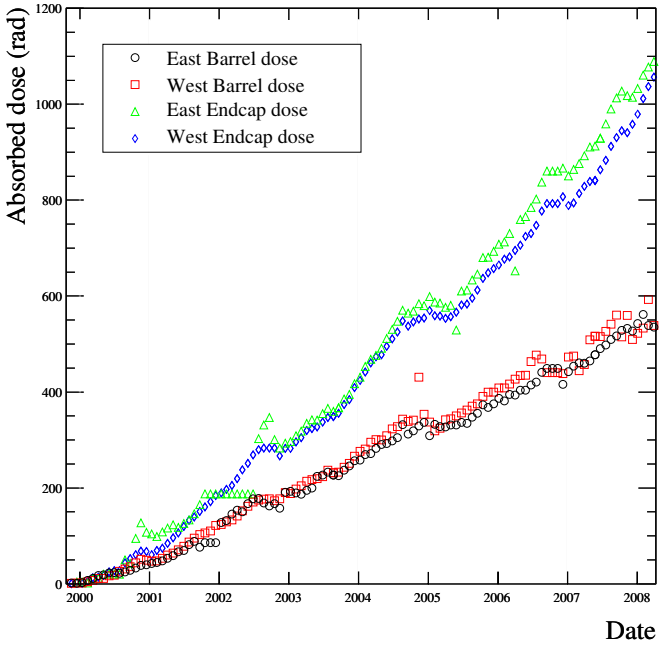

Figure 5.4: Absorbed dose in the electromagnetic calorimeter as a function of date.

Due to the energies of the PEP-II beams the BaBar detector was asymmetric, with a Lorentz boost of $\beta\gamma = 0.56$. This would lead to the forward regions of the electromagnetic calorimeter receiving a higher dose than the backward regions. Most of the damaging radiation would arise from shallow scattering of the beams, with the higher energy electron beam causing more damage and at smaller polar angles. For this reason the endcap regions are further divided into the inner, centre and outer rings. The average dose is then calculated for each of the eight regions by taking the sample mean of functioning radFETs in that region. These doses are showed in table 5.1

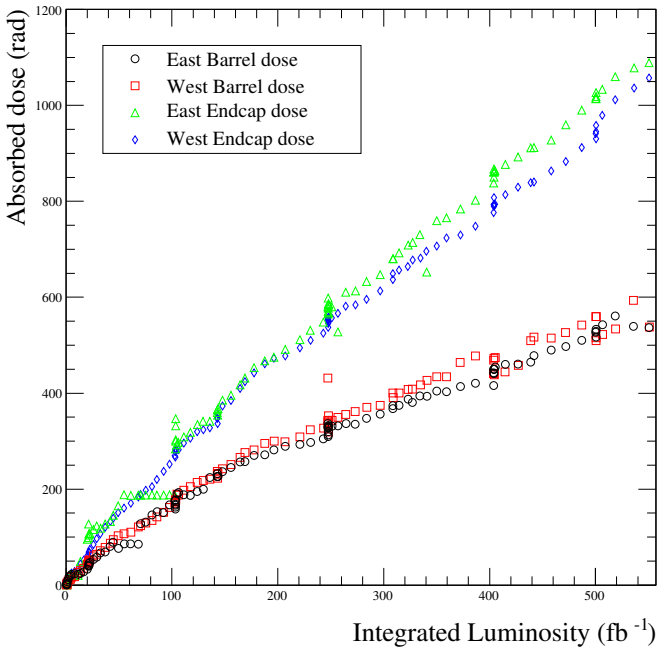

Figure 5.5: Absorbed dose in the electromagnetic calorimeter as a function of integrated delivered luminosity.

5.6 Systematic uncertainties

There are four main sources of uncertainty when determining the dose absorbed by the radFETs:

- The calibration of the radFETs.
- The standard error on the mean value for each region.
- The uncertainty on the temperature coefficient.
- The uncertainty introduced from removal of discontinuities in the absorbed dose.

5.6.1 Calibration

The uncertainty introduced by the calibration curve of the radFETs is determined by adding the uncertainty introduced by the constants in α and β from equations 5.1 in quadrature:

$$\delta D = \sqrt{(\Delta V \delta\alpha)^2 + (\Delta V^2 \delta\beta)^2} \tag{5.3}$$

where δD is the change in absorbed dose.

Table 5.1: Absorbed dose in the electromagnetic calorimeter at the end of each combined running period by region in units of rads.

Domain	Run 1	Run 2	Run 3	Run 4	Run 5	Run 6	Run 7
East barrel	38.2	180.2	214.8	318.3	441.1	516.9	540.4
West barrel	46.6	172, 7	230.7	334.3	470.9	554.3	591.3
Inner East endcap	120.6	225.2	489.3	783.6	1210.6	1458.1	1578.3
Centre East endcap	105.0	176.0	372.1	568.7	844.6	1012.7	1093.1
Outer East endcap	90.5	140.5	280.5	411.2	589.5	697.2	750.7
Inner West endcap	90.6	375.8	478.1	760.1	1129.3	1244.8	1511.9
Centre West endcap	59.6	245.3	304.0	477.1	695.7	825.0	946.0
Outer West endcap	45.0	186.6	225.3	345.7	494.8	585.0	676.6

5.6.2 Statistical uncertainty

When taking the average absorbed dose for each region the standard error on the mean, $\sigma/\sqrt{n}$, is taken as the statistical uncertainty where

$$\sigma^2 = \frac{\sum D^2 - \left(\sum D\right)^2 / n}{n-1} \tag{5.4}$$

and n is the number of functioning radFETs in the region.

5.6.3 Temperature coefficient

The uncertainty on the temperature coefficient introduces an uncertainty of $\delta k_T \Delta T$, where δk_T is the uncertainty on the temperature coefficient and $\Delta T = T - 21^\circ$ C.

5.6.4 Discontinuity corrections

When correcting for discontinuities in the absorbed dose distribution the absorbed dose is estimated by taking the average daily change in absorbed dose for the relevant run. The uncertainty on this change is estimated by calculating the standard deviation of the daily increase in dose for that running period.

5.6.5 Summary of systematic uncertainties

The systematic uncertainties at the end of run 7 are outlined in table 5.2. With the exception of the West barrel, the total uncertainties are dominated by the uncer-

Table 5.2: Uncertainties on the absorbed dose in the electromagnetic calorimeter at the end of run 7 by region in units of rads. σ_C refers to the systematic uncertainty associated with the calibration of the radFETs, σ_{stat} refers to the standard error on the mean taken when averaging over functioning radFETs, σ_T refers to the systematic uncertainty associated with the temperature correction, σ_D is the systematic uncertainty associated with the discontinuity corrections, and σ_{total} is the sum of these uncertainties added in quadrature.

Domain	Average absorbed dose	σ_T	σ_D	σ_C	σ_{stat}	σ_{total}
East barrel	540.4	0.6	42.4	23.4	11.9	49.8
West barrel	591.3	0.1	104.5	25.4	15.9	108.8
Inner East endcap	1578.3	0.1	26.3	76.7	72.7	108.9
Centre East endcap	1093.1	0.1	25.1	50.3	55.6	79.1
Outer East endcap	750.7	0.1	20.5	33.2	26.5	47.2
Inner West endcap	1511.9	0.1	17.7	73.0	61.1	96.8
Centre West endcap	946.5	0.1	14.3	42.9	44.7	63.6
Outer West endcap	675.5	0.1	14.8	29.4	40.8	52.4

tainties in the calibration of the radFETs, with the uncertainties due to temperature variations being negligible.

5.7 Effect on light yield

As the crystals in the electromagnetic calorimeter are irradiated, their light yields decrease. Studies using data from the early running periods of BaBar have shown this effect is not negligible (Bauer 2003). Figure 5.6 shows the result of such a study, indicating a change in light yield of approximately 10%. The work presented in this thesis will be used to inform further light yield studies, indicating changes in light yield over the course of the experiment.

5.8 Conclusions

The dose absorbed by the electromagnetic calorimeter is much lower than predicted in the BaBar Technical Design Report. The dose per luminosity for the most radiated crystals is $2.8 \pm 0.2\,\mathrm{rad\,fb^{-1}}$, which is below the budgeted dose of $4 - 12\,\mathrm{rad\,fb^{-1}}$. The performance of the electromagnetic calorimeter in a high radiation environment for long periods of time has exceeded expectations and similar results should be antici-

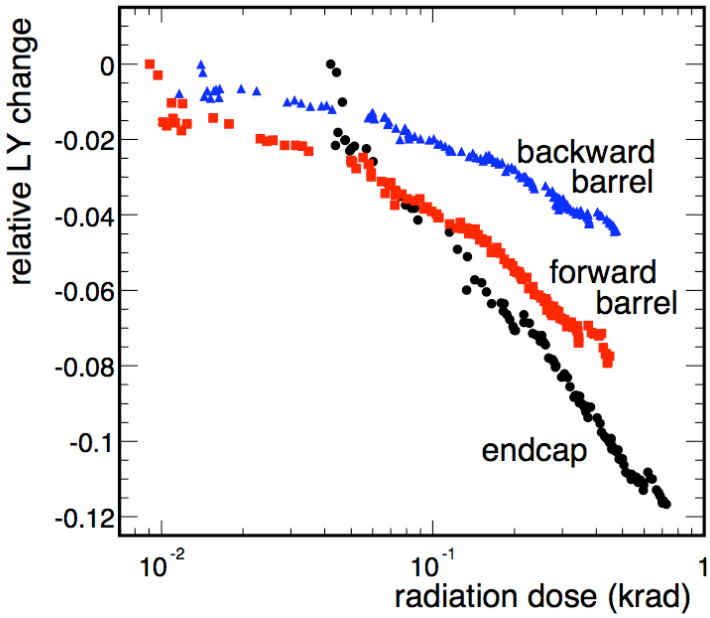

Figure 5.6: Light yield of crystals in the electromagnetic calorimeter as a function of the absorbed dose. LY refers to the light yield. Blue triangles correspond to the backward region of the barrel. Red s quares correspond to the forward region of the barrel. Black circles correspond to the endcap. (Bauer 2003)

pated for future experiments, most notably the SuperB experiment, which anticipates a dose of $1\,\mathrm{kradyr}^{-1}$ (Bona 2007).

5.9 Summary

The BaBar electromagnetic calorimeter has been monitored closely throughout the experiment, allowing a detailed study of the response of the electromagnetic calorimeter to incident radiation. The study of the dose absorbed by the electromagnetic calorimeter has shown that the predicted doses have been pessimistic. This study can be used to inform future experiments about the expectation of absorbed dose in high radiation environments.

Chapter 6

Analysis methods

6.1 Overview

This chapter introduces a series of useful analysis methods which use the BaBar dataset to extract measurements of interesting physical parameters. Much of the content of this chapter requires some knowledge of the BaBar detector and data storage systems, as described in previous chapters. The software environment of the BaBar experiment is described, including a detailed outline of the simulation environments. The remainder of the chapter is concerned with the reconstruction of physics events and identification of particle species. The methods described have been developed for the BaBar Collaboration, although similar techniques are used on other similar experiments.

6.2 Software environment

The BaBar experiment benefits from extensive software support. A large array of fast CPUs is available to all users via a batch system.

6.2.1 The ROOT framework

The ROOT framework is a collection of software tools developed for use in high energy physics at CERN (Brun 2010). Much of the analysis presented in this thesis, including the graphical representations was prepared using the ROOT framework.

Yield extraction

Estimates of the yields of signal events are extracted by performing fits to spectra of data. If the distributions of signal and background reconstructions are well known, and the spectrum in the data has sufficiently high statistics then a precise estimate of the yield of signal events can be determined. A software package called `Roofit` has been developed by the BaBar Collaboration, in order to facilitate such yield extractions (Verkerke & Kirby 2006). The `Roofit` package uses the likelihood formalism to obtain the most probable distribution given a model of the form

$$D = f_S S + \sum_i f_B^i B_i \tag{6.1}$$

where D is the observed distribution in data, S is the probability density function for signal events, f_S is the fraction of events in data which are signal events, B_i are the probability density functions for various components of background, and f_B^i are the fractions of these events in the data.

6.2.2 The BaBar software framework

Many tools common to several analyses are available in a framework known as the `beta` environment. This allows physicists to access and manipulate data sets, building on knowledge, experience and techniques from earlier works. The majority of the work performed in the beta environment is object oriented and CPU intensive. Most of the software is developed using the `C++` language.

The `DRecoilToolsUser` package

A software package called `DRecoilToolsUser` has been developed specifically for this analysis. This package manipulates the data and simulated event collections in order to extract the relevant parameters needed to calculate the branching fractions $\mathcal{B}(D_s \to \ell\nu_\ell)$.

6.3 Multivariate optimisation

A software package called `StatPatternRecognition` was developed to assist with multivariate analyses (Narsky 2005)(Narsky 2006). This analysis uses a tool called `BumpHunter` from the `StatPatternRecognition` package. The `BumpHunter` algorithm

searches for a series of selection criteria that define an $n-$dimensional cuboid in $n-$dimensional variable space. Once a suitable region is found the selection criteria are adjusted to optimize the figure of merit, θ, such that the proportion of the number of events excluded by this adjustment does not exceed a fixed amount. This amount is known as the peel parameter. The process is repeated until a cuboid is found which maximizes the figure of merit.

An example distribution is included to illustrate the nature of the algorithm. Figure 6.1 shows the example distribution in a space of two arbitrary variables, (x, y). Correctly reconstructed signal points are distributed according to a two dimensional probability density function, $P(x, y) = G_1(\mu_1, \sigma_1) \times G_2(\mu_2, \sigma_2)$, where G_i is a Gaussian distribution with mean μ_i and standard deviation σ_i. Incorrectly reconstructed signal points have a uniform distribution across the space. Background points also have a uniform distribution across the space.

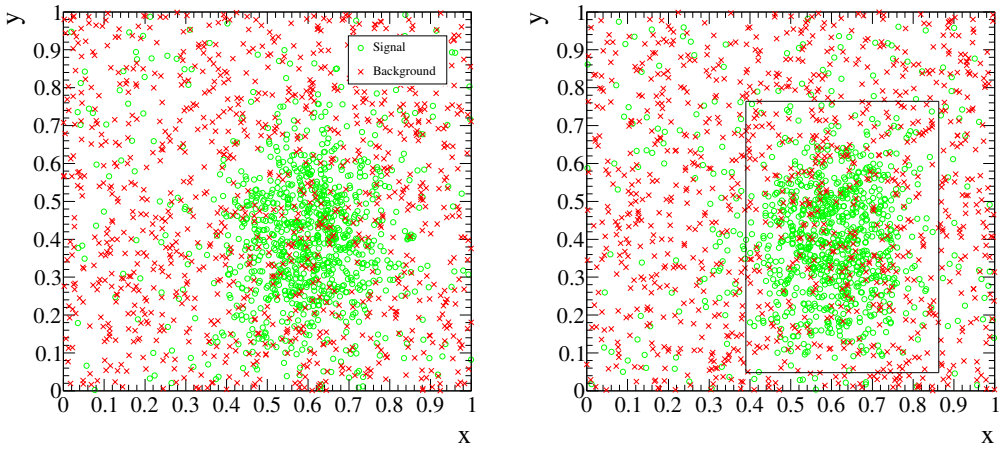

Figure 6.1: Example training (left) and testing (right) samples for the `BumpHunter` algorithm. Green circles indicate signal points and red crosses indicate background points in an arbitrary space (x, y). The black box indicates the resulting selection criteria.

The chosen figure of merit for this study is the significance, θ:

$$\theta = \frac{N_S}{\sqrt{N_S + N_B}} \tag{6.2}$$

where N_S is the number of signal points, and N_B is the number of background points. `BumpHunter` is trained on one sample of $1,000$ points (of which 500 are signal points) in order to find an optimal set of selection criteria for the chosen figure of merit. To avoid bias the figure of merit is estimated by applying the selection criteria to

an independent testing sample of points. As shown in figure 6.1 the algorithm has determined that the region enclosed by $0.39 < x < 0.86$ and $0.05 < y < 0.76$ gives the optimal value for the significance. The algorithm can be tested for robustness by varying the weight of signal points and by varying the peel parameter.

6.4 Monte Carlo simulation

In order to best understand the BaBar detector and the data set, a series of simulations are used, which are referred to as Monte Carlo simulations.

6.4.1 Physics simulation

Using data obtained from existing physics measurements (often using the Particle Data Group) different events are simulated. These simulations are model dependent, with Standard Model processes taken as default, unless otherwise stated. Event simulations are grouped into collection. The following generic processes are modelled and grouped into collections:

- $e^+e^- \to e^+e^-(\gamma)$ (Not used in this analysis)
- $e^+e^- \to \mu^+\mu^-(\gamma)$ (Not used in this analysis)
- $e^+e^- \to \tau^+\tau^-$
- $e^+e^- \to u\bar{u}/d\bar{d}/s\bar{s}$
- $e^+e^- \to c\bar{c}$
- $e^+e^- \to B^+B^-$
- $e^+e^- \to B^0\bar{B}^0$

The simulation proceeds by allowing each unstable particle (excluding the neutral kaons) to decay according to its Standard Model expectations for branching fraction, lifetime and dominant process.

In many instances a process where the branching fraction has not been measured by any experiment will be included. In such cases the branching fraction is often estimated using symmetry laws (such as isospin symmetry), by taking current experimental limits, or by using ratios of Cabibbo-Kobayashi-Maskawa element products. In some cases a process will be included which is forbidden by symmetry laws, or a

Table 6.1: Large statistics Monte Carlo samples which are used in this analysis. X refers to any system of particles consistent with the decays outlined in generic Monte Carlo collections.

Simulation production number	Decay chain $e^+e^- \to c\bar{c}; c\bar{c} \to D_s^\star X; D_s^\star \to D_s\gamma; \ldots$
$SP-3046$	$D_s^+ \to \mu^+\nu_\mu$
$SP-3047$	$D_s^- \to \mu^-\bar{\nu}_\mu$
$SP-3046$	$D_s^+ \to e^+\nu_e$
$SP-3047$	$D_s^- \to e^-\bar{\nu}_e$
$SP-3046$	$D_s^+ \to \tau^+\nu_\mu; \tau^+ \to \mu^+\bar{\nu}_\tau\nu_\mu$
$SP-3047$	$D_s^- \to \tau^-\bar{\nu}_\tau; \tau^- \to \mu^-\nu_\tau\bar{\nu}_\mu$
$SP-3046$	$D_s^+ \to \tau^+\nu_\mu; \tau^+ \to e^+\bar{\nu}_\tau\nu_e$
$SP-3047$	$D_s^- \to \tau^-\bar{\nu}_\tau; \tau^- \to e^-\nu_\tau\bar{\nu}_e$

known process will not be included. The Monte Carlo simulation is continually updated in an attempt to minimise and correct these effects. However it is unreasonable to expect that a Monte Carlo simulation will ever be able to model the underlying physics events perfectly.

When the simulation includes light quark pairs ($u\bar{u}/d\bar{d}/s\bar{s}$ and $c\bar{c}$) the quark pairs are forced to decay into multihadron states (hadronise) by creating additional quark-antiquark pairs, as described in section 2.6.5. This process is not well understood as the quantum chromodynamical processes are non-perturbative due to the large coupling of the strong force.

At each stage in the 'decay chain' if there is a charged particle present there is a chance that it will radiate a photon. This is known as final state radiation.

In addition to the generic Monte Carlo, the physics processes in table 6.1 are simulated. The Monte Carlo simulations are each uniquely identified with a simulation production code, which is assigned sequentially as the simulations are created. These Monte Carlo collections are used to perform a wide range of studies.

6.4.2 Hardware simulation

The resulting Monte Carlo simulation is then passed onto another simulation module called `GEANT4` (Allison 2006) which models the interaction of these simulated particles with the detector and other hardware. At this stage of the simulation the neutral

kaons are decayed as outlined above. Interactions with the hardware can lead to loss of energy for particles, and deviations in the trajectory which are relatively well modelled, and interactions leading to the creation of new particles or the ejection of particles from the hardware matter which are relatively poorly modelled.

Hardware simulation is CPU intensive and there are many CPU batch farms around the world dedicated to production of Monte Carlo simulation. Figure 6.2 shows a simulated event and the interactions between the particles and detector.

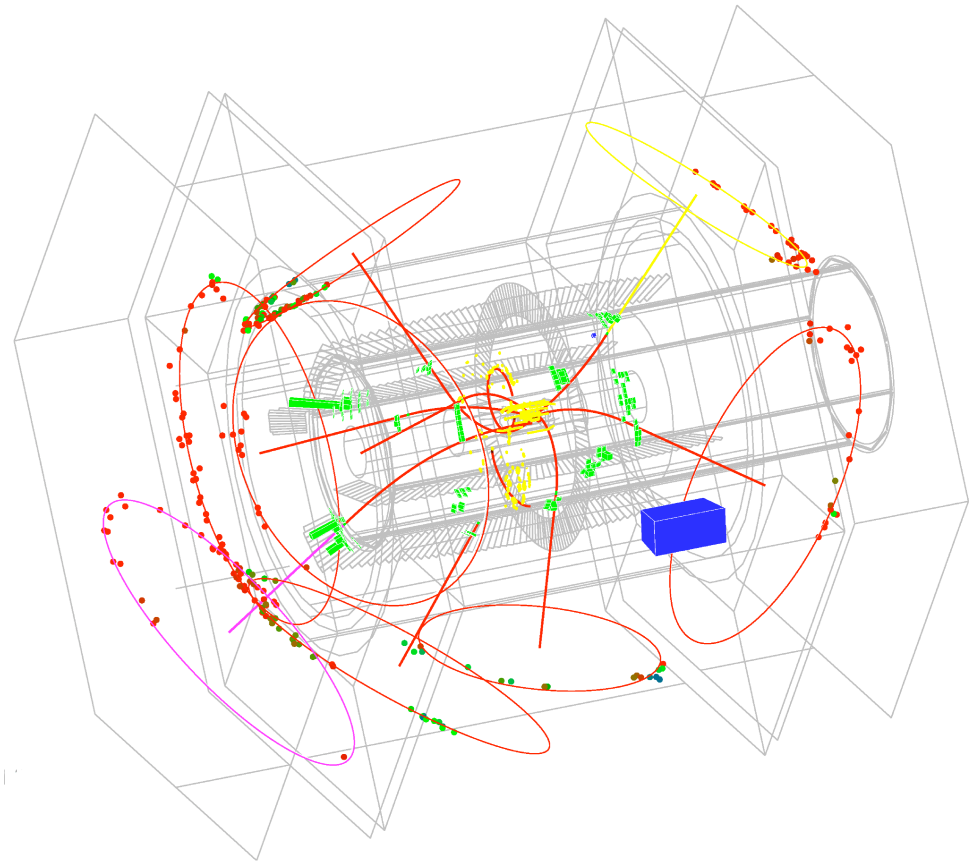

Figure 6.2: A simulation of a charm production event ($e^+e^- \rightarrow c\bar{c}$) in the BaBar detector. The red paths show particle trajectories. The blue and green rectangles show energy deposition in the electromagnetic calorimeter. The coloured circles show rings of Čerenkov radiation in the DIRC. (*The BaBar Collaboration* 2010)

6.4.3 Weighting of Monte Carlo simulated events

One of the purposes of the Monte Carlo simulation is to provide high statistics samples of simulated events of a given type. The number of generic Monte Carlo events generated is motivated by the relative importance of the type of event to the BaBar Collaboration as a whole, efficiencies in event reconstruction and the cross sections of

Table 6.2: Effective luminosities for the generic Monte Carlo samples. The cross-sections are taken from the BaBar Physics Book. (Harrison 1999)

Generic physics process	Effective luminosity (fb^{-1})	Ratio of effective luminosity to luminosity of data
$e^+e^- \to \tau^+\tau^-$	851.4	1.6
$e^+e^- \to u\bar{u}/d\bar{d}/s\bar{s}$	935.0	1.8
$e^+e^- \to c\bar{c}$	1060.1	2.0
$e^+e^- \to B^+B^-$	1350.0	2.5
$e^+e^- \to B^0\bar{B}^0$	1368.2	2.6

the various processes. As a result the Monte Carlo events are produced in unrealistic ratios and must be reweighted to match the distributions observed in data. This weighting is estimated assuming the cross sections of the various processes. Events of the type $e^+e^- \to c\bar{c}$ are further reweighted so that the hadronisation processes in the Monte Carlo distributions match those of data. The effective integrated luminosity, $\mathcal{L}_{eff}$, of a sample of simulated events can be determined by dividing the number of events in the sample, N, by the cross-section, σ:

$$\mathcal{L}_{eff} = \frac{N}{\sigma} \tag{6.3}$$

The effective integrated luminosities of the generic Monte Carlo samples used by the BaBar Collaboration are given in table 6.2

6.5 Tracking

As discussed in section 4.2, as particles pass through the detector and interact with the subsystems the information taken from the various subsystems is collated and used to reconstruct candidate trajectories. There are various strategies for reconstructing such trajectories, depending on the subsystems used and the nature of the interactions. Interactions in the subsystems are referred to as hits.

6.5.1 Trajectory helices

A trajectory is modelled as a helical path, P, with five parameters and one variable:

$$P = P(f; d_0, \phi_0, \omega, z_0, \tan\lambda) \tag{6.4}$$

where f is the flight length along the trajectory (the signed distance along the trajectory from the point of closest approach to the z-axis, where the coordinate system is defined in figures 4.2 and 4.3), d_0 is the distance of closest approach of the trajectory to the z-axis, ϕ_0 is the ϕ coordinate of the trajectory at this point, z_0 is the z coordinate of the trajectory at this point, ω is the inverse of the radius of the helix, and λ is the co-polar angle of the trajectory. λ is very small and can be approximated to 0. These parameters are shown in figures 6.3 and 6.4.

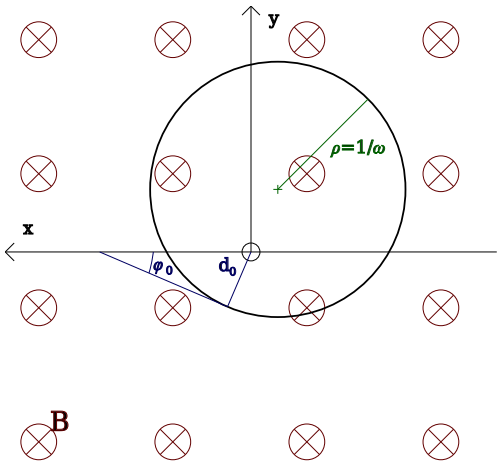

Figure 6.3: Transverse view of a particle's helical trajectory. ω is the inverse of the radius of curvature of the helix, d_0 is the distance of closest approach of the helix to the z axis, and ϕ_0 is the angle of trajectory at this point.

Using these variables gives the equations of the trajectory in Cartesian coordinates

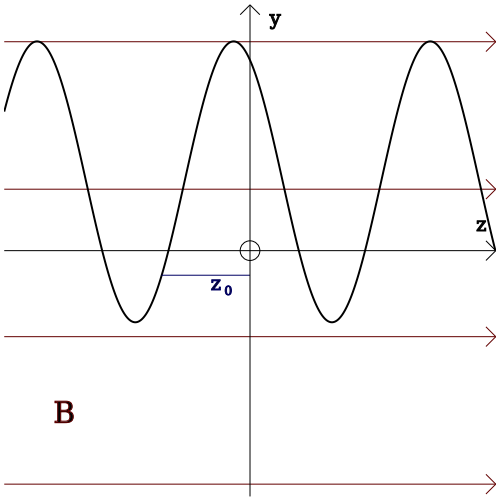

Figure 6.4: Longitudinal view of a particle's helical trajectory. z_0 indicates the z component of the position of the point of closest approach of the helix to the z axis.

as:

$$\begin{pmatrix} x \\ y \\ z \end{pmatrix} = \begin{pmatrix} \frac{1}{\omega}\sin(\phi_0 + \omega f) - \left(\frac{1}{\omega} + d_0\right)\sin\phi_0 \\ -\frac{1}{\omega}\cos(\phi_0 + \omega f) - \left(\frac{1}{\omega} + d_0\right)\cos\phi_0 \\ z_0 + f + v_z t \end{pmatrix} \tag{6.5}$$

where v_z is the z component of the velocity of the particle, and t is time elapsed since the interaction.

Using information from the hits in the drift chamber the candidate trajectory is fitted, minimising the χ^2 of the fit to the hits. The positions of the hits are represented by a vector, H, and the hypothesised helix, P, is described by a vector, $h(P)$, corresponding to the same detector components (wires, wafers etc) to those in H. The χ^2 is then defined as:

$$\chi^2 = \sum_i \frac{H_i - h_i(P)}{\sigma_i(H_i - h_i(P))} \tag{6.6}$$

The passage of a trajectory through the detector must take material effects and field effects into account. A simple helix model assumes that as the particle flies along the trajectory it will not lose energy or interact with the detector material. Such a model also assumes that the magnetic field is exactly parallel to the z-axis. In reality neither assumption is true and a simple helical path is not sufficient to model the trajectory of particle.

To overcome these limitations of the model, additional parameters are added to

take various effects into account. The fit used is a Kalman fit (Kalman 1960), which minimises χ^2 progressively, adding measurements one at a time, in the order they appear in the candidate trajectory. A typical fit can have ~ 100 such parameters and H can have a similar number of constraints.

6.5.2 Tracking efficiency

The efficiency associated with reconstructing a charged candidate (the tracking efficiency) is determined using a control sample of events of the type $e^+e^- \to \tau^+\tau^-$, where the τ leptons decay to one or three pions and a neutrino. The other τ lepton is required to decay to a to a leptonic final state ($\mu\nu_\tau\bar{\nu_\mu}$ or $e\nu_\tau\bar{\nu_e}$, and their charge conjugates). The cross sections and branching fractions for all of these process are well known, and due to the kinematic constraints these events are easily separated from events arising from other processes. These events provide the tracking efficiency over a large range of momenta and angular distribution. The tracking efficiency is calculated by the BaBar Tracking Efficiency Task Force and is quoted for each run per track in the reconstruction. Figure 6.5 shows the event topologies for $1-1$ and $3-1$ tracking study events.

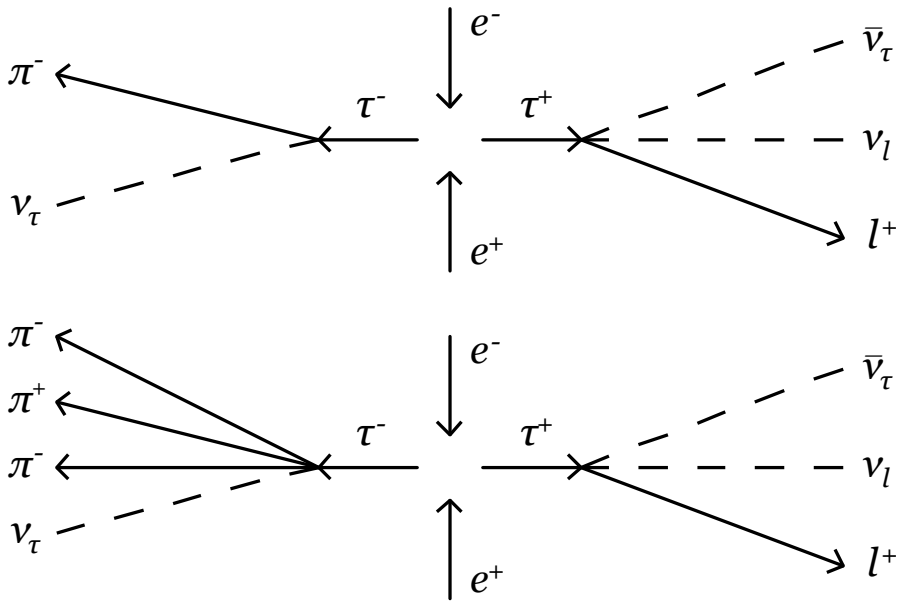

Figure 6.5: The topologies of $1-1$ and $1-3$ events used by the BaBar Tracking Efficiency Task Force to determine tracking efficiencies.

6.6 Vertex reconstruction

When considering a system of particles it is possible to improve the resolution of the momenta and energies of the particles by applying kinematic or geometric constraints. This process is known as vertex reconstruction. Two different vertex reconstruction algorithms are used in this analysis. The `Cascade` algorithm is relatively fast and is used for very large samples of reconstruction. The `TreeFitter` algorithm is more accurate and used for reconstructions which are used to obtain the final results.

When reconstructing vertices, 'daughter' particle candidates are combined to form 'mother' particle candidates. This process can be used recursively, resulting in a decay tree with several vertices.

6.6.1 General method

In the limit where the physical material in the detector is thin the trajectory of a charged particle can be approximated as a helix with five parameters. This five parameter helix is then converted into a six parameter $x - p$ representation, where x describes the spatial positions of the particles and p describes the momenta of the particles. The advantages of this representation are the simplicity of the calculations and the more natural interpretation of the measured quantities. Since there are six parameters in the $x - p$ representation, but only five parameters in the helical representation not all of the six parameters are independent. The $x-p$ representation is local in the sense that the parameters are meaningful only when referring to a given point in space.

The measurable quantities are described by a vector $\vec{\eta}$, whereas the recorded quantities are described a vector $\vec{y}$, where $\vec{y}$ and $\vec{\eta}$ are related by

$$\vec{y} = \vec{\eta} + \vec{\delta} \tag{6.7}$$

where $\vec{\delta}$ is a vector of uncertainties, assumed to be normally distributed. The unknown true quantities are described by a vector $\vec{X}$, which has r components. A series of m constraints are applied to $\vec{\eta}$, $\vec{y}$ and $\vec{X}$ to obtain a functional, f:

$$f_k(\vec{X}, \vec{\eta}) = f_k(\vec{X}, \vec{y} + \vec{\delta}) = 0 \tag{6.8}$$

The derivatives of f are described using the notation

$$a_{kl} = \left(\frac{\partial f_k}{\partial x_l}\right) \tag{6.9}$$

$$b_{kl} = \left(\frac{\partial f_k}{\partial \eta_l}\right) \tag{6.10}$$

where a_{kl} and b_{kl} are elements of the matrices $\bar{A}$ and $\bar{B}$ at a given point (x_0, η_0). The constraints can be expressed in a vector $\vec{c}$ where $c_k = f_k(\vec{X}_0, \vec{\eta}_0)$.

Expanding using a Taylor series about the point (x_0, η_0), the sum of squares of differences, χ^2 is then

$$\chi^2 = \vec{\delta}^T \bar{W}_y \vec{\delta} + 2\vec{\mu}^T \left(\bar{A}\vec{\epsilon} + \bar{B}\vec{\delta} + \bar{c}\right) \tag{6.11}$$

where $\vec{\mu}$ is the vector of Lagrange multipliers, and $\vec{\epsilon} = \vec{X} - \vec{X}_0$, $\vec{\delta} = \vec{\eta} - \vec{\eta}_0$.

For the first iteration the value of $\vec{\eta}_0$ is taken to be $\vec{\eta}_0 = \vec{y}$. For short lived particles the value of $\vec{X}_0$ can be taken to be the interaction region. For longer lived particles the point of closest approach of the relevant helices is used. After extensive manipulation the minimal value of χ^2 is found to be

$$\chi^2_{\min} = \vec{\delta}^T \left(\bar{B}^T \left(\bar{B}\bar{W}_y^{-1}\bar{B}^T\right)^{-1} \bar{B}\right) \vec{\delta} \tag{6.12}$$

By varying the momenta of the particle candidates to minimise the χ^2 of the vertex reconstruction properly reconstructed candidates will tend to provide more precise information about the momenta of the particles.

6.6.2 Constraints

A number of different constraints can be applied to vertex reconstructions, listed below. The suitability and relevance of each of these constraints depends upon the decay being described by the decay chain.

Pseudo-momentum

The momentum at each vertex in a decay chain must be conserved. For a mother particle candidate, M, reconstructed from daughter particle candidates, d_i, the constraint reads

$$f_i(\vec{X}, \vec{\eta}) = \sum_j p_{ij} - p_i = 0 \tag{6.13}$$

where i refers to the axes of the Cartesian coordinate system, j refers to the daughter particle candidates, p_{ij} refers to the ith component of momentum for the jth daughter particle candidate, and p_i refers to the ith component of momentum for the mother particle candidate.

Momentum

The momentum of the system of particles in a given frame of reference, specified by a Lorentz boost, $\vec{\beta}$, gives a constraint which reads

$$f(\vec{X},\vec{\eta}) = \begin{pmatrix} \gamma\beta_x & 1+\Gamma\frac{\beta_x^2}{\beta^2} & \Gamma\frac{\beta_x\beta_y}{\beta^2} & \Gamma\frac{\beta_x\beta_z}{\beta^2} \\ \gamma\beta_y & \Gamma\frac{\beta_y\beta_z}{\beta^2} & 1+\Gamma\frac{\beta_x^2}{\beta^2} & \Gamma\frac{\beta_y\beta_z}{\beta^2} \\ -\gamma\beta_z & \Gamma\frac{\beta_z\beta_x}{\beta^2} & \Gamma\frac{\beta_z\beta_y}{\beta^2} & 1+\Gamma\frac{\beta_x^2}{\beta^2} \end{pmatrix} \begin{pmatrix} E \\ p_x \\ p_y \\ p_z \end{pmatrix} - \begin{pmatrix} p_x^c \\ p_y^c \\ p_z^c \end{pmatrix} \tag{6.14}$$

where p_i^c are the constrained components of the momentum, $\Gamma = \gamma - 1$, and each component of $f(\vec{X},\vec{\eta})$ is a component of equation 6.14.

Mass

The mass of a given particle candidate can be constrained. This constraint reads

$$f(\vec{X},\vec{\eta}) = E^2 - \vec{p}^2 = M^2 \tag{6.15}$$

where E is the energy of the candidate, $\vec{p}$ is the momentum of the candidate, and M is the mass of the candidate.

Beam-spot

The point of collision of the two beams in the BaBar detector is continually monitored and is called the beam-spot. The beam-spot constraint requires that the position of the vertex in the transverse plane is close to the transverse position of the beam-spot (compatible with uncertainties in this position.) The constraint reads

$$f(\vec{X},\vec{\eta}) = (x - x_{BS})^2 + (y - y_{BS})^2 \tag{6.16}$$

where x_{BS} and y_{BS} are the x and y components of the beam-spot.

Energy

The energy of a particle candidate in a given frame of reference, specified by a Lorentz boost, $\vec{\beta}$, can be constrained. This constraint reads

$$f(\vec{X}, \vec{\eta}) = \gamma E - \gamma\beta_x p_x - \gamma\beta_y p_y - \gamma\beta_z p_z - E^c \tag{6.17}$$

where E is the energy of the particle candidate, E^c is the constrained energy, and p_i are the components of the momentum of the particle candidate.

Beam energy

The energy of the candidates in the centre of mass frame must be equal to the energies of the beams (compatible with uncertainties in the beam energies.) This constraint reads

$$f(\vec{X}, \vec{\eta}) = (E_{e^+} + E_{e^-})\, E - (\vec{p}_{e^+} + \vec{p}_{e^-})\, \vec{p} - \sqrt{(E_{e^+} + E_{e^-})^2 - (\vec{p}_{e^+} + \vec{p}_{e^-})^2} \tag{6.18}$$

where $E_{e^\pm}$ and $\vec{p}^{\pm}$ are the energies and momenta of the e^+ and e^- beams respectively, and E and $\vec{p}$ are the energy and momenta of the system of particle candidates.

Zero-lifetime

A particle candidate can be forced to decay to its daughters at the point of production (the vertex of its mother particle.) This constraint reads

$$f(\vec{X}, \vec{\eta}) = (x - x_m)^2 + (y - y_m)^2 + (z - z_m)^2 \tag{6.19}$$

where x, y, z describe the position of the vertex of the particle candidate and x_m, y_m, z_m describe the position of the vertex of the mother particle candidate.

Line-of-flight

A particle candidate can be required to align its momentum in a given direction. This constraint reads

$$f(\vec{X}, \vec{\eta}) = x - x_0 - t_x s \tag{6.20}$$

where x_0 and t_x define the position and direction of the line of flight in the x direction and s is the distance along the path from the point x_0 (and similarly for the y and z

components.)

6.6.3 The `Cascade` vertex reconstruction algorithm

The `Cascade` vertex reconstruction algorithm includes two additional constraints:

Pseudo-energy

The energies of daughter particle candidates must sum to a constrained energy. This constraint reads

$$f(\vec{X}, \vec{\eta}) = \sum_i E_i - E^c \tag{6.21}$$

where E_i is the energy of the ith particle candidate, and E^c is the constrained energy.

Beam-spot intersection

The production vertex of a particle candidates must intersect with the beam-spot. This constraint reads

$$f(\vec{X}, \vec{\eta}) = x - \left(x_{BS} + \left(\frac{\tau}{m}\right) p_x\right) \tag{6.22}$$

where x_{BS} is the x position of the beam-spot, τ is the lifetime of the particle candidate, and m is the mass of the particle candidate (and similarly for the y and z components.)

6.6.4 The `TreeFitter` vertex reconstruction algorithm

The `TreeFitter` vertex reconstruction algorithm minimises the χ^2 for a given decay tree of arbitrary size and complexity. This makes the algorithm ideal for decay trees with many particles in the final state, and many intermediate particles. In particular `TreeFitter` is excellent for reconstructions which aim to model the entire physics event.

6.7 Particle identification

As discussed in section 4.10 different particles would interact with the BaBar detector in different characteristic ways. Using this information it is possible to form a hypothesis on the type of particle present for a given trajectory. Since this analysis measures the number of $D_s \to \ell\nu$ events relative to the inclusive number of events containing a D_s meson, all of the uncertainties associated with the efficiencies of particle identification cancel out exactly, except for those of the charged lepton. Forming a hypothesis about the identity of a particle candidate requires the reconstruction of a charged track.

6.7.1 General method

The Particle Identification Working Group of BaBar has developed techniques for forming hypotheses about true particle species. The general strategy for determining the efficiencies of these techniques is:

- Determine a control sample of events where the particle species is easily and reliably isolated in data.
- Model this control sample using a Monte Carlo sample.
- Compare the efficiencies between the data and Monte Carlo control samples.
- Compare the efficiencies between the Monte Carlo control sample and the Monte Carlo sample pertaining to the analysis.

The Particle Identification Working Group analyses the efficiencies for both data and Monte Carlo control samples and collates the results. Using these results it is possible to determine the ratio of efficiencies between data and Monte Carlo samples and hence determine the efficiency of the particle identification procedure for any given analysis.

Information is taken from different detector subsystems and the efficiencies are provided as a function of:

- Momenta. Correct identification of particle type depends on parameters such as the energy loss in the drift chamber and Čerenkov angle in the DIRC. These parameters in turn depend upon the momentum of the candidate in the laboratory frame.

- Angular distribution. Variation in the polar angle of the detector is important due to the geometry of the detector and variation in the degradation of the detector performance (eg radiation damage affects the forward end of the detector more than the backward end.)

- Running period. As the experiment progressed various parts of hardware degraded, or were replaced. This led to changes in the performance of various parts of the detector, leading to changes in efficiency.

- Matter-antimatter differences. Since the detector is made entirely of matter there may be significant different behaviors when comparing matter to antimatter.

The selection efficiency is therefore quoted separately for positively and negatively charged particles, run by run, as a function of laboratory frame momentum and polar angle. This analysis ignores variations in efficiency due to azimuthal angle.

Muon identification

Muon candidates are identified using a boosted decision tree output. Events of the type $e^+e^- \rightarrow \mu^+\mu^-\gamma$ are used to estimate the efficiency of the boosted decision tree output. The instrumented flux return was designed to issue a hardware `accept` command when two muon candidates were observed. This provides a very clean control sample for the muon particle identification study (where conservation of four-momentum provides unambiguous identification of muons) and allows the study of muon identification to be performed independently of the other particle species identificaton.

The efficiency of the output of the boosted decision tree is used to define different samples of muon candidates. This analysis uses the most efficient selection criterion, and the sample of candidates which pass this criterion is known as the `MuBDTVeryLoose` sample.

In spite of the success of the boosted decision tree based selection procedure, there remain a large number of pions which get misidentified as muons. In later times in the experiment it was noted that muon candidates with low momentum in the laboratory frame are more likely to be misidentified pions. A special boosted decision tree based selection procedure is used in this low momentum region and the sample of candidates which pass this criterion is known as the `MuBDTLoPLoose` sample.

The union of the `MuBDTVeryLoose` and `MuBDTLoPLoose` samples is used in this analysis. The efficiencies in Monte Carlo samples are then corrected by comparing Monte Carlo to data.

Figure 6.6 shows the raw number of events (in signal Monte Carlo) which pass the selection criteria, the yields of the particle selector, and the yields obtained using tables provided by the Particle Identification Working Group for the `MuBDTVeryLoose` and `MuBDTLoPLoose` selectors for positively charged muons during run 5 for the $D_s \to \mu\nu_\mu$ mode.

6.7.2 Multi-species particle selectors

To identify electron, charged pion, charged kaon, and proton candidates, BaBar uses a collection of particle identification selection procedures developed by the BaBar collaboration, which are referred to as multi-species particle selectors. The control samples used for each particle type are:

- $e^+e^- \to e^+e^-\gamma$, $\gamma \to e^+e^-e^+e^-$ for electron candidates.
- $D^{\star\pm} \to D^0\pi^\pm; D^0 \to K^\mp\pi^\pm$ for pion and kaon candidates (where the slow pion from the $D^{\star\pm}$ decay is used to resolve charge ambiguity).
- $\Lambda \to p\pi^\mp$ for proton candidates.

A series of bootstrap aggregated decision trees (multi-species particle trees) are trained using several variables obtained from the detector. Each multi-species particle tree is trained to identify a subset of particle species, returning a value between 0 and 1, where values close to 0 indicate a very low probability that candidates are correctly identified and values close to 1 indicate a very high probability that candidates are correctly identified. Since there are four particles species which can be identified using the multi-species particle trees there are sixteen possible multi-species particle trees, which are labelled using a vector of four bits. If a multi-species particle tree is trained to identify a particular particle species the corresponding bit is set to 1, otherwise it is set to 0. A multi-species particle tree with vector $[1, 1, 1, 1]$ does not provide any discrimination between particle species, and is excluded from the selection procedure. Pairs of multi-species particle selectors are complementary if their bits are related by inversion, and using both complementary multi-species particle trees does not increase discrimination between particles species. Excluding one tree from each

complementary pair, there are seven useful multi-species particle trees, outlined in table 6.3.

Table 6.3: Definition of multi-species particle trees. The columns labelled e, $\pi^{\pm}$, $K^{\pm}$, p indicate if a multi-species particle tree is trained to correctly identify the relevant particle species.

Multi-species particle tree	Bits	e	$\pi^{\pm}$	$K^{\pm}$	p
t_1	$[1,1,1,0]$	Yes	Yes	Yes	No
t_2	$[1,1,0,1]$	Yes	Yes	No	Yes
t_3	$[1,0,1,1]$	Yes	No	Yes	Yes
t_4	$[0,1,1,1]$	No	Yes	Yes	Yes
t_5	$[1,1,0,0]$	Yes	Yes	No	No
t_6	$[1,0,1,0]$	Yes	No	Yes	No
t_7	$[1,0,0,1]$	Yes	No	No	Yes

The most likely particle species hypothesis is found by finding the minimum sum of squares of the differences between the outputs from the multi-species particle trees and the values shown in table 6.4.

Table 6.4: Definitions of the sums of squares differences for the different particle species. X refers to the species of particle.

Particle species	Sum of squares of differences ($\sum_{i=1}^{7} \Delta_{Xi}^2$)
e	$\lvert(t_1,t_2,t_3,t_4,t_5,t_6,t_7)-(1,1,1,0,1,1,1)\rvert^2$
$\pi^{\pm}$	$\lvert(t_1,t_2,t_3,t_4,t_5,t_6,t_7)-(1,1,0,1,1,0,0)\rvert^2$
$K^{\pm}$	$\lvert(t_1,t_2,t_3,t_4,t_5,t_6,t_7)-(1,0,1,1,0,1,0)\rvert^2$
p	$\lvert(t_1,t_2,t_3,t_4,t_5,t_6,t_7)-(0,1,1,1,0,0,1)\rvert^2$

The selection criteria are manipulated to suit different analyses, with varying efficiencies and misidentifaction rates. The lists of candidates obtained from the selection criteria are arranged by efficiency and labelled `SuperLoose`, `VeryLoose`, `Loose`, `Tight`, and `VeryTight`, `SuperTight`.

6.7.3 Electron identification

In this analysis, the loosest multi-species particle selector for electrons, the `EKMSuperLoose` selector list, is used to define a sample of electron candidates. Figure 6.7 shows the

raw number of events (in signal Monte Carlo) which pass the selection criteria, the yields of the particle selector, and the yields obtained using tables provided by the Particle Identification Working Group for the `EKMSuperLoose` selector for electrons during run 5 for the $D_s \to e\nu_e$ mode. This figure compares positively and negatively charged electrons, indicating matter-antimatter effects.

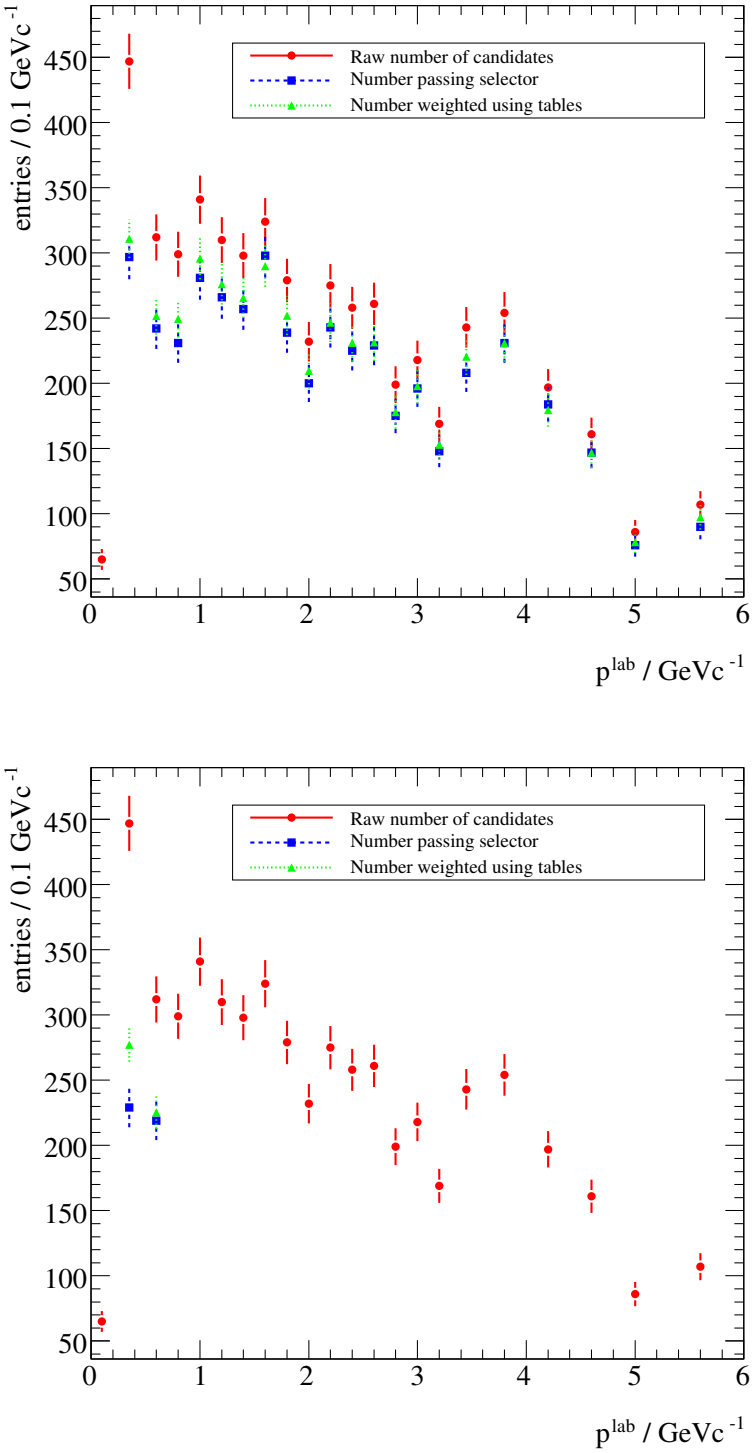

Figure 6.6: Particle identification yields for the muon selectors. The plot shows the raw number of Monte Carlo events passing the selection criteria (red circles), the number of events which also pass the muon selector (green squares), and the number of events weighted according to the information provided by the Particle Identification Working Group. This plot shows positively charged muons taken from Monte Carlo samples using the `MuBDTVeryLoose` selector (top) and the `MuBDTLoPLoose` selector (bottom) for run 5. Note that the `MuBDTLoPLoose` selector is used only on the very low momentum region. The uncertainties shown do not reflect the statistical uncertainty of the signal Monte Carlo samples used.

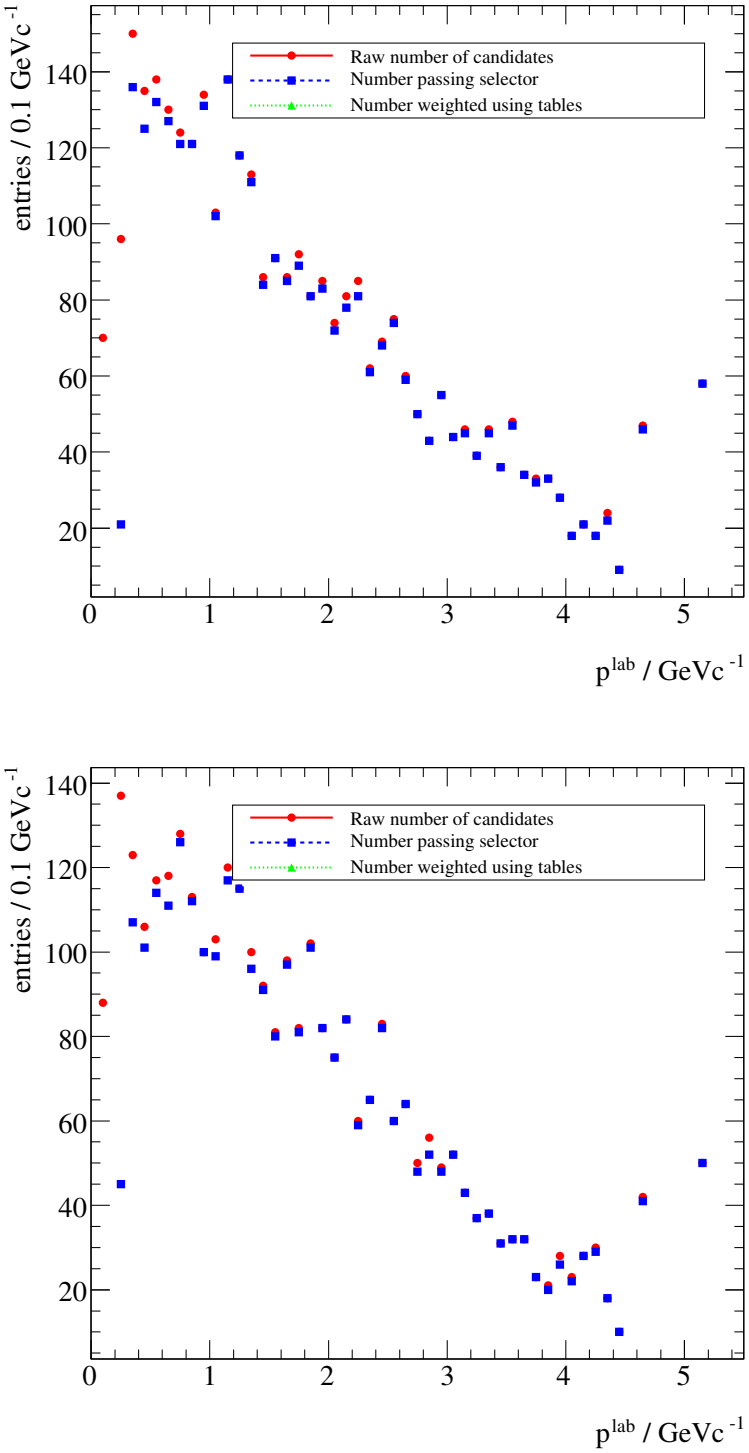

Figure 6.7: Particle identification yields for the `EKMSuperLoose` selector. The plot shows the raw number of Monte Carlo events passing the selection criteria (red circles), the number of events which also pass the `EKMSuperLoose` selector (green squares), and the number of events weighted according to the information provided by the Particle Identification Working Group. This plot shows positively electrons (top) and negatively charged electrons (bottom) taken from Monte Carlo samples for run 5. The uncertainties shown do not reflect the statistical uncertainty of the signal Monte Carlo samples used.

6.7.4 Other particle identification

A variety of selectors are used to identify other particle candidates in this analysis. However, the efficiencies of these selection criteria cancel out exactly, and the techniques used are very similar to those already described, hence the selections are not discussed in detail.

Other particle identification selection criteria include

- Charged track candidates, which are required to have a successfully reconstructed trajectory through the detector.
- Charged kaon candidates, where a boosted decision tree is used to identify candidates.

6.8 Composite particle reconstruction

Combining particle candidates from the samples defined by the particle identification selection criteria and photon candidates, along with vertex reconstruction algorithms it is possible to reconstruct commonly produced particle candidates, such as the π^0. Samples of such candidates are used in this analysis and include:

- $K^0_S \to \pi^+\pi^-$
- $\pi^0 \to \gamma\gamma$
- $\Lambda \to p\pi$

6.9 Summary

This chapter has outlined the methods developed at BaBar, which have been used in this analysis. The BaBar experiment has a wide range of useful analysis methods to make best use of the data available. The software environment is flexible enough to allow good simulation and reconstruction techniques, which inform analyses. The information from the BaBar detector provides excellent particle identification, and information from all subsystems is used in the reconstruction of physics events. Using this information it is possible to reconstruct entire events, extract yields and perform high precision measurements of important parameters.

Chapter 7

Reconstruction and selection method

7.1 Overview

This chapter outlines the reconstruction strategy for the measurements of the branching fractions $\mathcal{B}(D_s \to \ell\nu_\ell)$. The measurements are made by taking the ratio of branching fractions:

$$\mathcal{B}(D_s \to \ell\nu_\ell) = \frac{\mathcal{B}(e^+e^- \to D_s; D_s \to \ell\nu_\ell)}{\mathcal{B}(e^+e^- \to D_s)} \tag{7.1}$$

where any other particles consistent with known conservation laws are allowed in the final state. The first part of the chapter outlines the reconstruction of the D_s candidates, sometimes referred to as the 'denominator' part of the analysis. Given the limitations of the Monte Carlo simulation the measurements of the branching fractions are corrected for the true hadronisation processes and care is taken to model these effects correctly. The final part of the chapter outlines the reconstruction of the final states, sometimes referred as the 'numerator' part of the analysis.

7.2 Event topology

An event candidate is reconstructed in the following manner:

- A charm tag candidate (C_{tag}) is reconstructed.
  - If the tag is baryonic a proton candidate (p_{tag}) is also reconstructed.

- A strange tag meson candidate (K_{tag}) is reconstructed.
- Additional pion candidates are reconstructed assuming that they originate from hadronisation processes close to the interaction point. The system consisting of particle candidates arising from the hadronisation processes are labelled X.
- A photon candidate, γ, is identified.
- A charged lepton candidate, ℓ, is identified.
- The net missing four-momentum in the centre of mass frame is used to identify a neutrino system candidate.

The event topology is shown in figure 7.1

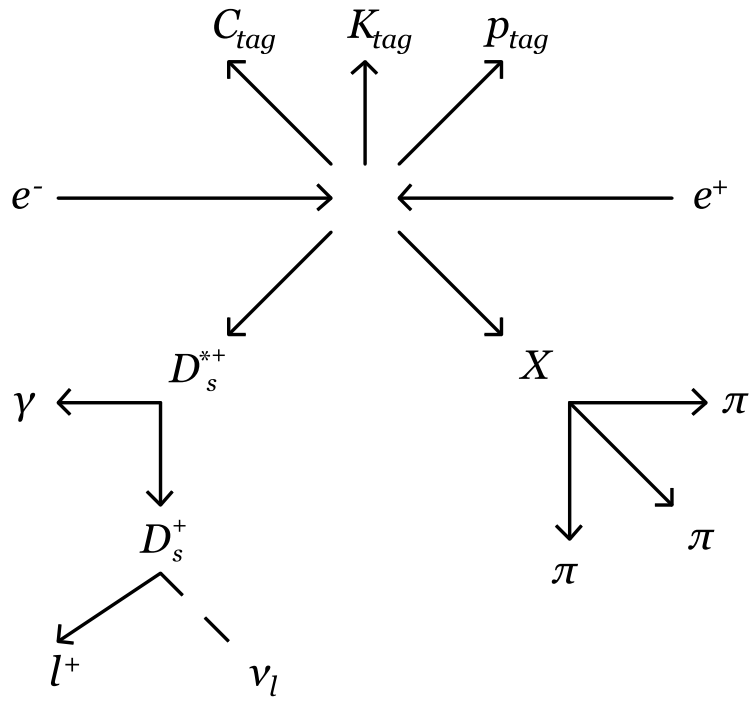

Figure 7.1: Event topology, showing a reconstruction with a baryonic charm tag candidate.

7.3 Charm tag reconstruction

An exhaustive list of charm tag candidates is given in table 7.1. Every tag candidate listed gives unambiguous determination of the flavour of the charm quark in the candidate. Therefore, informed by the discussion in section 2.7.1, decays of the D^0 meson to a K^0_S are not included in the list, unless the flavour of the D^0 meson can

be determined via the decay $D^{\star+} \to D^0\pi^+$. Charm tag reconstruction was optimised by varying selection criteria on a subset of the data (1/4 of Run 3 OnPeak running) to obtain the best significance, θ,

$$\theta = \frac{N_S}{\sqrt{N_S + N_B}} \tag{7.2}$$

where N_S is the number of correctly reconstructed charm tags and N_B is the number of background events (including misreconstructed events). The mass distribution of correctly reconstructed charm tags was modelled using a Gaussian probability density function. The distribution of other events was modelled using a linear probability density function. Figure 7.2 shows the mass specrum of $D^0 \to K^-\pi^+$ charm tag candidates for data.

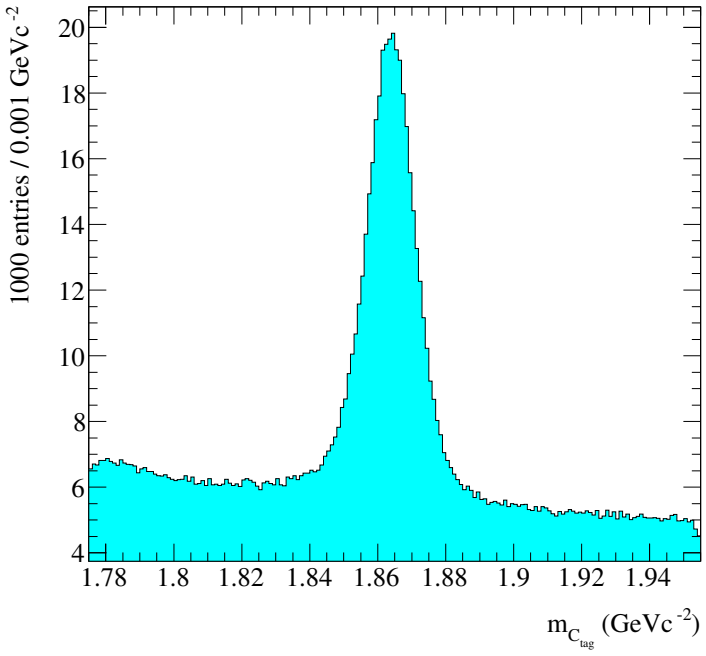

Figure 7.2: Mass spectrum of $D^0 \to K^-\pi^+$ candidates for data.

A kinematic fit was performed for each charm tag candidate. The following variables were used in the optimisation study:

- Particle identification selection criteria.
- The photon energy for π^0 daughter candidates.
- The invariant mass of the reconstructed charm tag candidate.

- The momentum of the reconstructed charm tag candidate in the centre of mass frame.
- The probability of the χ^2 of the kinematic fit given the number of degrees of freedom.

It should be noted that the efficiency of these selection criteria are not calculated explicitly, as such a study would rely on samples of Monte Carlo simulated events. The Monte Carlo simulation does not model the production of hadrons well, so an efficiency study would not return meaningful results.

Following the charm tag candidate reconstruction, $D^\star$ candidates are reconstructed. The purpose of this reconstruction is to improve the resolution of the invariant mass of the missing four-momentum in the event reconstruction, so no candidates are rejected in this process. The $D^\star$ candidate selection was chosen using 1/3 of Run 3 OnPeak running. The difference in the masses of the D and $D^\star$ candidates is Δm. Where a π^0 was used in the reconstruction the invariant mass of the two photon candidate system is $m_{\gamma\gamma}$, the energy of the two photon candidate system in the laboratory frame is $E_{\gamma\gamma}$, and the energy of such a daughter in the laboratory frame is E_γ. The purity of the sample is defined as the ratio of the estimate of the number of correctly reconstructed candidates to the total number of reconstructions. The selection criteria outlined in table 7.2 are applied, with the requirement that the purity of the $D^\star$ sample was not lower than the purity of the D sample. A typical $D^\star$ mass peak is shown in figure 7.3.

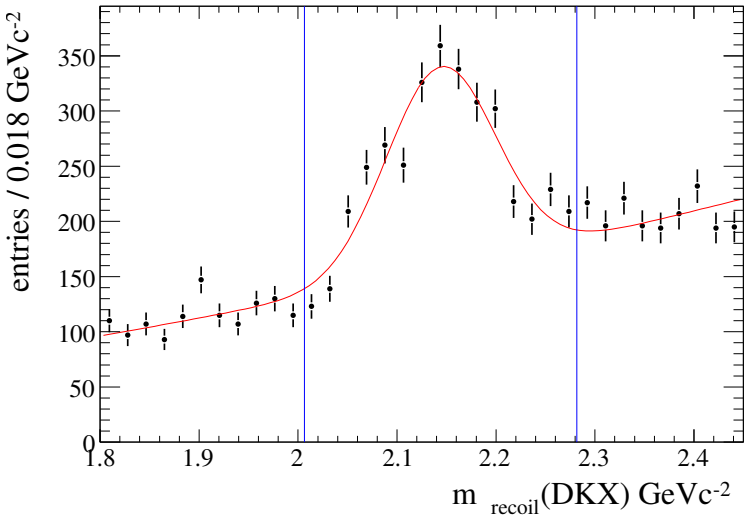

Figure 7.3: The $D^\star$ charm tag candidate mass spectrum for Monte Carlo reconstructions. This plot shows reconstruction with one π^0 in the hadronisation system.

Table 7.1: Summary of charm tags. (Jackson 2010)

Charm tag mode	Quark content	Charge (e)	Branching fraction of parent
$D^0 \to K^-\pi^+$	$c\bar{u}$	0	$3.89 \pm 0.05\%$
$D^0 \to K^-\pi^+\pi^0$	$c\bar{u}$	0	$13.9 \pm 0.5\%$
$D^0 \to K^0_S\pi^+\pi^-$	$c\bar{u}$	0	$2.99 \pm 0.17\%$
$D^0 \to K^-\pi^+\pi^+\pi^-$	$c\bar{u}$	0	$8.10 \pm 0.20\%$
$D^0 \to K^0_S\pi^+\pi^-\pi^0$	$c\bar{u}$	0	$5.4 \pm 0.6\%$
$D^0 \to K^-\pi^+\pi^+\pi^-\pi^0$	$c\bar{u}$	0	$4.2 \pm 0.4\%$
$D^+ \to K^0_S\pi^+$	$c\bar{d}$	1	$1.45 \pm 0.04\%$
$D^+ \to K^-\pi^+\pi^+$	$c\bar{d}$	1	$9.22 \pm 0.21\%$
$D^+ \to K^0_S\pi^+\pi^0$	$c\bar{d}$	1	$6.8 \pm 0.5\%$
$D^+ \to K^-\pi^+\pi^+\pi^0$	$c\bar{d}$	1	$6.00 \pm 0.20\%$
$D^+ \to K^0_S\pi^+\pi^+\pi^-$	$c\bar{d}$	1	$3.02 \pm 0.12\%$
$\Lambda_c^+ \to pK^0_S$	udc	1	$1.15 \pm 0.3\%$
$\Lambda_c^+ \to pK^-\pi^+$	udc	1	$5.0 \pm 1.3\%$
$\Lambda_c^+ \to pK^0_S\pi^+\pi^-$	udc	1	$1.3 \pm 0.35\%$
$\Lambda_c^+ \to pK^-\pi^+\pi^0$	udc	1	$3.4 \pm 1.0\%$
$\Lambda_c^+ \to \Lambda\pi^+$	udc	1	$1.07 \pm 0.28\%$
$\Lambda_c^+ \to \Lambda\pi^+\pi^0$	udc	1	$3.6 \pm 1.3\%$
$\Lambda_c^+ \to \Lambda\pi^+\pi^+\pi^-$	udc	1	$2.6 \pm 0.7\%$
$\Lambda_c^+ \to \Sigma^0\pi^+$	udc	1	$1.05 \pm 0.28\%$
$\Lambda_c^+ \to \Sigma^0\pi^+\pi^+\pi^-$	udc	1	$0.83 \pm 0.31\%$

Table 7.2: Selection criteria of excited charm tags. (Benitez 2010)

Charm tag mode	Δm ($\mathrm{GeVc^{-2}}$)	E_γ (MeV)	$E_{\gamma\gamma}$ (MeV)	$m_{\gamma\gamma}$ ($\mathrm{MeVc^{-2}}$)
$D^{\star+} \to D^0\pi^+$	$143.92 - 146.92$			
$D^{\star0} \to D^0\pi^0$	$139.12 - 145.12$	> 30	> 200	$115 - 150$
$D^{\star+} \to D^+\pi^0$	$137.64 - 143.62$	> 30	> 200	$115 - 150$
$D^{\star0} \to D^0\gamma$	$139.12 - 145.12$	> 250		

7.3.1 Rejection of $b\bar{b}$ events

Relatively large numbers of pairs of $b\bar{b}$ quarks were produced at the interaction region. (In fact, PEP-II is often referred to as a 'B Factory'.) B mesons decay predominantly to charm mesons and other particles, so $e^+e^- \rightarrow b\bar{b}$ events contribute significant backgrounds to the reconstruction method. (In particular, real charm mesons can be reconstructed from the decay products of real B mesons.) Placing restrictions on the tagging systems can remove most of these backgrounds.

When a $b\bar{b}$ pair is produced the system will hadronise to form B mesons (either B^+B^- or $B^0\bar{B}^0$) and conservation of energy and momentum constrains the momenta of these mesons in the centre of mass frame to be $330\,\mathrm{MeVc}^{-1}$. An upper limit can be placed on the momentum of a charm meson from the decay $B \rightarrow DX$ in this frame (where B is a meson with quark content $b(\bar{u}/\bar{d})$ and D is any charm meson.) The charm meson will have the maximum momentum in the B rest frame when the recoiling system, X, is massless. In this limit the momentum of the D meson is found to be (for $B^0 \rightarrow D^0X$) $2310\,\mathrm{MeVc}^{-1}$. In the centre of mass frame this momentum can be no larger than $2898\,\mathrm{MeVc}^{-1}$. In principle, requiring tag candidates to have a momentum that exceeds $2898\,\mathrm{MeVc}^{-1}$ in the centre of mass frame would eliminate all correctly reconstructed real charm mesons from $b\bar{b}$ events. (A similar argument can be applied to charm baryons for the case of Λ_c^+ tags.)

Figure 7.4 shows the momentum of charm tag candidates in the centre of mass frame for generic Monte Carlo, for samples where B and charmed mesons are produced. Figure 7.5 shows the mass spectra of charm tag candidates in the centre of mass frame for generic Monte Carlo, for samples where B mesons and samples where charmed mesons are produced when different requirements are made of the momentum of the charm tag candidate in the centre of mass frame. Figure 7.6 shows the same spectra for running at energies higher and lower than the energy of the $\Upsilon(4S)$, showing evidence of the peaking background from the B mesons.

7.3.2 Suppression of $u\bar{u}$, $d\bar{d}$, $s\bar{s}$, $\tau^+\tau^-$ events

Events of the type $e^+e^- \rightarrow q\bar{q}$ (where $q = u/d/s$ and where no heavier quarks are present) were produced in large numbers at the interaction region. Since these particles are not heavy enough to decay to real charm mesons or baryons any tag candidates identified in such events must be incorrectly reconstructed. While there are a small number of events which can be misreconstructed in such a way, the invariant

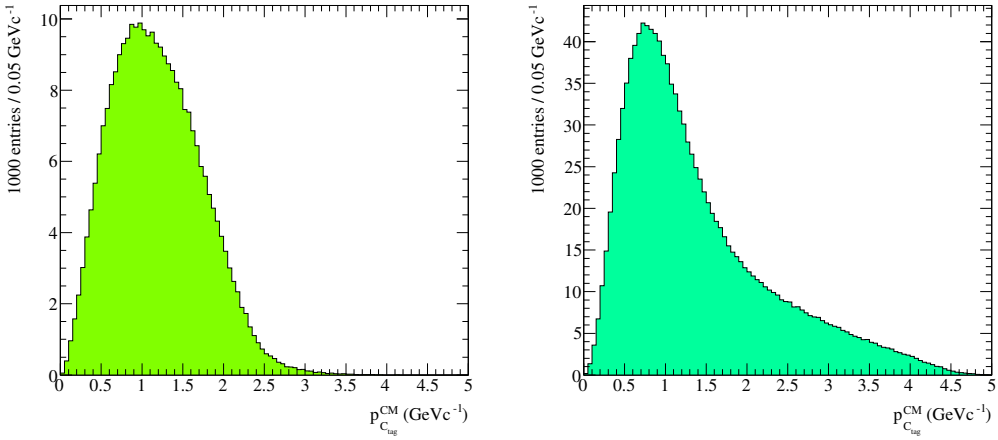

Figure 7.4: Momentum spectra of charm tag candidates in the centre of mass frame for $b\bar{b}$ (left) and $c\bar{c}$ (right) generic Monte Carlo. This plot shows the momentum spectra for $D^0 \to K^-\pi^+$ candidates from run 3.

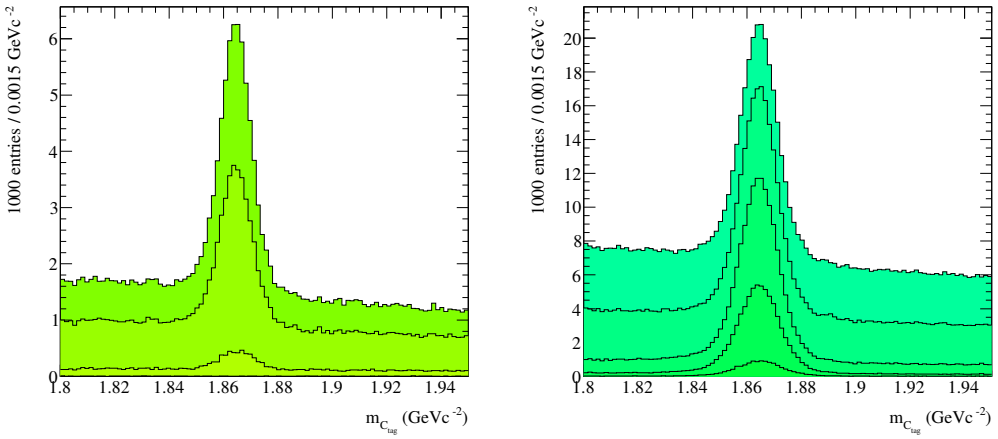

Figure 7.5: Mass spectra of charm tag candidates for $b\bar{b}$ (left) and $c\bar{c}$ (right) generic Monte Carlo. This plot shows the mass spectra for $D^0 \to K^-\pi^+$ candidates from run 3. The darkest histograms show the spectra where there is no requirement made on the centre of mass frame charm tag candidate momentum. The lighter histograms show the mass spectra for requirements that the centre of mass frame charm tag candidate momentum be greater than $1\,\mathrm{GeVc}^{-1}$, $2\,\mathrm{GeVc}^{-1}$, $3\,\mathrm{GeVc}^{-1}$, and $4\,\mathrm{GeVc}^{-1}$.

mass spectra of these events are smooth and do not contain any significant peaks. Similarly events of the type $\tau^+\tau^-$ cannot decay to form real charm mesons. Events of the type $e^+e^- \to u\bar{u}, d\bar{d}, s\bar{s}, \tau^+\tau^-$ are referred to as continuum and their invariant mass spectra can be well modeled. Figure 7.7 shows the momentum and mass spectra for continuum Monte Carlo.

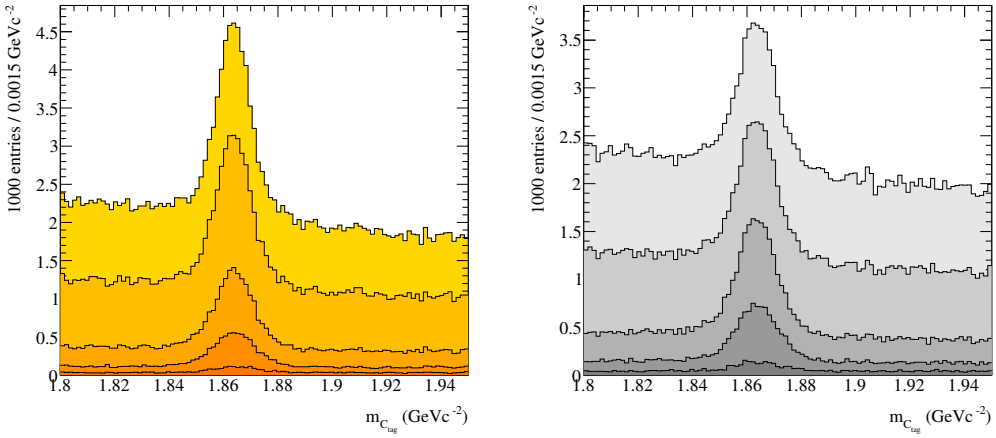

Figure 7.6: Mass spectra of charm tag candidates for data taken at energies higher than (left) and lower than (right) the energy of the $\Upsilon(4S)$ meson. This plot shows the mass spectra for $D^0 \to K^-\pi^+$ candidates from run 3. The darkest histograms show the spectra where there is no requirement made on the centre of mass frame charm tag candidate momentum. The lighter histograms show the mass spectra for requirements that the centre of mass frame charm tag candidate momentum be greater than $1\,\mathrm{GeVc}^{-1}$, $2\,\mathrm{GeVc}^{-1}$, $3\,\mathrm{GeVc}^{-1}$, and $4\,\mathrm{GeVc}^{-1}$.

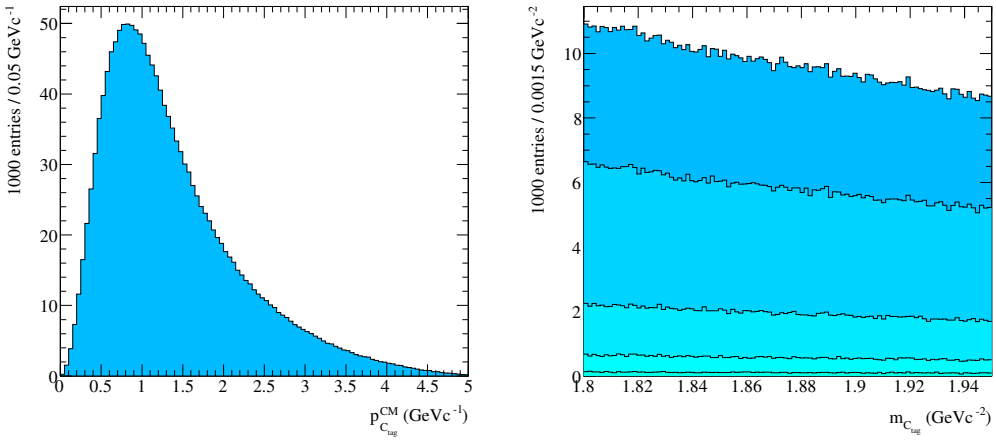

Figure 7.7: Momentum (left) and mass (right) spectra of charm tag candidates in the centre of mass frame for continuum generic Monte Carlo. These plots shows the momentum and mass spectra for $D^0 \to K^-\pi^+$ candidates from run 3.

7.4 Kaon and proton reconstruction

Kaon candidates are identified using the following criteria:

- Charged kaons
  - Candidates must pass the loosest boosted decision tree kaon candiate identification criteria.

- Neutral kaons
  - Two oppositely charged pion candidates are taken from the loosest charged track candidate sample.
  - A mass constrained kinematic fit is performed using the `TreeFitter` algorithm and the probability of a successful fit must be greater than 0.1%.
  - The cosine of the angle between the line of flight of the K^0_S candidate from the interaction region and the momentum of the K^0_S candidate in the laboratory frame must be positive.

Where the charm tag candidate is baryonic, a proton candidate is identified using the loosest multi-species particle proton selection criteria.

7.5 Hadronisation reconstruction

When pairs of charm quarks were produced at BaBar there was enough energy to create additional hadrons via quantum chromodynamical processes. These hadronisation processes are not well modelled in Monte Carlo. In particular the Monte Carlo collections do not model the number of hadrons produced, or their momenta spectra well. In order to determine the efficiency of the selection criteria this hadronisaton process needs to be well understood. Figure 7.8 shows the Feynman diagram for the hadronisation process for a typical event. The X system can undergo further quark-antiquark production.

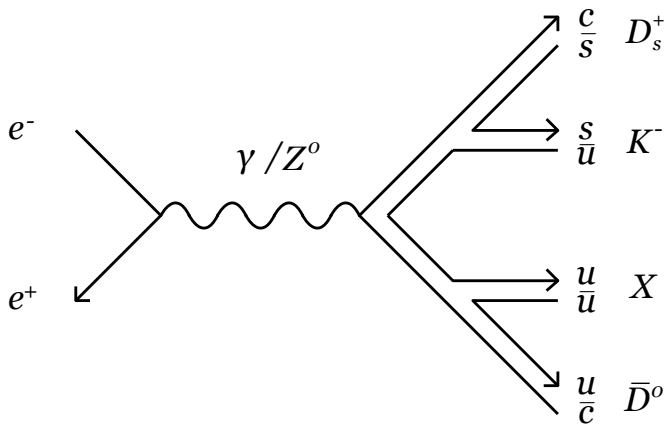

Figure 7.8: Event hadronisation, showing the production of charmed and strange quarks, as well as the X system.

An X system is formed by combining charged and neutral hadrons. Studies show that the contribution from KK pairs is negligible, so only pions are considered. The number of reconstructed paticles in the X system is called n_X^R and the true number of pions created by the hadronisation process is called n_X^T. Performing efficiency studies using the Monte Carlo collections it is possible to determine the n_X^T distribution as a function of the n_X^R distribution.

Candidates with more than three charged pion candidates or more than one π^0 candidate are found to have very large backgrounds and low efficiencies and are excluded from the analysis. The following X system candidates are reconstructed:

- No pions
- π^+
- $\pi^+\pi^-$
- $\pi^+\pi^-\pi^+$
- π^0
- $\pi^+\pi^0$
- $\pi^+\pi^-\pi^0$

The following selection criteria are applied to the pion candidates:

- π^+ candidates
  - The momentum in the laboratory frame must be larger than $100\,\mathrm{MeVc}^{-1}$.
- π^0 candidates
  - $121.3 < m_{\gamma\gamma} < 145.3\,\mathrm{MeVc}^{-2}$
  - $E_\gamma > 100\,\mathrm{MeV}$ if $\cos\theta < 0.5$
  - $E_\gamma > 100 + 100(\cos\theta - 0.5)\,\mathrm{MeV}$ if $\cos\theta \geq 0.5$

where the variables have the same meanings as in section 7.3 and θ is the polar angle of the photon candidate momentum with respect to the beam axis.

The determination of the n_X^T distribution is not performed at this point.

7.6 Tagging system

The tagging system consists of the C_{tag}, K_{tag}, X, and (if necessary) p_{tag}. All possible combinations of tagging systems are considered. If there are n candidates per event then each candidate is weighted by a factor of $1/n$ to ensure that events are not multiply counted.

Table 7.3: Tagging systems.

C	K_{tag}	p_{tag}	X	Right sign/wrong sign sample
D^0	K^+		X^0	Right sign
D^0	K^0_S		X^+	Right sign
D^+	K^+		X^-	Right sign
D^+	K^0_S		X^0	Right sign
Λ_c^+	K^+	$\bar{p}$	X^0	Right sign
Λ_c^+	K^0_S	$\bar{p}$	X^+	Right sign
D^0	K^+		X^{--}	Wrong sign
D^0	K^0_S		X^-	Wrong sign
D^+	K^0_S		X^{--}	Wrong sign
Λ_c^+	K^+	$\bar{p}$	X^{--}	Wrong sign
Λ_c^+	K^0_S	$\bar{p}$	X^-	Wrong sign

7.6.1 Right sign and wrong sign definitions

The tagging systems are divided into three samples. The right sign sample contains all the reconstructions where the quark flavour and charge of the tagging system is consistent with the recoiling against a system with quark content $c\bar{s}$. The wrong sign sample contains all the reconstructions where the quark flavour of the tagging system is consistent with the recoiling against a system with quark content $c\bar{s}$, but the charge is of the wrong sign. A third sample contains all other events, and is not used in this analysis. An exhaustive list of right sign and wrong sign tagging systems is given in table 7.3.

A signal region is defined using studies from Monte Carlo simulation. Events which do not fall into this signal region are said to be in the sidebands. By fitting to the invariant missing mass squared it is possible to form two sidebands. This allows a more stringent comparison of Monte Carlo simulated events and real data events.

7.7 Signal reconstruction

In order to reconstruct a signal candidate a series of kinematic fits is performed. In each fit the invariant mass recoiling against a system of particles is used to determine the yield.

7.7.1 $D_s^\star$ reconstruction

A $D_s^\star$ candidate is reconstructed using a kinematic fit with the tagging system recoiling against the missing four-momentum, defined as

$$p_{miss}^{D_s^\star} = p_{e^+e^-} - p_C - p_{K_{tag}} - p_{p_{tag}} - p_X \tag{7.3}$$

where $p_{e^+e^-}$ is the momentum of the electron-positron system, p_C is the momentum of the charm tag candidate, $p_{K_{tag}}$ is the momentum of the tag kaon candidate, $p_{p_{tag}}$ is the momentum of the tag proton candidate (if it exists in the reconstruction), and p_X is the momentum of the X system. For events containing a real $D_s^\star$ the resulting distribution will peak around the $D_s^\star$ mass. A mass window is placed on the recoiling mass distribution around the nominal $D_s^\star$ mass and events which fall outside the mass window are rejected. Hence the system $[C, (K_{tag}), (p_{tag}), (X)]$ is referred to as the $D_s^\star$ recoil system. Figure 7.9 shows the topology of the $D_s^\star$ recoiling against the $D_s^\star$ recoil system. Figure 7.10 shows the mass spectrum of the $D_s^\star$ candidate for generic $c\bar{c}$ events.

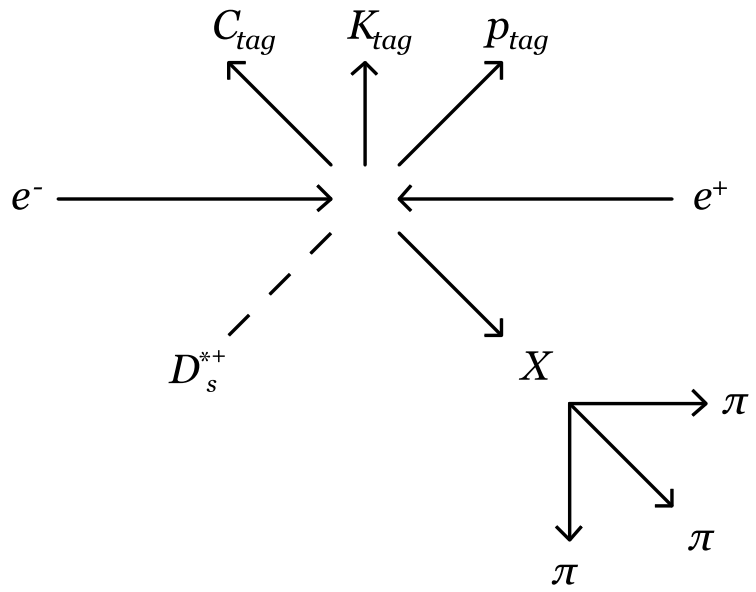

Figure 7.9: Event topology, showing a $D_s^\star$ candidate and $D_s^\star$ recoil system.

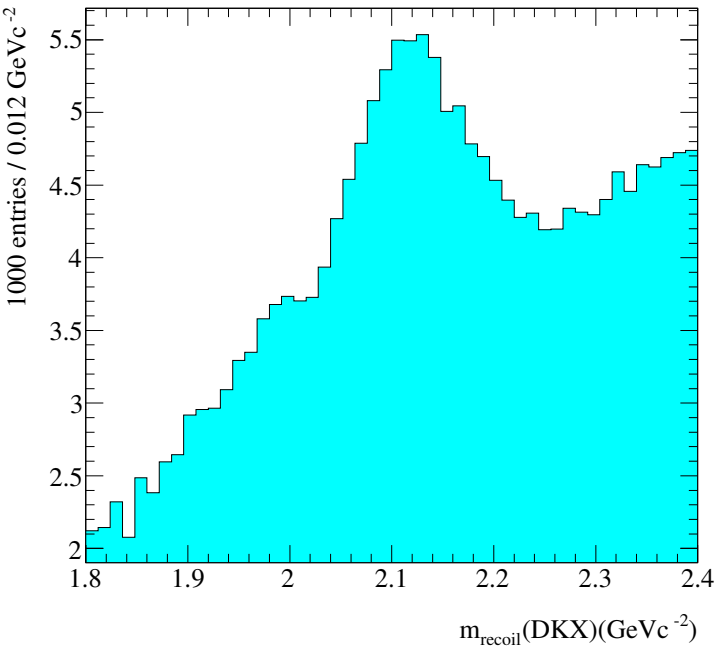

Figure 7.10: Mass spectrum of $D_s^\star$ candidates for generic $c\bar{c}$ Monte Carlo.

7.7.2 D_s reconstruction

A photon candidate is identified which is consistent with the decay $D_s^\star \to D_s\gamma$ and does not overlap with the $D_s^\star$ recoil system. The photon candidate must satisfy the following criteria:

- $E_\gamma > 120\,\text{MeV}$
- The cosine of the angle between the direction of charm tag candidate and the direction of the photon candidate is negative.

where E_γ is the energy of the photon candidate in the laboratory frame. Figure 7.11 shows the cosine of the angle between correctly reconstructed charm tag candidates and correctly identified photons, using truth-matched Monte Carlo samples.

There are significant contributions to the sample of photon candidates from the processes $\pi^0 \to \gamma\gamma$ and $\eta \to \gamma\gamma$. A veto is applied to reconstructions where the photon candidate is likely to originate from these processes. Pairs of photons are taken and used to reconstruct π^0 and η candidates. The `TreeFitter` algorithm is used to perform a kinematic fit. The meson candidate is mass-constrained and required to originate from the interaction point. If the resulting probability of a successful fit

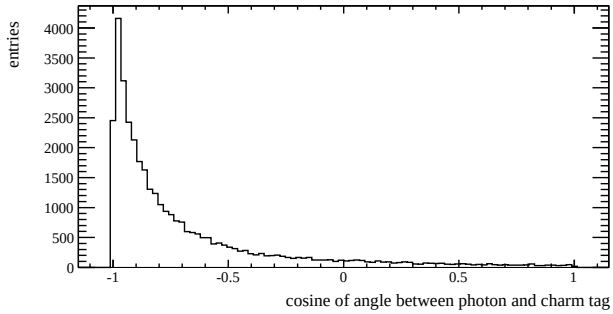

Figure 7.11: Cosine of the angle between the charm tag and photon for Monte Carlo, where the charm tag and photon have both been correctly identified and reconstructed. (Benitez 2010)

satisfies $P(\chi^2|n) > 1\%$ the veto is applied and the photon candidate is rejected.

A kinematic fit is performed with the tagging system and photon recoiling against the missing four-momentum, now defined as

$$p_{miss}^{D_s} = p_{e^+e^-} - p_C - p_{K_{tag}} - p_{p_{tag}} - p_X - p_\gamma \tag{7.4}$$

For events containing a real D_s this will peak around the D_s mass. Another mass window is placed on the recoiling mass distribution around the nominal D_s mass and events which fall outside the mass window are rejected. Hence the system $[C, (K_{tag}), (p_{tag}), (X), \gamma]$ is referred to as the D_s recoil system. Figure 7.12 shows the topology of the D_s recoiling against the D_s recoil system. Figure 7.13 shows the mass spectrum of the D_s candidate for generic $c\bar{c}$ events.

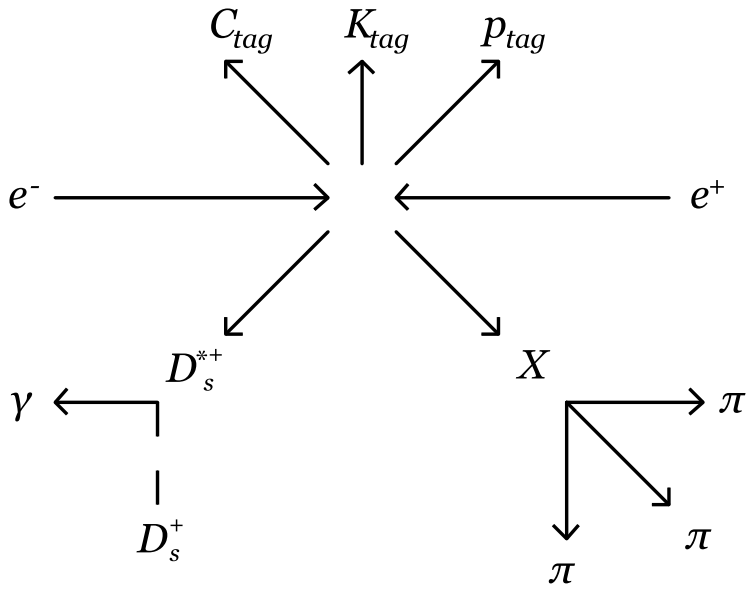

Figure 7.12: Event topology, showing a D_s candidate and D_s recoil system.

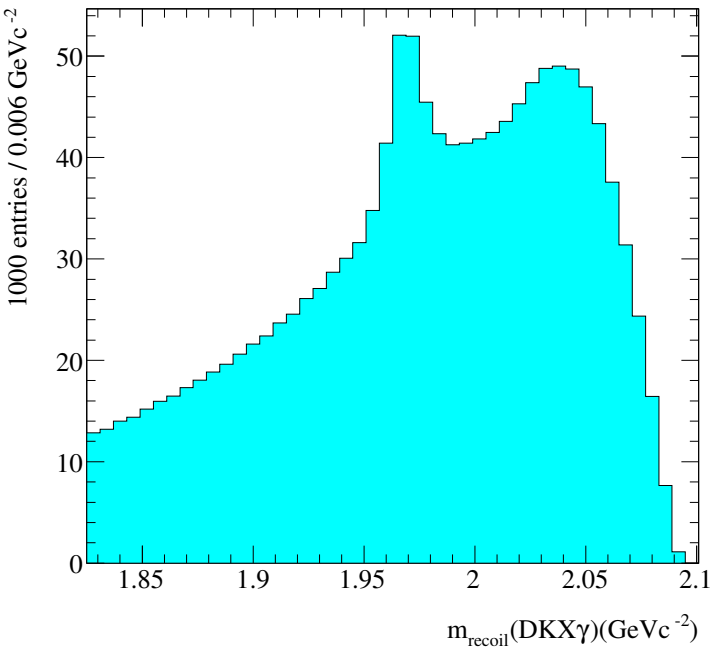

Figure 7.13: Mass spectrum of D_s candidates for generic $c\bar{c}$ Monte Carlo.

7.7.3 Leptonic system reconstruction

Four final states are investigated:

- $D_s \to e\nu_e$
- $D_s \to \mu\nu_\mu$
- $D_s \to \tau\nu_\tau; \tau \to e\nu_e\nu_\tau$
- $D_s \to \tau\nu_\tau; \tau \to \mu\nu_\mu\nu_\tau$

For each final state a charged lepton candidate is identified by taking a candidate from the list of charged track candidates. If there are any other track candidates left in this list after the charged lepton has been identified the reconstruction is rejected. Electron candidates are required to pass the `EKMSuperLoose` selection criteria and muon candidates are required to pass either `MuBDTVeryLoose` or `MuBDTLoPLoose` selection criteria.

A kinematic fit is performed with the tagging system and photon recoiling against the missing four-momentum, now defined as

$$p_{miss}^{D_s} = p_{e^+e^-} - p_C - p_{K_{tag}} - p_{p_{tag}} - p_X - p_\gamma - p_\ell \tag{7.5}$$

where p_ℓ is the momentum of the charged lepton candidate. For reconstructions of the type $D_s \to e\nu_e$ and $D_s \to \mu\nu_\mu$ this mass squared should form a sharp peak at zero $\mathrm{GeV^2c^{-4}}$. For these reconstructions, the D_s candidate is mass constrained in the final kinematic fit to improve the resolution of this peak. For reconstructions of the type $D_s \to \tau\nu_\tau; \tau \to e\nu_e\nu_\tau$ and $D_s \to \tau\nu_\tau; \tau \to \mu\nu_\mu\nu_\tau$ there is no sharp peak as there are three neutrinos in the final state. Therefore the mass constraint is not applied to the D_s candidate for these reconstructions.

The signal events are modeled using Monte Carlo samples. The background events are modeled using generic Monte Carlo samples. Where the branching fractions of the D_s meson in the Monte Carlo simulation disagrees with the world average quoted in the Particle Data Group the events in the simulation are weighted by the ratio of the world average branching fraction in the Particle Data Group and branching fraction in the Monte Carlo simulation. This correction is only applied if the disagreement is larger than the uncertainty on the branching fraction provided by the Particle Data Group. The semileptonic decays of the D_s are not well modeled in the Monte Carlo simulation and contribute a high proportion of the background events. The

semileptonic decays of the D_s mesons are modeled using a dedicated probability density function taken from Monte Carlo samples.

The event topology for the $D_s \to e\nu_e$ and $D_s \to \mu\nu_\mu$ modes is shown in figure 7.14, and for the $D_s \to \tau\nu_\tau; \tau \to e\nu_e\nu_\tau$ and $D_s \to \tau\nu_\tau; \tau \to \mu\nu_\mu\nu_\tau$ modes in figure 7.15.

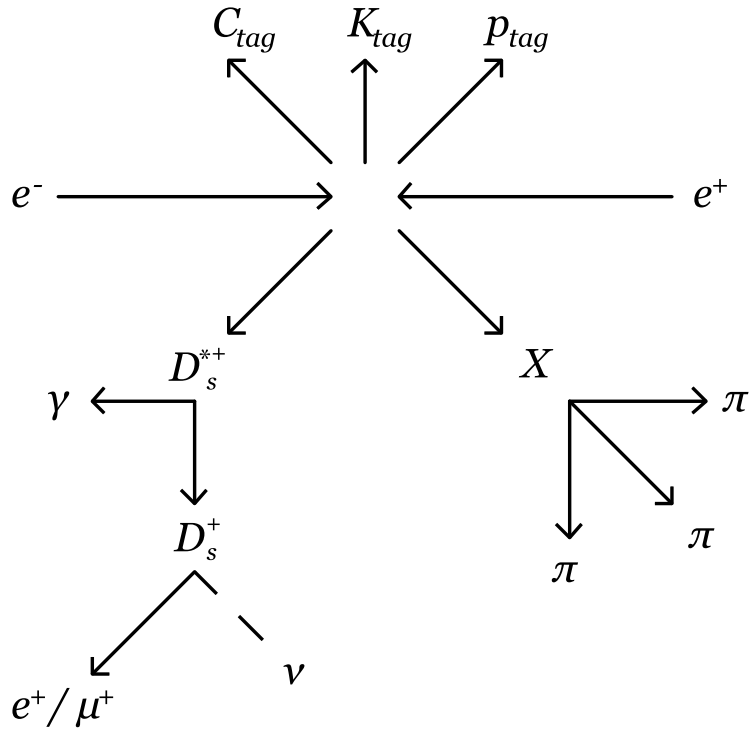

Figure 7.14: Event topology, showing a ν candidate and ν recoil system for the $D_s \to e\nu_e$ and $D_s \to \mu\nu_\mu$ mode.

7.8 Summary

The reconstruction of complete events is a multi-stage process, including a sophisticated tagging system. By reconstructing the whole event an inclusive sample of D_s candidates can be identified. This allows the absolute measurement of the branching fractions $\mathcal{B}(D_s \to \ell\nu_\ell)$.

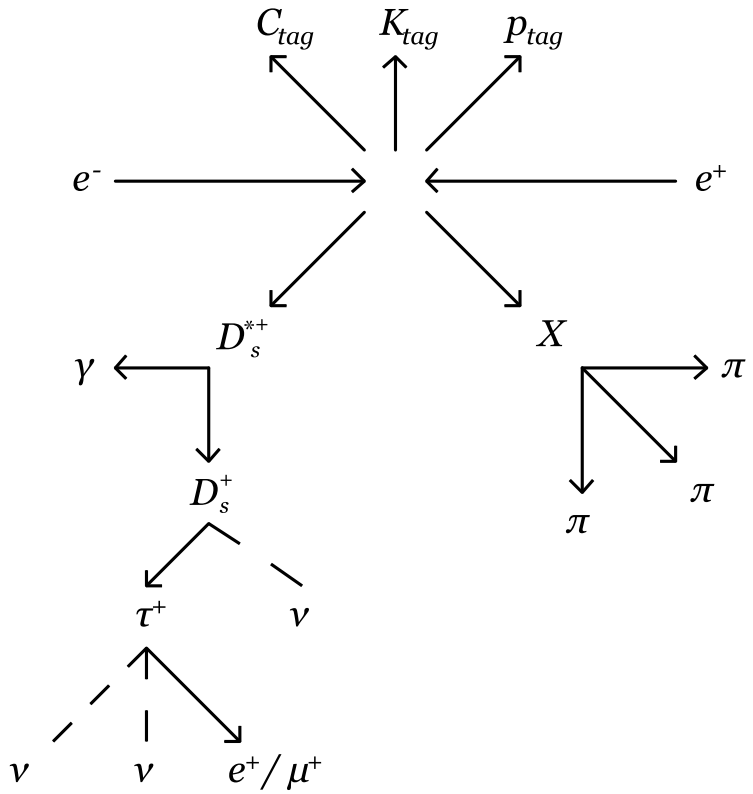

Figure 7.15: Event topology, showing a ν system candidate and ν recoil system for the $D_s \to \tau\nu_\tau; \tau \to e\nu_e\nu_\tau$ and $D_s \to \tau\nu_\tau; \tau \to \mu\nu_\mu\nu_\tau$ mode.

Chapter 8

Inclusive D_s and $D_s \to \ell\nu_\ell$ yield extraction

8.1 Overview

Once the reconstruction of events has been performed it is possible to determine the branching fractions. This is achieved in two stages. First the number of D_s mesons in the data is determined using a fit to the mass spectrum of the D_s candidates and the reconstructed number of pions in the event, n_X^R. This fit determines the n_X^T spectrum in data, which is used to reweight the efficiencies of event reconstruction. The yields of numerator events ($D_s \to \ell\nu_\ell$) are then extracted and the branching fractions are estimated using the efficiency corrected ratio of the yields of the $D_s \to \ell\nu_\ell$ events and D_s events.

8.2 Inclusive D_s yield estimate

In order to measure the absolute branching fractions the yield of D_s mesons in data must be estimated. Due to the differences in the hadronisation processes between the Monte Carlo and data samples this is not trivial.

8.2.1 X system crossfeed

Studies using Monte Carlo samples show that the n_X^T distribution does not map simply onto the n_X^R distribution, and the efficiency of the selection criteria is a function of the n_X^T distribution. Without determining the n_X^T distribution in data it is impossible

to estimate the yield of D_s mesons in data. Figure 8.1 shows the n_X^R distributions for each value of n_X^T in Monte Carlo reconstructions. The n_X^T distribution in data is determined using a two dimensional yield extraction fit to the mass of the D_s candidate and the n_X^R distribution. This fit is also performed to estimate the D_s yield in data. In principle the spectrum of n_X^T extends to very large values. However, due to the finite size of the samples all reconstructions with $n_X^T \geq 6$ are combined into a single sample.

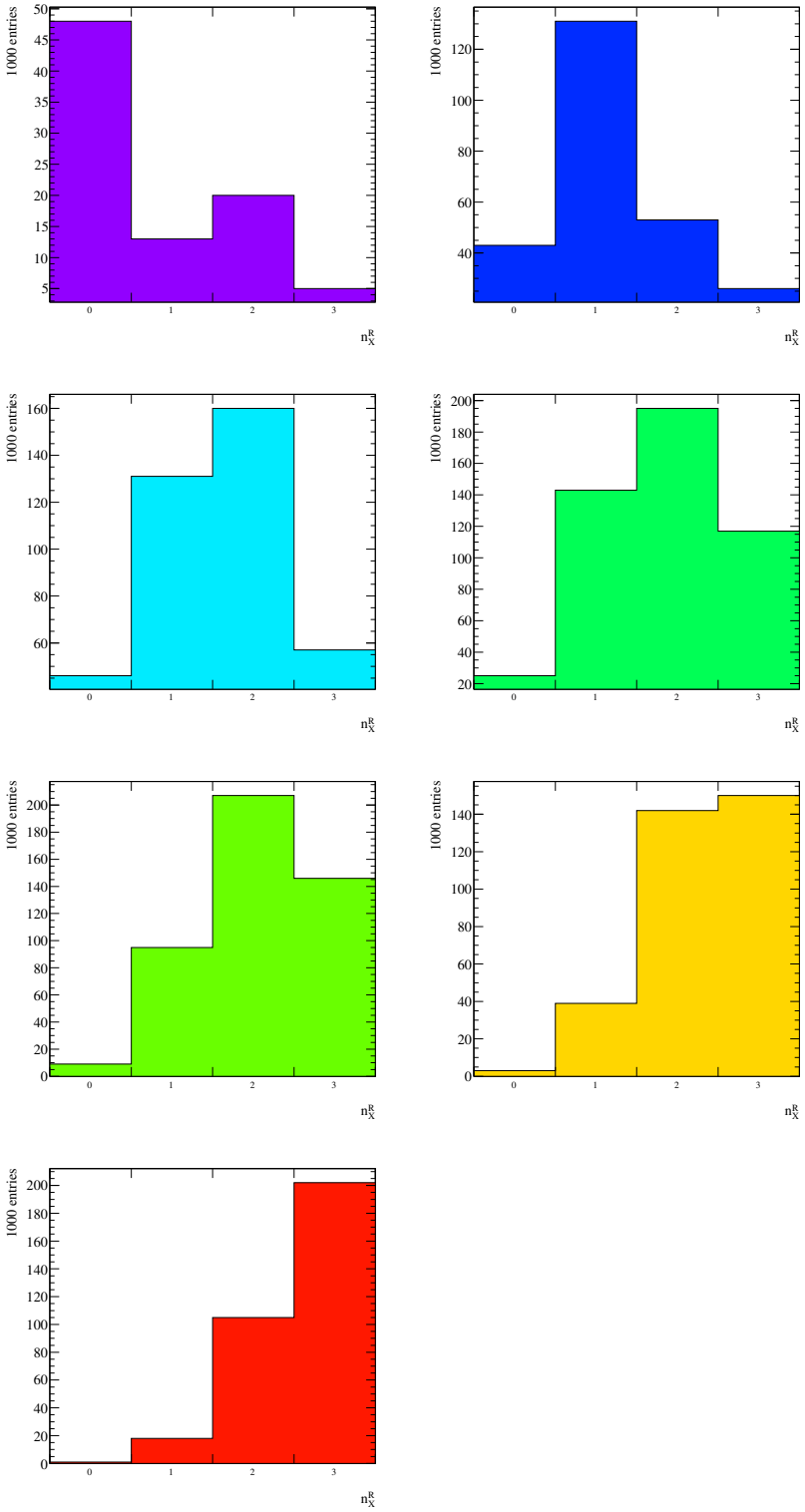

Figure 8.1: The distribution of n_X^R for $n_X^T = 0$ (first row left), $n_X^T = 1$ (first row right), $n_X^T = 2$ (second row left), $n_X^T = 3$ (second row right), $n_X^T = 4$ (third row left), $n_X^T = 5$ (third row right), and $n_X^T = 6$ (fourth row) as determined using Monte Carlo samples.

8.2.2 D_s yield extraction

The yield of D_s mesons is estimated in a two dimensional fit to the mass spectrum of D_s candidates and n_X^R. A model composed of signal and background probability density functions is used to obtain the estimateion of the yield.

Background probability density function

The distribution of the mass of the D_s candidates, m_{D_s}, in the right sign sample in Monte Carlo shown in figure 8.2. The background in this distribution can be estimated by using the mass distribution for the wrong sign sample, which is shown in figure 8.3. There is a contribution from events with a real D_s in the wrong sign sample. A yield extraction fit is performed to estimate the size of this contribution. These reconstructions are then removed from the distribution to get a model of wrong sign reconstructions excluding events with real D_s mesons. The resulting distribution is then divided into probability density functions for each value of n_X^R. Due to the definition of the right sign and wrong sign samples there are no wrong sign reconstructions for $n_X^R = 0$. The probability density function for this subsample is determined by taking the average of the probability density functions for the remaining values of n_X^R.

The background probability density function for the right sign sample, B^{RS}, is then expressed as a sum of components:

$$B^{RS}(m_{D_s}, n_X^R) = \sum_{i=0}^{3} b_i B_i^{RS}(m_{D_s}, n_X^R) \tag{8.1}$$

where B_i^{RS} is the probability density function for background events in the right sign sample where $n_X^T = i$, b_i is the coefficient for the component where $n_X^T = i$, and the final coefficient, b_3^{RS} is constrained to ensure the sum of these coefficients is equal to unity.

Signal probability density function

The signal probability density function, S^{RS}, is also expressed as the sum of different components in terms of n_X^R:

$$S^{RS}(m_{D_s}, n_X^R) = \sum_{j=0}^{6} s_j S_j^{RS}(m_{D_s}, n_X^R) \tag{8.2}$$

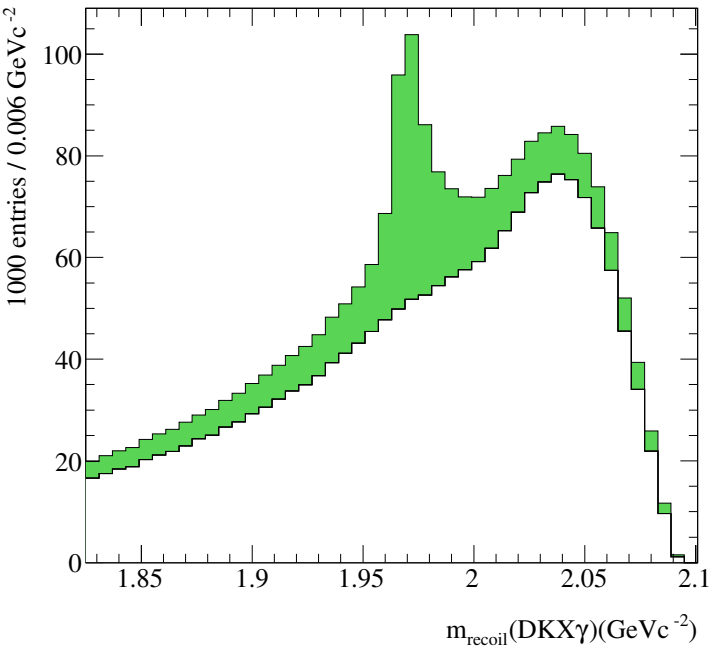

Figure 8.2: m_{D_s} spectrum for the right sign sample in Monte Carlo. The green (shaded) histogram shows reconstruction where a D_s is present. The white histogram shows all other reconstruction.

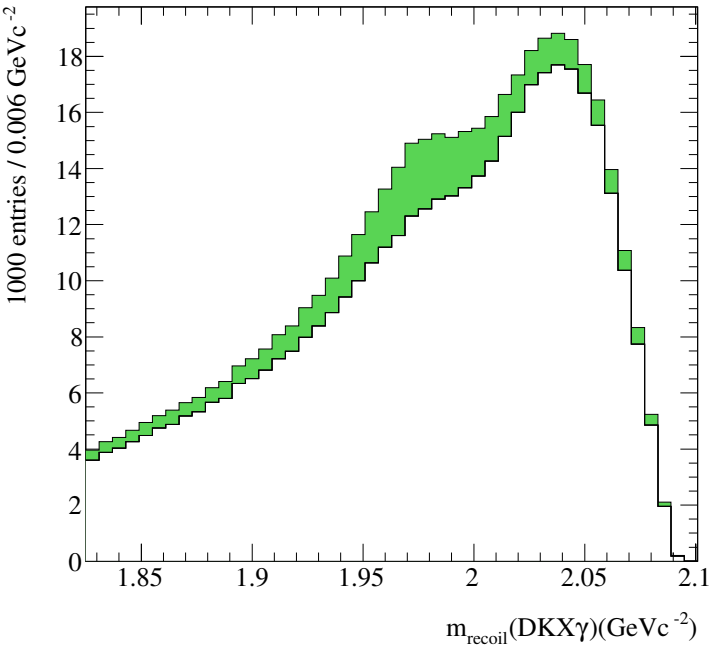

Figure 8.3: m_{D_s} spectrum for the wrong sign sample in Monte Carlo. The green (shaded) histogram shows reconstruction where a D_s is present. The white histogram shows all other reconstruction.

where S_j^{RS} is the probability density function for signal events in the right sign sample where $n_X^T = j$, s_j is the coefficient for the component where $n_X^T = j$, and the coefficients are weighted to sum to unity.

In principle every coefficient would be varied in the yield extraction fit. Unfortunately this leads to divergences and ill-defined results. The coefficients are related to each other using the following model empirically determined:

$$s_j = \frac{(j-\alpha)^\beta e^{-\gamma j}}{\sum_{k=0}^{6}(k-\alpha)^\beta e^{-\gamma k}} \tag{8.3}$$

where α, β and γ are coefficients determined by the yield extraction fit. The position of the maximum in the weight distribution is determined by α. When modeling the data with this model it is found that the result is insensitive to the value of α, and this is understood by noting the n_X^T distribution in data (as shown in figure 8.5), which approximately follows an exponential distribution. The n_X^T distribution in Monte Carlo samples has a local maximum and is sensitive to the value of α. For this reason the value of α is fixed to the value obtained from Monte Carlo studies, $\alpha = -1.32 \pm 0.08$. The fit returns $\beta = 0.27 \pm 0.17$ and $\gamma = 0.28 \pm 0.07$.

Figure 8.4 shows the distribution of n_X^T weights in Monte Carlo, and figure 8.5 shows the weights for data returned by the fit. Figures 8.6 and 8.7 show how these weights change as the values of β and γ are varied by one standard deviation around the fitted values. (Figures 8.6 and 8.7 are not normalised to unit area, to better aid the eye.)

The complete probability density function is then written as

$$P(m_{D_s}, n_X^R) = yS^{RS}(m_{D_s}, n_X^R) + (1-y)B^{RS}(m_{D_s}, n_X^R) \tag{8.4}$$

where y is the fraction of events in the data which contain a D_s meson.

The distribution of reconstructions in the data is described by a two dimensional histogram where the m_{D_s} spectrum satisfies $1.82 < m_{D_s} < 2.12\,\mathrm{GeVc}^{-2}$ and is divided into 50 bins.

The parameters are varied in order to minimise the squares of the residual differences, χ^2:

$$\chi^2 = \sum_i^{bins} \frac{\left(N_i - N^{RS}P_i\right)^2}{\left(\sigma_i^N\right)^2 + \left(N^{RS}\sigma_i^P\right)^2} \tag{8.5}$$

where N_i is the number of reconstructions in the data in a given bin in the histogram,

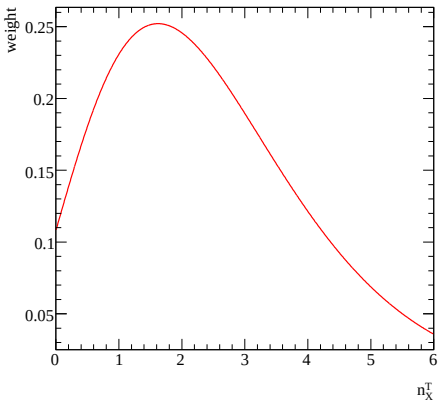

Figure 8.4: The weights for each component in Monte Carlo, determined by counting events.

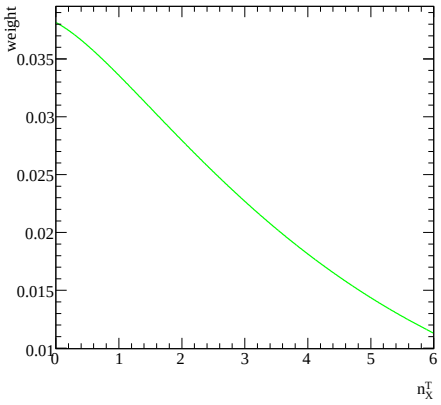

Figure 8.5: The weights for each component in data, determined using a fit to data.

σ_i^N is the uncertainty on the number of reconstructions in the data for that bin, P_i is the contents of the corresponding bin for the probability density function used to describe the signal and background reconstructions and σ_i^P is the uncertainty on the number of reconstructions in the probability density function for that bin. Since the reconstructions are weighted by the number of reconstructions per event, the

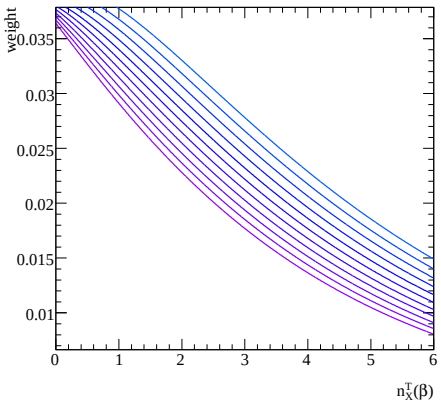

Figure 8.6: The weights as a function of β for each component in data, determined using a fit to data. The blue (upper) functions show how the weights vary with increasing values of β. The variation shown corresponds to one standard deviation either side of the mean value. (These functions are not normalised to unit area.)

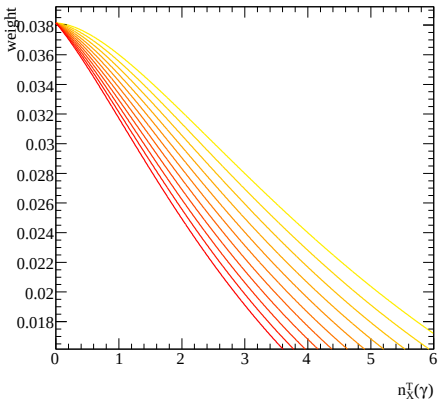

Figure 8.7: The weights for each component in data, determined using a fit to data. The red (lower) functions show how the weights vary with increasing values of γ. The variation shown corresponds to one standard deviation either side of the mean value. (These functions are not normalised to unit area.)

uncertainty on the contents of a bin are calculated as the sum of the squares of these weights.

Due to the low statistics of the wrong sign samples for $n_X^R = 1$, the m_{D_s} spectrum for this sample is determined by taking the average of the spectra for the other values of n_X^R. For the wrong sign sample where $n_X^R = 0$ there is a mass dependent correction, $C(m_{D_s})$, which is applied to the distribution. This correction is determined using Monte Carlo samples, and is shown in 8.8. The proportion of signal events containing a D_s meson in the wrong sign sample is estimated using Monte Carlo samples. The correction factor is consistent with unity in the region of interest.

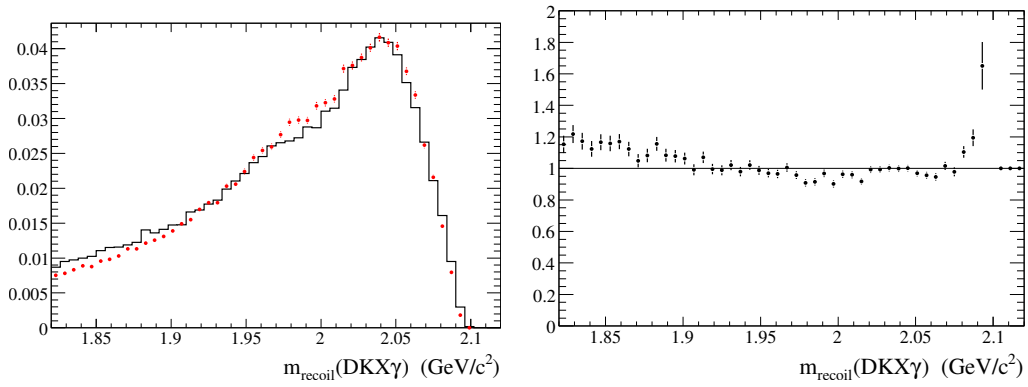

Figure 8.8: The correction applied to the $n_X^R = 0$ wrong sign m_{D_s} spectrum. The plot on the left compares the distributions, where the solid histogram shows the m_{D_s} spectrum for right sign backgrounds where $n_X^R = 0$, and the points show the average m_{D_s} spectrum for wrong sign backgrounds where $n_X^R = 1, 2, 3$. The right hand plot shows the mass dependent correction factor.

There is a small difference in the position of the peak of the m_{D_s} between data and Monte Carlo samples. The probability density function is shifted such that $m_{D_s} \to m_{D_s} - 1.5\,\mathrm{MeVc}^{-2}$ to match the distribution in data, as seen in figure 8.9.

8.2.3 Yield of D_s mesons

Using this model the yield of D_s mesons is estimated to be $67,000 \pm 1,500$. The result of the fit is shown in figure 8.10 for all values of n_X^R, and in figure 8.11 for each value of n_X^R separately.

8.3 $D_s \to \ell\nu_\ell$ yield extraction

The branching fraction for a given final state is determined using the efficiency corrected ratio of yields:

$$\mathcal{B}(D_s \to \ell\nu_\ell) \quad = \quad \frac{N(D_s \to \ell\nu_\ell)}{N(D_s)\sum_{j=0}^{6} s_j R_j(D_s \to \ell\nu_\ell)} \tag{8.6}$$

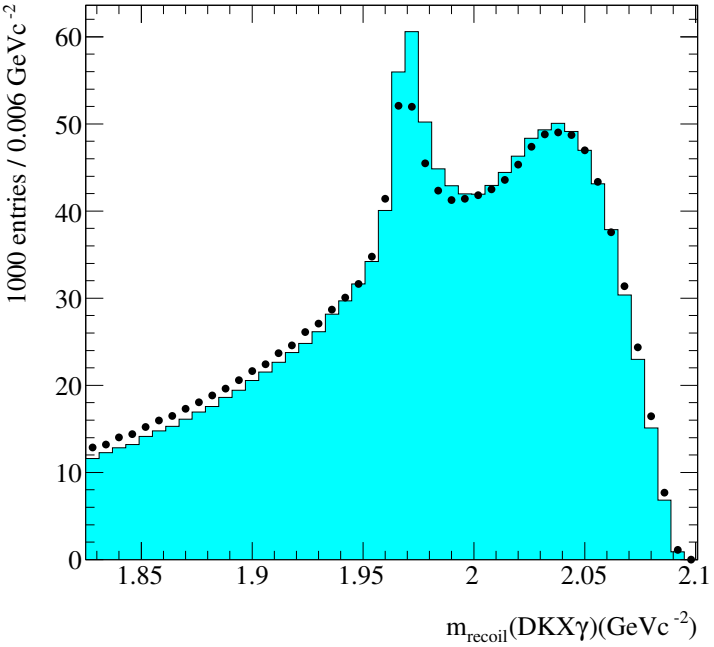

Figure 8.9: The shift in the m_{D_s} spectrum between data and Monte Carlo. The solid histogram shows Monte Carlo reconstructions and the points show data. (The histogram showing Monte Carlo has not been reweighted to match the n_X^T spectrum in data.)

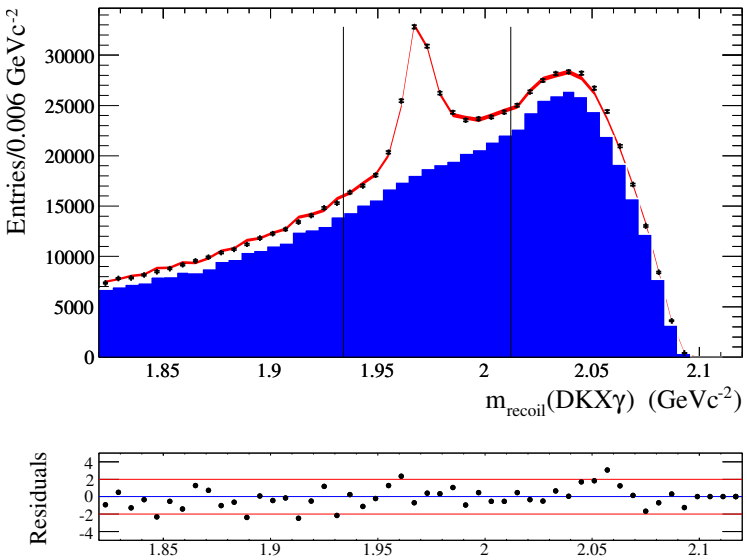

Figure 8.10: The yield extraction fit to data in projection to the m_{D_s} spectrum. The blue (solid) histogram shows the background probability density function. The empty histogram shows the signal probability density function. The red bands shows the uncertainty in the yield for each value of m_{D_s}. The points show the data. The vertical lines show selecton criteria. (Benitez 2010)

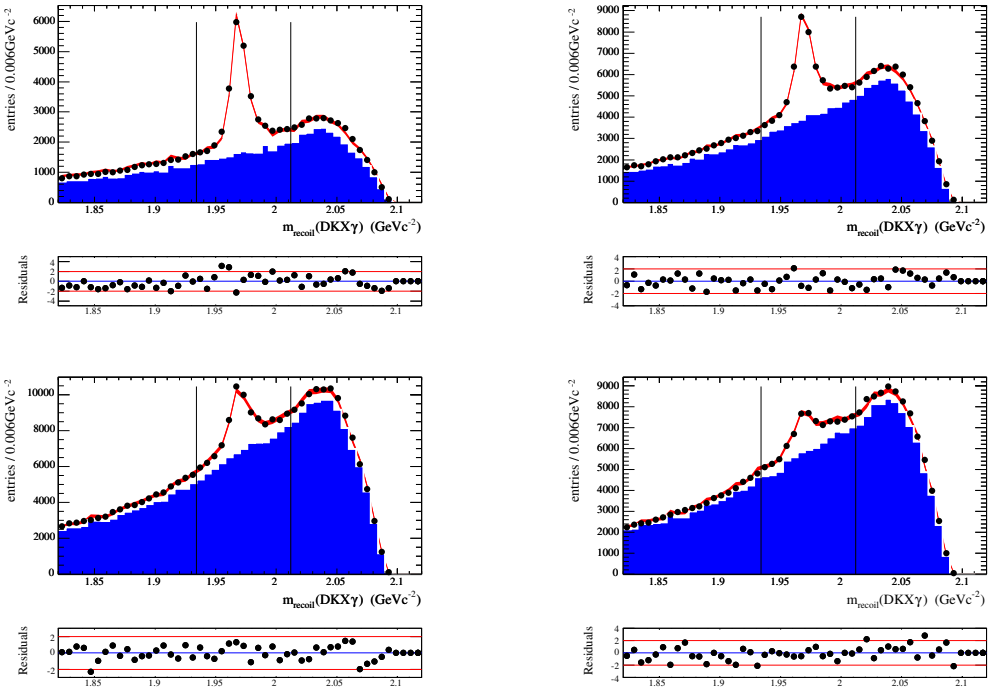

Figure 8.11: The yield extraction fit to data in projection to the m_{D_s} spectrum. The blue (solid) histogram shows the background probability density function. The empty histogram shows the signal probability density function. The red bands shows the uncertainty in the yield for each value of m_{D_s}. The points show the data. The vertical lines show selecton criteria. The plots show the fit for $n_X^R = 0$ (top left), $n_X^R = 1$ (top right), $n_X^R = 2$ (bottom left), and $n_X^R = 3$ (bottom right). (?)Jose)

$$R_j(D_s \to \ell\nu_\ell) \quad = \quad \frac{\varepsilon_j(D_s \to \ell\nu_\ell)}{\varepsilon_j(D_s)} \tag{8.7}$$

where $N(D_s \to \ell\nu_\ell)$ is the number of $D_s \to \ell\nu_\ell$ reconstructions determined by the yield extraction fit, $N(D_s)$ is the number of D_s mesons determined by the yield extraction fit, $\varepsilon_j(D_s \to \ell\nu_\ell)$ is the efficiency of reconstruction for an event of the type $D_s \to \ell\nu_\ell$ where $n_X^T = j$, and $\varepsilon_j(Ds)$ is the efficiency of reconstruction for an event containing a D_s meson where $n_X^T = j$. These efficiencies are estimated using Monte Carlo samples.

The signal and background are divided into different components, which are labelled accoring to the legend shown in figure 8.12.

8.3.1 Yield extraction variables

The yield extraction is determined using one of two variables, depending on the final state topology. Both variables are well suited to analyses with neutrinos in the final state and have been used previously in other studies.

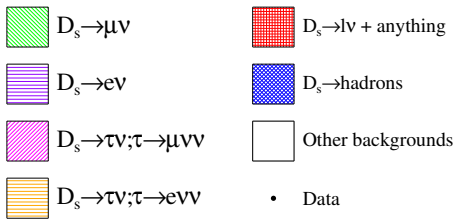

Figure 8.12: Legend for the background components for the $D_s \to \ell\nu_\ell$ reconstruction.

$D_s \to e\nu_e$ and $D_s \to \mu\nu_\mu$ modes

For the events of the type $D_s \to e\nu_e$ and $D_s \to \mu\nu_\mu$ there should be a single neutrino in the final state, and since the centre of mass frame energy is known, using conservation of four-momentum it is possible to reconstruct the invariant mass squared of the neutrino candidate. For real $D_s \to e\nu_e$ and $D_s \to \mu\nu_\mu$ events this should peak at zero GeV^2c^{-4}. This variable is known as m_m^2, and has been used in other analyses to extract a yield (Widhalm 2008). Figure 8.13 shows the m_m^2 distributions for signal Monte Carlo samples for the $D_s \to e\nu_e$ and $D_s \to \mu\nu_\mu$ modes. The long tail in the m_m^2 distribution for the $D_s \to e\nu_e$ mode are due to radiative processes, which are more prevalent for electrons. Figure 8.14 shows the m_m^2 distributions for generic Monte Carlo samples for the $D_s \to e\nu_e$ and $D_s \to \mu\nu_\mu$ modes. The hadronic component in the m_m^2 distribution for the $D_s \to \mu\nu_\mu$ mode arises due to misidentification of charged pions and kaons as muons in the BaBar detector. These backgrounds are particularly persistent as both charged pions and kaons can decay in flight to muons and neutrinoes. Otherwise the contributions to the backgrounds for both modes are similar in their compositions, with dominant backgrounds arising from semileptonic decays of the D_s meson and from $D_s \to \tau\nu_\tau$ decays.

$D_s \to \tau\nu_\tau$ modes

When considering events of the type $D_s \to \tau\nu_\tau; \tau \to e\nu_e\nu_\tau$ and $D_s \to \tau\nu_\tau; \tau \to \mu\nu_\mu\nu_\tau$ there are three neutrinos in the final state. This means that the distribution of invariant masses squared of the neutrino systems has a broad spectrum, making a yield extraction with this variable difficult. Neutrinos interact with other particles very rarely, so as the three neutrinos pass through the detector they should not deposit any energy. The extra energy deposited in the electromagnetic calorimeter, E_{extra}, is defined in the following way:

-

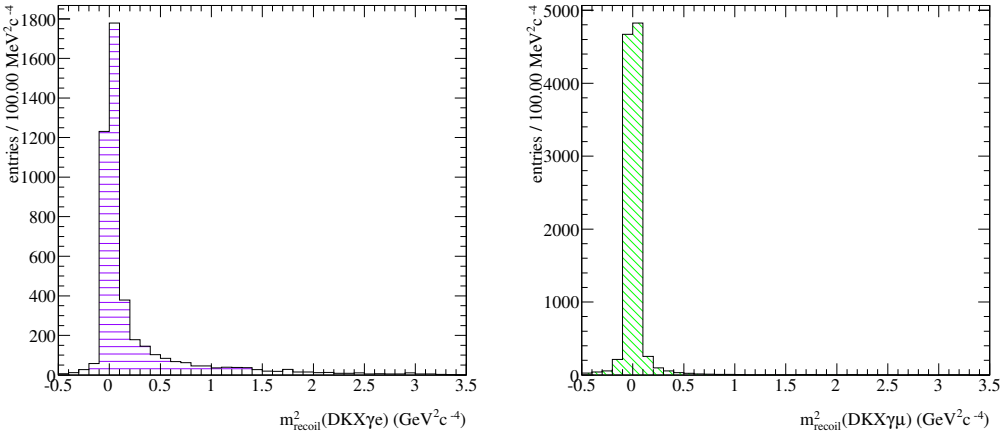

Figure 8.13: m_m^2 distributions for signal Monte Carlo for the $D_s \to e\nu_e$ mode (left) and $D_s \to \mu\nu_\mu$ mode (right).

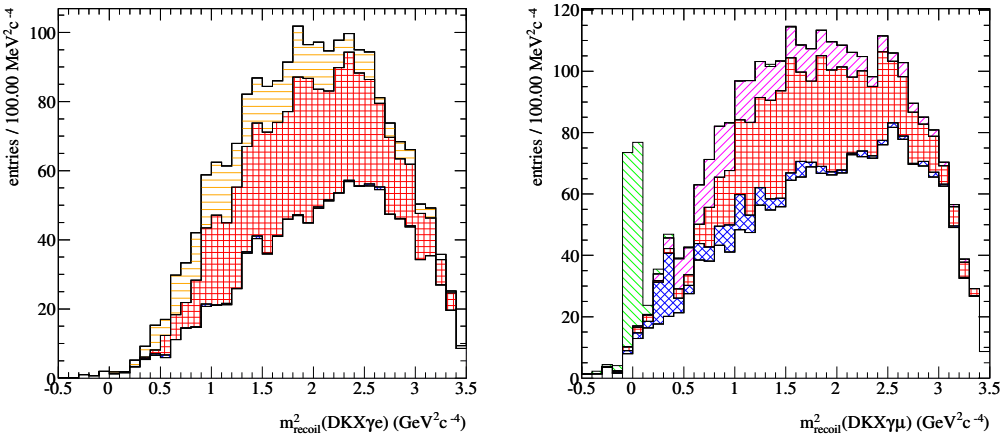

Figure 8.14: m_m^2 distributions for generic Monte Carlo for the $D_s \to e\nu_e$ mode (left) and $D_s \to \mu\nu_\mu$ mode (right).

- Each cluster of crystals (a group of neighbouring crystals within the electromagnetic calorimeter, where the size and shape of the cluster depends upon its position in the electromagnetic calorimeter) in the electromagnetic calorimeter with energy deposition is added to a list (known as the `CalorNeutral` list.)

- A second list of clusters is formed, called the `EExtraNeutral` list, which contains all the clusters from the `CalorNeutral` list where:

  – no cluster has been associated with the reconstruction of the rest of the event.

  – no cluster has an energy deposition of less than 30 MeV.

- The sums of energies of clusters in the `EExtraNeutral` list is the extra energy, E_{extra}.

The purpose of the selection criterion of 30 MeV is to reduce electronic noise. In principle the crystals in the electromagnetic calorimeter should be able to report energies down to 0 MeV. However in practice it is not possible to reliably separate such small electronic signals from electronic noise, so energies of clusters must be above a given threshold. Previous work on BaBar has shown that a threshold of $20 - 30$ MeV is sufficient to reduce most electronic noise (Aubert 2006). Figure 8.15 shows the E_{extra} distributions for signal Monte Carlo samples for the $D_s \to \tau\nu_\tau; \tau \to e\nu_e\nu_\tau$ and $D_s \to \tau\nu_\tau; \tau \to \mu\nu_\mu\nu_\tau$ modes. Figure 8.16 shows the E_{extra} distributions for generic Monte Carlo samples for the $D_s \to \tau\nu_\tau; \tau \to e\nu_e\nu_\tau$ and $D_s \to \tau\nu_\tau; \tau \to \mu\nu_\mu\nu_\tau$ modes.

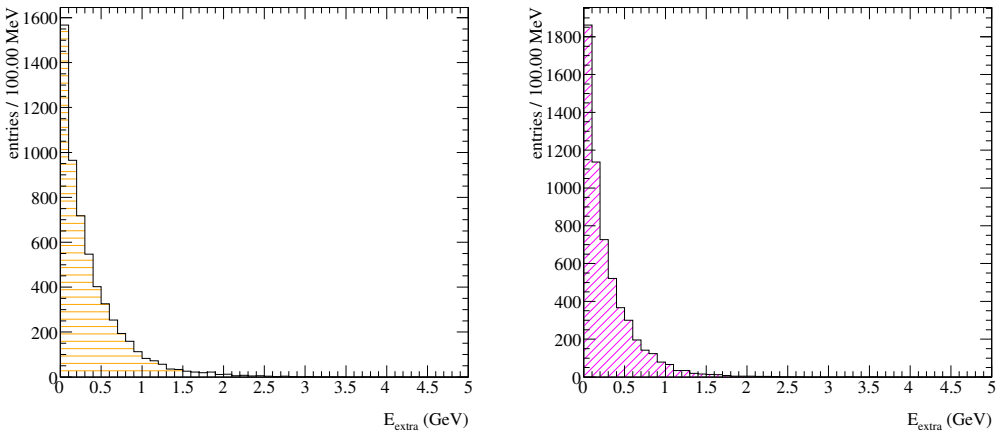

Figure 8.15: E_{extra} distributions for signal Monte Carlo for the $D_s \to \tau\nu_\tau; \tau \to e\nu_e\nu_\tau$ mode (left) and $D_s \to \tau\nu_\tau; \tau \to \mu\nu_\mu\nu_\tau$ mode (right).

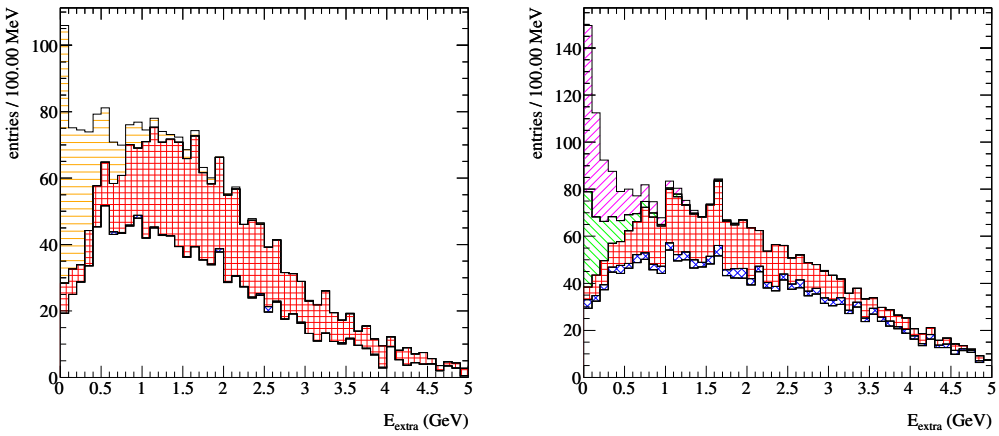

Figure 8.16: E_{extra} distributions for generic Monte Carlo for the $D_s \to \tau\nu_\tau; \tau \to e\nu_e\nu_\tau$ mode (left) and $D_s \to \tau\nu_\tau; \tau \to \mu\nu_\mu\nu_\tau$ mode (right).

8.3.2 Background suppression

To reduce the hadronic backgrounds a multivariate study was performed, aimed at rejecting events where the lepton candidate is a misidentified hadron. The dominant backgrounds include:

- $D_s \to K^0 K^{\pm}$, where the charged kaon is misidentified as a lepton.
- $D_s \to \eta\pi^{\pm}$, where the charged pion is misidentified as a lepton.
- $D_s \to \phi\pi$, where the charged pion is misidentified as a lepton.

The generic Monte Carlo was separated into two samples. Sample A contained Run 5 OnPeak candidates and Sample B contains all other candidates. The samples were further separated into events where the lepton candidates were leptons and where they were hadrons. `StatPatternRecognition` `BumpHunter` (Narsky 2006) was used to separate these two subsamples. Events with hadronic lepton candidates were assigned the label signal and events with correctly identified leptonic candidates were assigned the label background. `BumpHunter` was trained on Sample B and tested on Sample A, returning a series of selection criteria that maximise the significance, θ,

$$\theta = \frac{N_S}{\sqrt{N_S + N_B}} \tag{8.8}$$

where N_S is the number of signal (hadronic) lepton candidates and N_B is the number of background (correctly identified) leptonic candidates.

The weight of the hadronic lepton candidate events were varied by 50% to 150% of the true value (determined using Monte Carlo), in steps of 10%. The peel parameter (described in section 6.3) was varied from 0.0 to 0.99 in steps of 0.01. The `BumpHunter` analysis was performed using the following variables:

- E_{extra}
- p_{ℓ}^{lab}, the momentum of the lepton candidate in the laboratory frame.
- m_{D_s}, the mass of the D_s candidate after the kinematic fit is performed to the whole event, including the lepton candidate.
- Lepton selector used to identify lepton candidates.

The spectra for these variables are shown in figures 8.17, 8.18, and 8.19.

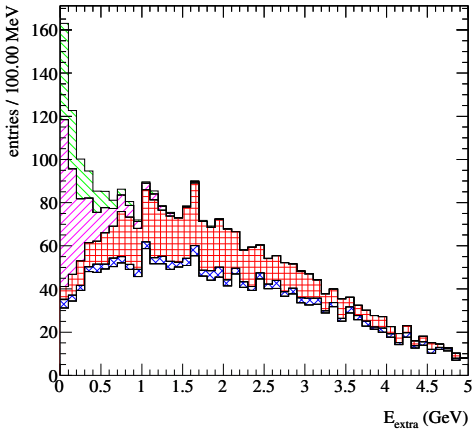

Figure 8.17: E_{extra} distribution used in the `BumpHunter` study for the $D_s \to \mu\nu_\mu$ mode.

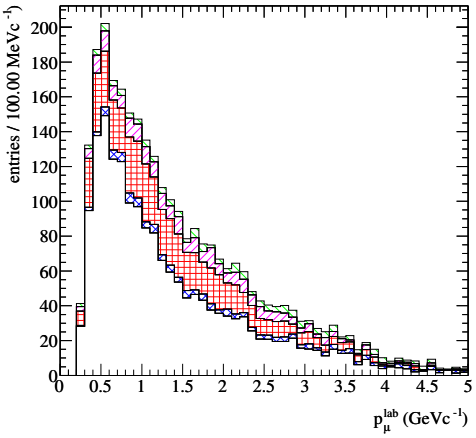

Figure 8.18: p_ℓ^{lab} distribution used in the `BumpHunter` study for the $D_s \to \mu\nu_\mu$ mode.

The study only returned cuts for some variables. Based upon these results only one selection criterion was used (obtained by reversing the selection criteria obtained from `BumpHunter`):

- $E_{extra} < 1\,\text{GeV}$

This selection criterion was chosen based upon the relative stability of the returned values as a function of weight and peel parameter, as is evident in figure 8.20. Figure 8.21 shows the m_m^2 spectrum for hadronic backgrounds before and after the selection criterion is applied.

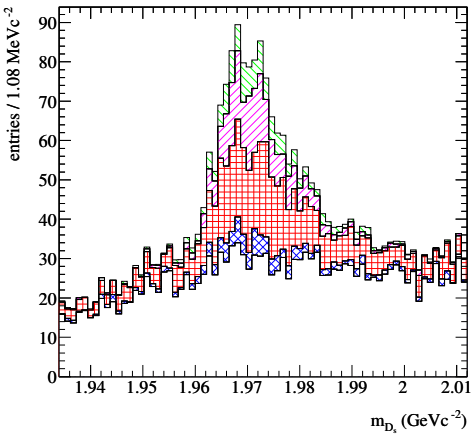

Figure 8.19: m_{D_s} distribution used in the `BumpHunter` study for the $D_s \to \mu\nu_\mu$ mode.

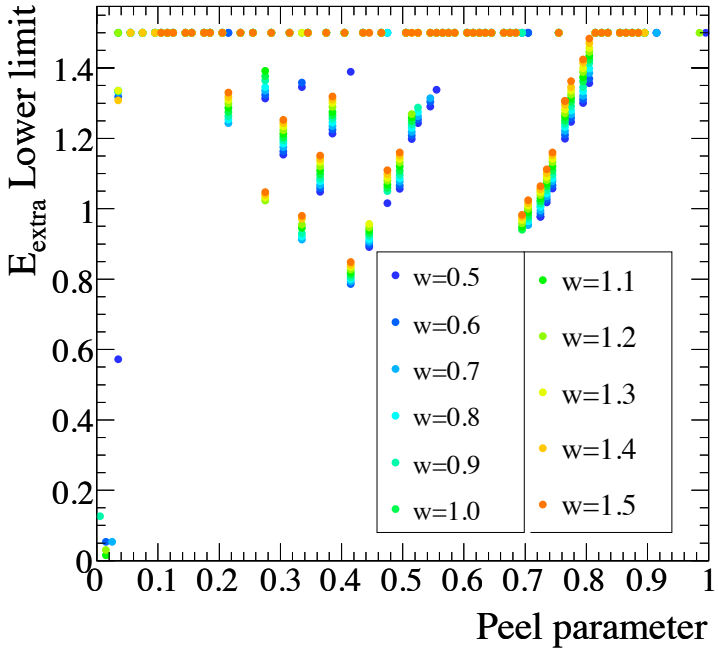

Figure 8.20: The results of the background suppression study using SPR `BumpHunter`. (Narsky 2006). w refers to the weight of the candidates.

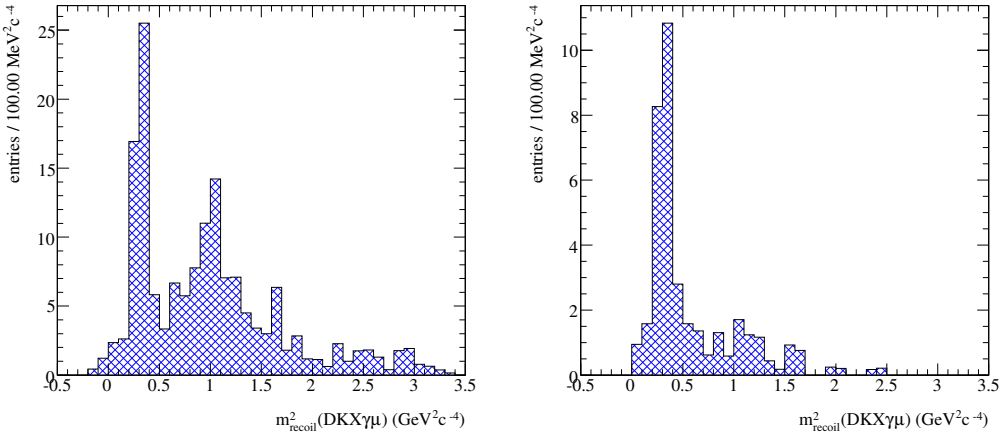

Figure 8.21: The m_m^2 distribtion for hadronic backgrounds before (left) and after (right) the selection criterion determined using the `BumpHunter` study is applied, for the $D_s \to \mu\nu_\mu$ mode. The remaining peak in the spectrum is composed of $D_s \to K^0 K$ events, where the K^0 is a K_L^0 meson.

8.3.3 Yield extraction of $D_s \to e\nu_e$ events

The number of $D_s \to e\nu_e$ events in data is estimated by a yield extraction fit in the invariant mass squared of the neutrino system. Due to the large number of misidentified hadrons in the high m_m^2 region, candidates are required to satisfy $E_{extra} < 1\,\text{GeV}$. The total number of events is estimated to be 1.94 ± 1.87, which is consistent with 0, and where the uncertainty accounts for only the statistical variation of the data and Monte Carlo samples. The result of the fit is shown in figure 8.22. This plot shows the signal probability density function (shaded purple histogram, absent in this fit), the total probability density function (empty histogram), and the data (black points). The normalised residual differences are shown underneath the plot. The residual difference for a bin, i, is given by:

$$\chi_i^2 = \frac{\left(N_{data} - N_{MC}\right)^2}{\sigma_{MC}^2 + \sigma_{data}^2} \tag{8.9}$$

where χ_i^2 is the residual difference for the ith bin, N_{data} is the number of data events in the ith bin, σ_{data} is the statistical uncertainty on this value, N_{MC} is the number of Monte Carlo events in the ith bin, and σ_{MC} is the statistical uncertainty on this value.

The normalised residual difference is a signed difference, indicating the sign of the difference between Monte Carlo and data samples:

$$\Delta_{norm} = \frac{N_{data} - N_{MC}}{\sqrt{\sigma_{MC}^2 + \sigma_{data}^2}} \tag{8.10}$$

8.3.4 Yield extraction of $D_s \to \mu\nu_\mu$ events

The number of $D_s \to \mu\nu_\mu$ events is estimated by a yield extraction fit in the invariant mass squared of the neutrino system. The total number of events is estimated to be 274.1 ± 16.9 where the uncertainty accounts for only the statistical variation of the data and Monte Carlo samples. The result of the fit is shown in figure 8.23. This plot shows the signal probability density function (shaded green histogram), the total probability density function (empty histogram), and the data (black points). Figure 8.23 shows excellent agreement between data and Monte Carlo samples, indicating a successful fit and a reliable determination of the yield of signal events.

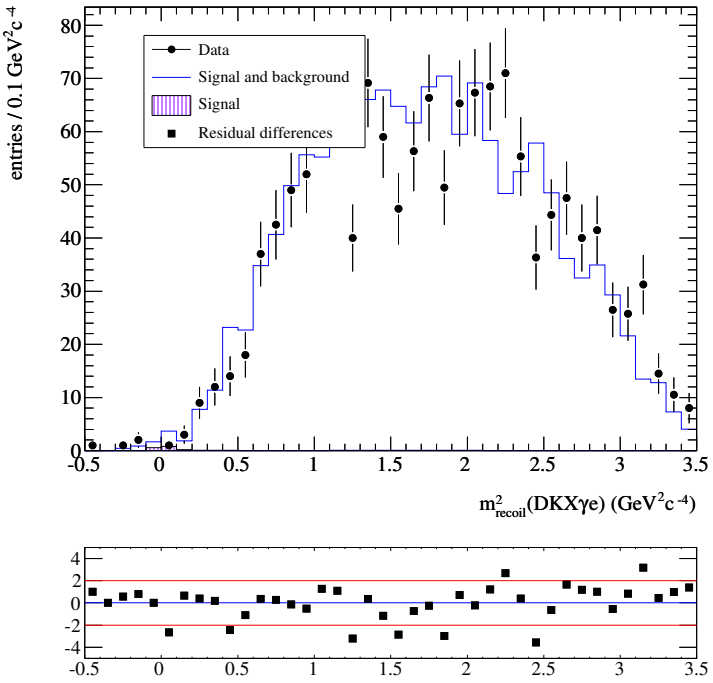

Figure 8.22: The result of the yield extraction fit for the $D_s \to e\nu_e$ mode.

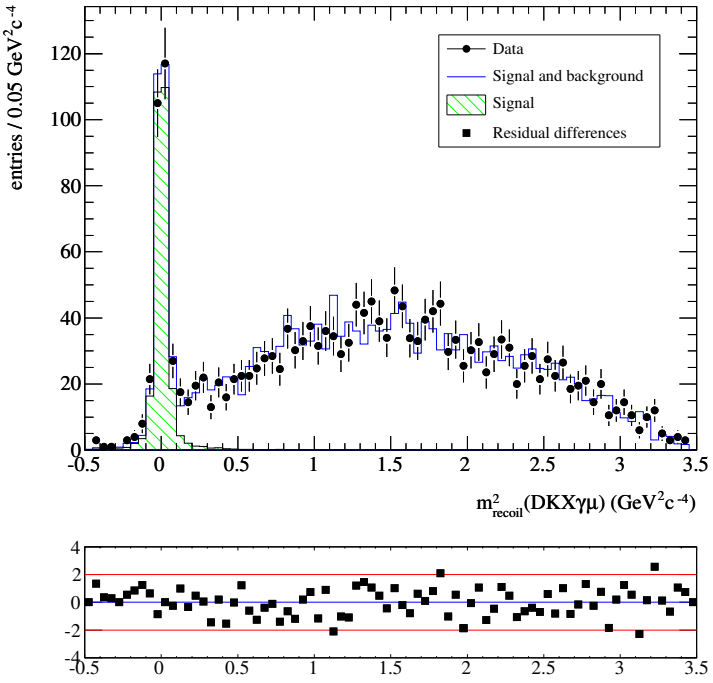

Figure 8.23: The result of the yield extraction fit for the $D_s \to \mu\nu_\mu$ mode.

8.3.5 Yield extraction of $D_s \to \tau\nu_\tau; \tau \to e\nu_e\nu_\tau$ events

The number of $D_s \to \tau\nu_\tau; \tau \to e\nu_e\nu_\tau$ events is estimated by a yield extraction fit in the E_{extra} distribution. The total number of events is estimated to be 433.4 ± 40.9

where the uncertainty accounts for only the statistical variation of the data and Monte Carlo samples. The result of the fit is shown in figure 8.24. This plot shows the signal probability density function (shaded orange histogram), the total probability density function (empty histogram), and the data (black points). The normalised residual differences indicate a reliable result.

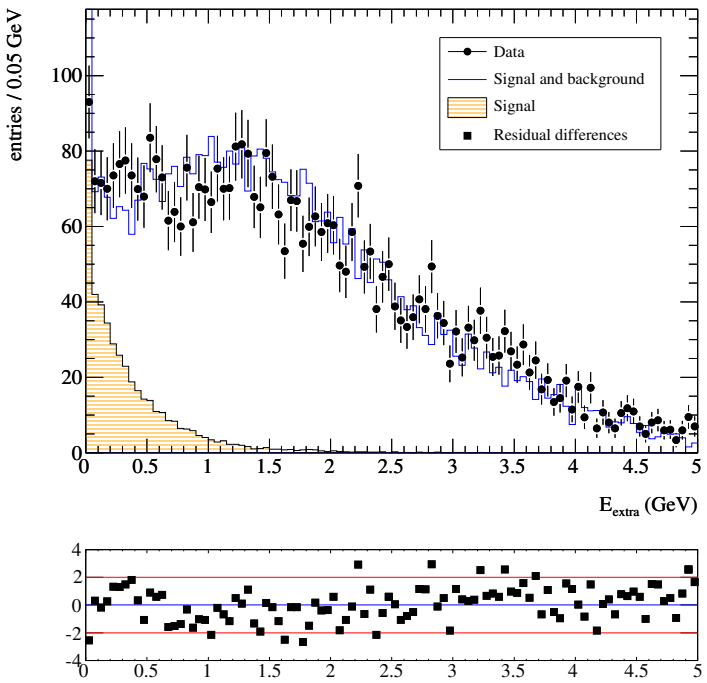

Figure 8.24: The result of the yield extraction fit for the $D_s \to \tau\nu_\tau; \tau \to e\nu_e\nu_\tau$ mode.

8.3.6 Yield extraction of $D_s \to \tau\nu_\tau; \tau \to \mu\nu_\mu\nu_\tau$ events

The number of $D_s \to \tau\nu_\tau; \tau \to \mu\nu_\mu\nu_\tau$ events is estimated by a yield extraction fit in the E_{extra} distribution. However, there are a significant number of events of the type $D_s \to \mu\nu_\mu$ which peak in the same region as $D_s \to \tau\nu_\tau; \tau \to \mu\nu_\mu\nu_\tau$ events. To remove these events candidates must satisfy $m_m^2 > 0.5\,\mathrm{GeV^2c^{-4}}$. The distribution of m_m^2, with the selection criterion indicated, is shown in figure 8.25. The total number of events is estimated to be 334.1 ± 32.0 where the uncertainty accounts for only the statistical variation of the data and Monte Carlo samples. The result of the fit is shown in figure 8.24. This plot shows the signal probability density function (shaded pink histogram), the total probability density function (empty histogram), and the data (black points). The normalised residual difference indicate a reliable result.

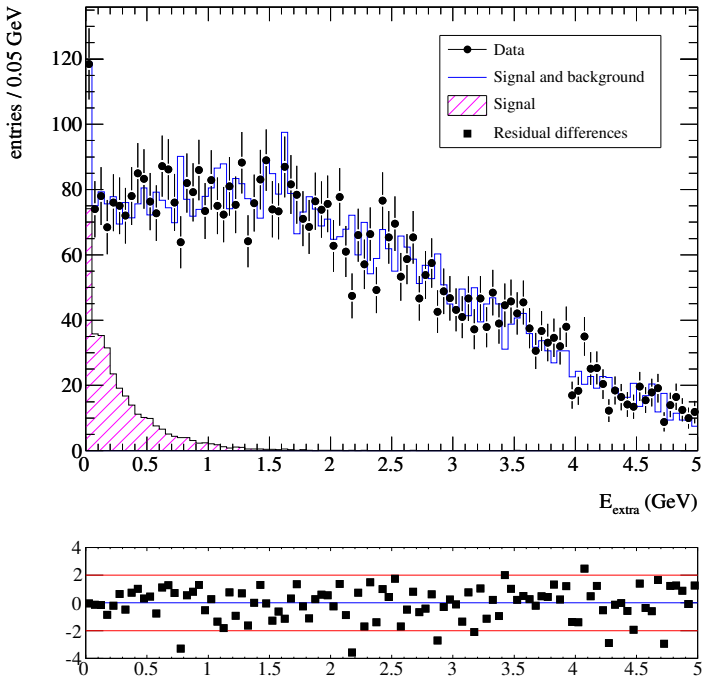

Figure 8.25: The result of the yield extraction fit for the $D_s \to \tau\nu_\tau; \tau \to \mu\nu_\mu\nu_\tau$ mode.

8.4 Summary

By taking the efficiency corrected ratio of yields of $D_s \to \ell\nu_\ell$ events and D_s events the branching fractions $\mathcal{B}(D_s \to \ell\nu_\ell)$ can be estimated. These estimations are sensitive to the n_X^T spectrum in data, which must be determined using a two dimensional fit to n_X^R and $m(D_s)$. The calculation of the branching fractions $\mathcal{B}(D_s \to \ell\nu_\ell)$ must be accompanied by the relevant systematic uncertainties, which are oultined in the following chapter.

Chapter 9

Systematic uncertainties and validation

9.1 Overview

This chapter outlines the systematic uncertainties associated with the reconstruction and yield extraction for events of the type $D_s \to \ell\nu_\ell$. The uncertainties associated with the reconstruction of the tagging system cancel out exactly, so their contribution is not calculated. The first series of systematic uncertainties to be described apply to the D_s yield extraction. The second series of systematic uncerainties correspond to the $D_s \to \ell\nu_\ell$ yield extraction.

9.2 D_s yield estimation

9.2.1 Estimation of right sign and wrong sign components

The weights for each n_X^T component which are applied to the wrong sign sample are determined using Monte Carlo studies. However the distribution of n_X^T in data has a lower average value than for Monte Carlo. To investigate how this difference can affect the yield the weights are transformed linearly according to

$$b_i \to 1 - \frac{b_i - 3}{3} \tag{9.1}$$

where b_i is the weight for the component where $n_X^T = i$. The change in yield of D_s mesons is taken as the uncertainty.

The weights which describe the n_X^T distribution for the right sign sample are defined by a model (described in equation 8.1) which is insensitive to the parameter α. This parameter is varied in the range $-10 < \alpha < -0.5$ and the change in yield of D_s mesons is taken as the uncertainty.

9.2.2 D_s signal model

The width of the mass peak in the signal probability density function is varied by smearing the probability density function in the following way. A Gaussian distribution, G, is defined with mean of zero $\mathrm{GeV^2c^{-4}}$ and a standard deviation of $2\,\mathrm{MeVc^{-2}}$. For each entry in the Signal Monte Carlo, the value of m_{D_s} is added to a random number generated from G. After applying this smearing the change in yield of D_s mesons is taken as the uncertainty.

9.2.3 D_s peaking backgrounds

There are two sources of peaking background in the D_s yield estimation. The first source is the proportion of the wrong sign sample which contains D_s mesons, which is determined using Monte Carlo samples. The second source is the decay of the excited meson $D^{\star 0} \to D^0\gamma$, where the mass difference, $m_{D^{\star 0}} - m_{D^0}$, is similar to that of the mass difference $m_{D_s^\star} - m_{D_s}$. To estimate the uncertainty introduced by these peaking backgrounds the weights of reconstructions in the peaking backgrounds in the Monte Carlo simulation are varied by 10% (which is the approximate contribution of the peaking background to the total yield in this region) and the change in yield of D_s mesons is taken as the uncertainty. Figure 9.1 shows the contribution to the wrong sign sample from the reconstruction containing D_s mesons.

9.2.4 Hadronisation system crossfeed estimation

In order to investigate how the crossfeed between n_X^R and n_X^T can affect the yield of D_s mesons the distribution is smeared in the following way. For each value of n_X^T 10% of the reconstructions are moved from the most populated bin in n_X^R to neighbouring bins and the yield is determined after this migration. Similarly reconstructions are moved from neighbouring bins into the most populated bin in n_X^R and the yield is determined after this migration. The larger change in yield of D_s mesons is taken as the uncertainty.

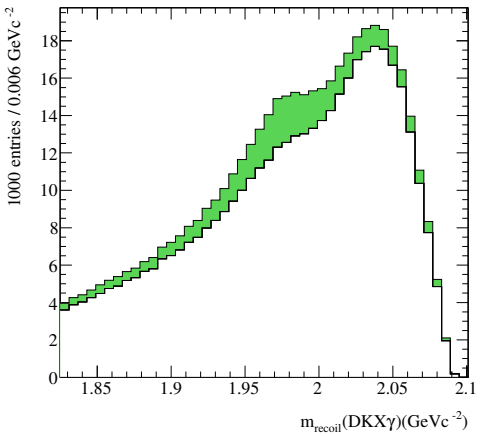

Figure 9.1: The wrong sign sample for the denominator for Monte Carlo. The white histogram shows the reconstruction where a D_s is not present. The shaded (green) histogram shows the reconstruction where a D_s meson is present.

9.2.5 Signal photon identification

Identification of the photon in the decay $D_s^\star \to D_s\gamma$ has many sources of background, including:

- Real photons from neutral meson decays (mainly π^0 and η.)
- Charged particles and K_L^0 mesons interacting with the electromagnetic calorimeter.

The weights of reconstuctions of these components in the Monte Carlo simulation are varied by 5% and the change in yield of D_s mesons is taken as the uncertainty, where 5% is approximately equal to the average contribution from each background source in the region of interest. Figure 9.2 shows these components.

9.3 $\mathcal{B}(D_s \to \ell\nu_\ell)$ estimation

9.3.1 Track reconstruction

The track reconstruction efficiency of the BaBar detector and software system is determined by the BaBar Tracking Group using events of the type $e^+e^- \to \tau^+\tau^-$ decaying to 1 or 3 charged particles. The uncertainty of the efficiency of reconstruction introduced by the identification of a track is found to be 0.83% per track. Since this analysis in concerned with the ratio of efficiencies between two states, the uncertainties

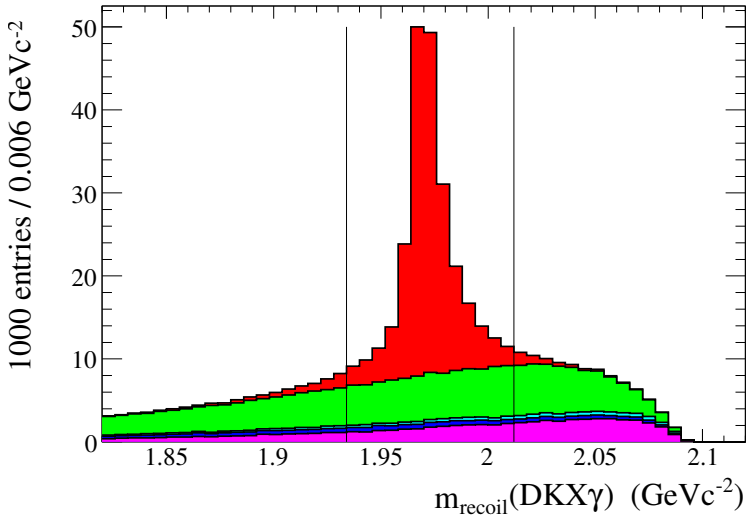

Figure 9.2: The sources of signal photon candidates. The histograms (from top to bottom) show photon candidates from $D_s^\star \to D_s\gamma$ decays, from $\pi^0/\eta \to \gamma\gamma$ decays, from charged particles radiating photons, from other radiative hadronic decays, and from interaction of hadronic matter with the detector. The vertical lines indicate selection criteria. (Benitez 2010)

due to particles common to both states cancel out exactly. Therefore the uncertainty is introduced for only the charged lepton candidates.

9.3.2 Particle identification

As described in section 6.7.1 the BaBar Particle Identification Group provide many tools for the evaluation of particle identification efficiencies and uncertainties. This analysis uses the control samples prepared by the Particle Identification Group and as a result there are uncertainties associated with the differences between the Monte Carlo samples and data used to determine the efficiencies.

The selector efficiency uncertainty has two components. The first component comes from the statistical limitations of the sample. To estimate this component of the uncertainty the sample of signal events is split into bins of momenta and polar angle and then each bin is multiplied by the error taken from the tables provided by the Particle Identification Group. These errors are then added in quadrature and weighted run by run according to luminosity and charge. For a given charge, q, and running period, r, the statistical uncertainty is summed over all bins in quadrature:

$$\sigma^2_{stat} = \frac{\sum_{pqrt} n^2_{pqrt}\sigma^2_{pqrt}}{\left(\sum_{pqrt} n_{pqrt}\right)^2} \tag{9.2}$$

where n_{pqrt} is the content of the bin for a given value of momentum, charge, running period and polar angle and σ_{pqrt} is the uncertainty corresponding to the ratio of efficiencies between Monte Carlo and data taken from the particle identification tables in that bin of momentum, charge, running period and polar angle.

The second component of the uncertainty is associated with the detector environment, which is unique to each analysis. Variations in the number of charged particles and photons leads to variations in the selector efficiency, contributing to the overall uncertainty. This uncertainty arises because the control sample used to determine the particle identification efficiencies is different to the signal Monte Carlo sample. The uncertainty is estimated by comparing the number of candidates which pass the selector and the number of candidates in the `ChargedTracks` list weighted according to the tables provided by the Particle Identification Group. The uncertainties are correlated across runs so a weighted error is taken when summing over runs.

The change in efficiency, $\delta\varepsilon$ is

$$2\sigma_{env} = \delta\varepsilon = \frac{N_{selector}}{N} - \frac{\sum_{pqrt} \varepsilon_{pqrt} n_{pqrt}}{N} \tag{9.3}$$

where N is the total number of candidates in the sample, $N_{selector}$ is the number of candidates that pass the selector, ε_{pqrt} is the efficiency of the selector in a given bin as determined by the control sample and n_{pqrt} is the number of signal candidates in that bin. The total efficiency obtained using the particle identification table is $(\sum_{pqrt} \varepsilon_{pqrt} n_{pqrt})/N$.

These uncertainties are then added in quadrature:

$$\sigma^2 = \sigma^2_{stat} + \sigma^2_{env} \tag{9.4}$$

The uncertainties for the different branching fractions are shown in table 9.1. The environmental uncertainty is typically much larger for muons than for electrons, due to the relatively high rate of misidentification of hadrons.

9.3.3 Yield extraction studies

In order to ensure the yield extraction fit does not bias the estimation of the yield of events a number of validation studies are performed.

Table 9.1: Uncertainties associated with particle identification.

Decay mode	Uncertainty
$D_s \to e\nu_e$	0.2%
$D_s \to \mu\nu_\mu$	1.9%
$D_s \to \tau\nu_\tau; \tau \to e\nu_e\nu_\tau$	0.2%
$D_s \to \tau\nu_\tau; \tau \to \mu\nu_\mu\nu_\tau$	1.9%

Toy studies

A 'toy' distribution is a distribution which is used to study how statistical variations can affect the result returned by a yield extraction fit. The toy distributions are generated using the accept-reject method in the following way:

- A sample of background reconstructions is taken from generic Monte Carlo.
- A sample of signal reconstructions is taken from signal Monte Carlo.
- An accept-reject model is constructed:
  - The samples are arranged into bins in the variable of interest.
  - The samples are weighted and combined bin by bin to form a single sample. (This weighting allows the number of signal reconstructions to be varied to investigate stability of the yield extraction fit as a function of branching fraction.)
  - A random number, n, is generated from a Gaussian distribution with a mean equal to the number of reconstructions in the combined sample and with a standard deviation equal to the square root of this number.
  - A bin, i, is chosen at random.
  - A random number, x, is generated from a uniform distribution of $10,000$ steps in the range $0 < x < h$, where h is the content of the bin with the largest number of entries in the distribution.
  - If x is less than or equal to the content of bin i then that bin is incremented in the toy distribution.
  - This process is repeated until the number of events in the toy distribution is within one reconstruction of the randomly generated number, n.

Table 9.2: Results of the toy studies for the $D_s \to \mu\nu_\mu$, $D_s \to \tau\nu_\tau; \tau \to e\nu_e\nu_\tau$, and $D_s \to \tau\nu_\tau; \tau \to \mu\nu_\mu\nu_\tau$ modes.

Mode	Mean	Standard deviation
$D_s \to \mu\nu_\mu$	-0.001 ± 0.036	0.986 ± 0.035
$D_s \to \tau\nu_\tau; \tau \to e\nu_e\nu_\tau$	-0.095 ± 0.036	0.976 ± 0.034
$D_s \to \tau\nu_\tau; \tau \to e\nu_e\nu_\tau$	-0.039 ± 0.036	0.989 ± 0.035

- The number of reconstructions in the distribution is scaled to the randomly generated number, n, which is generally not an integer value.
- The toy distribution is fitted using the signal and background probability density functions.

The pull for a given fit is defined as

$$Pull = \frac{n_{fit} - n_{true}}{\sigma_{fit}} \tag{9.5}$$

where n_{fit} is the number of reconstruction determined by the yield extraction fit, σ_{fit} is the statistical uncertainty returned by the yield extraction fit and n_{true} is the number of signal reconstructions that is included in the combined sample of reconstructions. If the yield extraction fit converges then the value of the pull is stored to a histogram.

If the yield extraction fit returns unbiased results then for a large enough set of toy distributions the pull should be well described by a Gaussian distribution with a mean equal to 0 and a standard deviation equal to 1. The values of the mean and standard deviations of the pulls are shown in table 9.2. (Since the number of signal events for the $D_s \to e\nu_e$ mode in the Monte Carlo samples is equal to zero, the pull for this mode cannot be determined directly, and is excluded from the study.)

The number of signal reconstructions is varied in the range $(75\% - 125\%) \times n(D_s \to \ell\nu_\ell)_{MC}$ in steps of 5% in order to determine how a different branching fraction might affect the pull distribution. The pull distributions for the $D_s \to \mu\nu_\mu$ mode are shown in figure 9.3.3, showing no bias and excellent performance for the yield extraction fits. These toy studies were performed using $1,000$ toy distributions for each study.

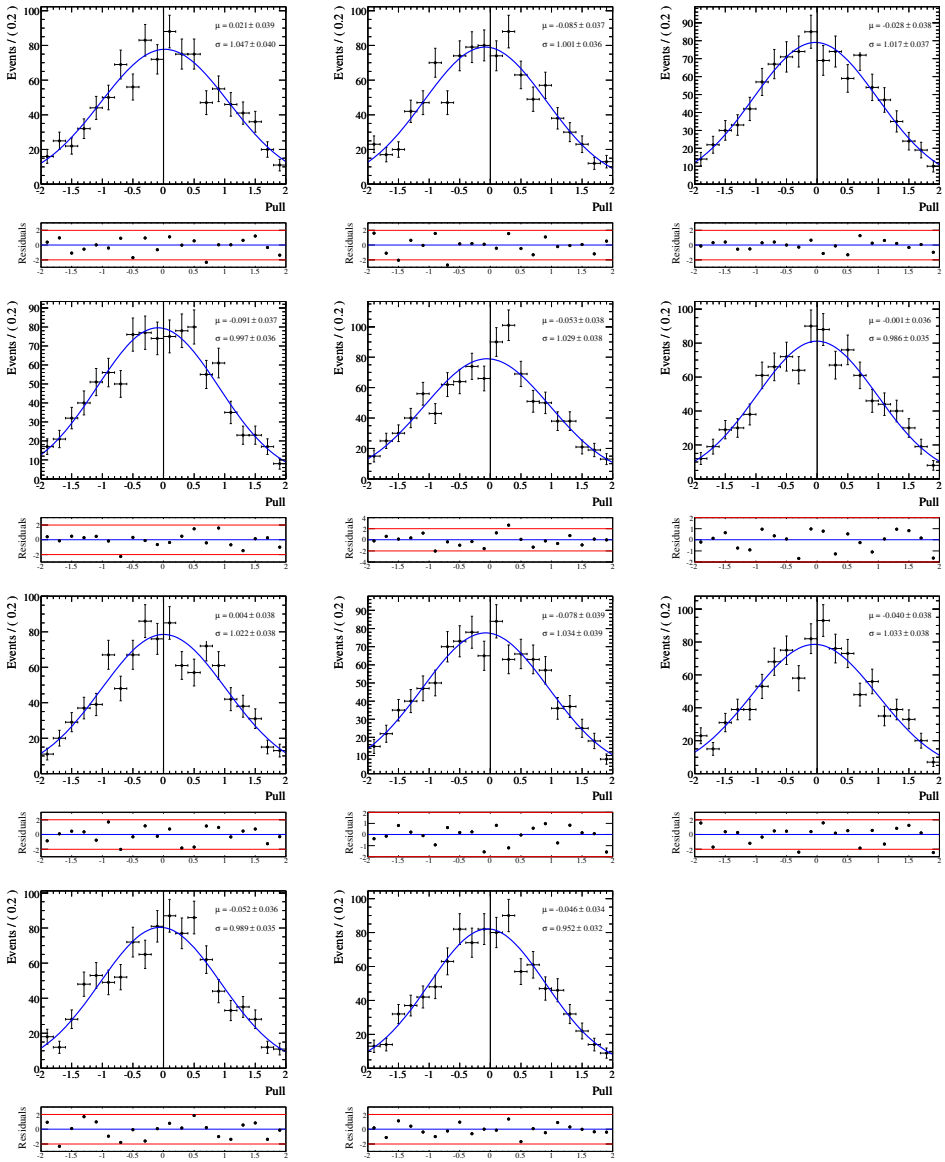

The pull distributions for the $D_s \to \mu\nu_\mu$ mode. The pull distributions for the $D_s \to \mu\nu_\mu$ mode for Monte Carlo samples where the branching fraction $\mathcal{B}(D_s \to \mu\nu_\mu)$ has the values of 75% (first row left), 80% (first row centre), 85% (first row right), 90% (second row left), 95% (second row centre), 100% (second row right), 105% (third row left), 110% (third row centre), 115% (third row right), 120% (fourth row left), and 125% (fourth row centre) of the nominal value of 6.16×10^{-3}.

9.3.4 $D_s \to \ell\nu_\ell$ signal model

The uncertainty associated with the signal model depends on the final state. For the $D_s \to e\nu_e$ and $D_s \to \mu\nu_\mu$ modes the signal model uncertainty is estimated by varying the central value and width of the peak in the signal m_m^2 distribution. To determine how the shape of the signal peak may vary between data and Monte Carlo a control sample of $D_s \to K_S^0 K$ candidates is used. The decay $D_s \to K_S^0 K$ is reconstructed in the following way:

- Reconstructions of the type $e^+e^- \to DKX\gamma D_s$ are selected.
- A $K^{\pm}$ candidate is identified from the `KBDTVeryLoose` selector list.
- A K^0_S candidate is identified by the four-momentum recoiling against the $DKX\gamma K$ system.
- The mass of the K^0_S candidate, $m_{K^0_S}$ must satisfy $m(K^0_S)_{recoil} > 0\,\mathrm{GeVc}^{-2}$.
- The mass of the D_s candidate before a kinematic fit is performed must satisfy $1.868 < m_{D_s} < 2.068\,\mathrm{GeVc}^{-2}$.
- Probability of χ^2 given number of degrees of freedom, n, associated with the kinematic fit to the whole event, $P(\chi^2|n)$, must satisfy $P(\chi^2|n) > 1 \times 10^{-5}$.
- The K candidate cannot overlap with the $DKX\gamma$ system.
- The extra energy in the event must satisfy $E_{extra} < 1\,\mathrm{GeV}$.
- Exactly two tracks from `ChargedTracks` do not overlap with the $DKX\gamma K$ system and they are oppositely charged.

The Monte Carlo samples used for this study includes $c\bar{c}$ and $u\bar{u}/d\bar{d}/s\bar{s}$ Monte Carlo samples weighted to the relevant cross-sections. (Contributions from $B\bar{B}$ and $\tau^+\tau^-$ backgrounds are negligible.) $c\bar{c}$ and $u\bar{u}/d\bar{d}/s\bar{s}$ Monte Carlo samples are taken from Run 1-6 OnPeak and OffPeak collections. The Monte Carlo candidates are not weighted to match the luminosity of the data sample as the study is concerned only with the shape of the m^2_m distribution. Figure 9.3 shows the effects of applying the most discriminating selection criteria sequentially to the control sample in data, indicating the change in yield and shape of the distribution.

The m^2_m distribution for the K^0_S is fitted using a Gaussian probability density function for the signal and a 3rd degree Chebyshev polynomial probability density function for the background. The central values and the standard deviations of the Gaussian probability density functions are compared for Monte Carlo and Data.

The m^2_m distributions for candidates from the K^0_S sample are fit in data and Monte Carlo. The results of these fits are shown in figure 9.4 and the means and standard deviations of the fitted Gaussians are shown in table 9.3.

When comparing the missing mass recoiling against a $DKX\gamma K$ system the difference in between the central values of the peaks is found to be $0.007\,\mathrm{GeV}^2\mathrm{c}^{-4}$ (with the data peaking lower), and the difference of the widths of the peaks is found to be

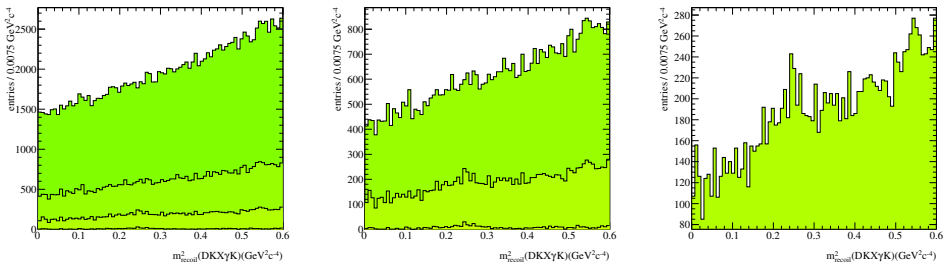

Figure 9.3: The effect of applying selection criteria sequentially to the $D_s \to K^0_S K$ control sample in data. The first histogram shows the distribution after applying the selection criterion $E_{extra} < 1$. The second histogram shows the distribution after applying the selection criterion $|m_{D_s} - 1.968| < 0.1\,\mathrm{GeVc}^{-2}$. The third histogram shows the distribution after applying the selection criterion $P(\chi^2|n) > 1 \times 10^{-5}$.

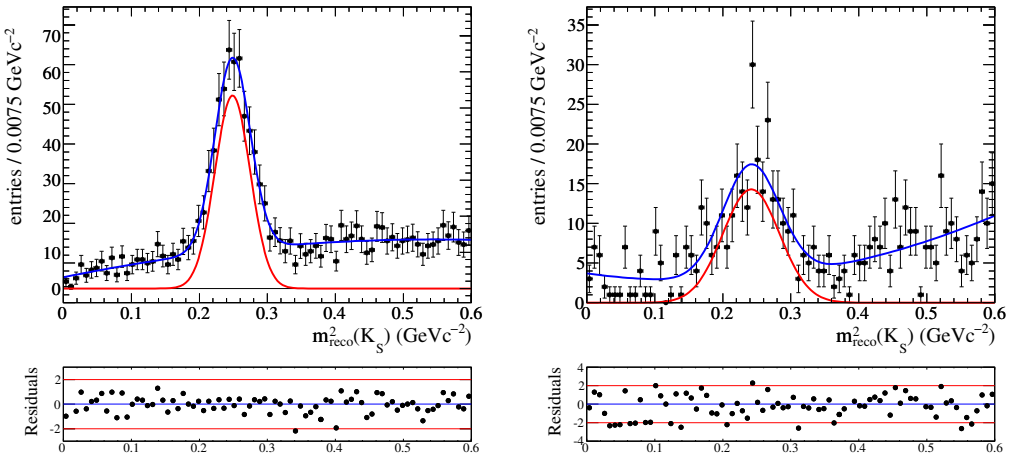

Figure 9.4: The results of the fit to the m^2_m distributions for the $D_s \to K^0_S K$ control sample, for Monte Carlo (left) and data (right).

$0.016\,\mathrm{GeV}^2\mathrm{c}^{-4}$ (with the data having a wider peak). To estimate the uncertainties, two yield extraction fits are performed with different shape parameters.

The width of the signal probability density function is varied by smearing the probability density function in the following way. A Gaussian distribution, G, is defined with mean $0\,\mathrm{GeV}^2\mathrm{c}^{-4}$ and a standard deviation equal to the differences of the width of the peaks taken from the $D_s \to K^0_S K$ study, ($G \sim N(0, 0.1\sigma)$. For each entry in the Signal Monte Carlo, the value of m^2_m is added to a random number generated from G. The residual differences between the raw and smeared m^2_m distributions are shown in figure 9.5.

For the $D_s \to \tau\nu_\tau; \tau \to e\nu_e\nu_\tau$ and $D_s \to \tau\nu_\tau; \tau \to \mu\nu_\mu\nu_\tau$ modes an exponential function is used as the signal probability density function, and the resulting change in yield is taken as the systematic uncertainty. The results of these fits are shown in

Table 9.3: Results of the $D_s \to K^0_S K$ control sample study.

Parameter	Data	Monte Carlo
Mean ($\mathrm{GeV^2c^{-4}}$)	0.242 ± 0.004	0.249 ± 0.002
Standard deviation ($\mathrm{GeV^2c^{-4}}$)	0.249 ± 0.002	0.026 ± 0.001

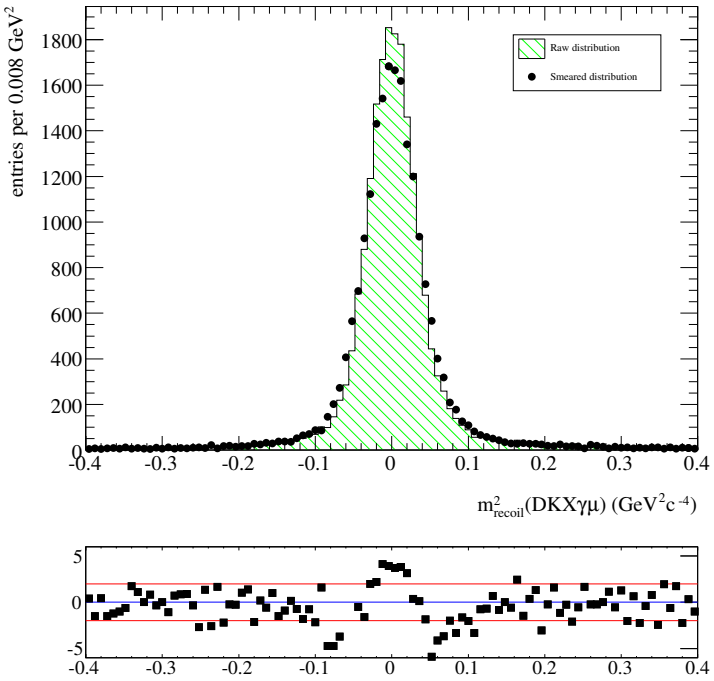

Figure 9.5: The m^2_m distributions and residual differences for signal Monte Carlo before and after smearing for the $D_s \to \mu\nu_\mu$ mode.

figures 9.6 and 9.7. The systematic uncertainties associated with the signal models are 0.4% for the $D_s \to \tau\nu_\tau; \tau \to e\nu_e\nu_\tau$ mode and 9.9% for the $D_s \to \tau\nu_\tau; \tau \to \mu\nu_\mu\nu_\tau$ mode.

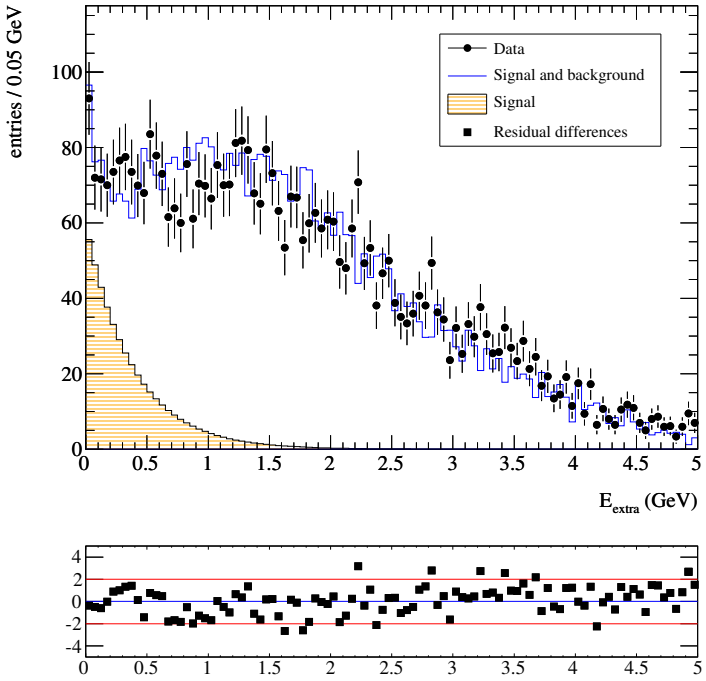

Figure 9.6: The exponential signal probability density function for the $D_s \to \tau\nu_\tau; \tau \to e\nu_e\nu_\tau$ mode.

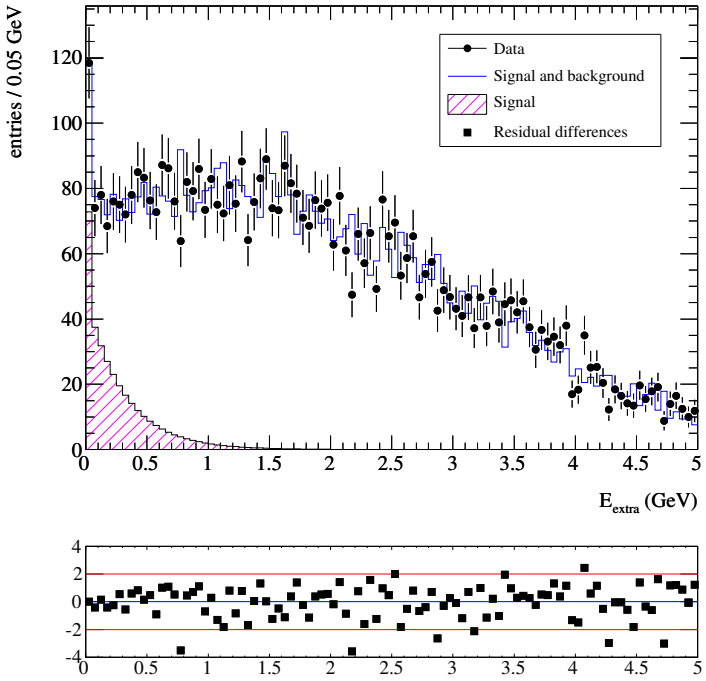

Figure 9.7: The exponential signal probability density function for the $D_s \to \tau\nu_\tau; \tau \to \mu\nu_\mu\nu_\tau$ mode.

9.3.5 $D_s \to \ell\nu_\ell$ background model

There are three contributions to the background model uncertainty. These arise from the uncertainty in the sizes of various components of the background, the D_s decays in the Monte Carlo sample (some of which are now known to be in disagreement with values taken from the Particle Data Group) and from statistical variation due to the small size of the background Monte Carlo sample.

The uncertainty associated with the components background model is estimated by varying the contributions of the components of the background. The following dominant backgrounds are identified and the size of their contribution to the background probability density function varied:

- Semileptonic decays of the D_s meson.
- Hadronic decays of the D_s meson.
- Events where a π^+ is produced in the hadronisation process, and misidentified as a lepton candidate.
- The semileptonic decay of the D^+ meson, $D^+ \to K^0\ell^+\nu$.
- The semileptonic decay of the D^0 meson, $D^0 \to K^-\ell^+\nu$.
- Other background processes arising from $e^+\mathrm{e}^- \to c\bar{c}$ events.
- Other background processes arising from the continuum.

The contributions from leptonic decays are not varied. The backgrounds that do not come from D_s mesons are divided into $c\bar{c}$ events and continuum events to take the uncertainty in the ratio of quark production cross sections into account. The semileptonic decays of the D^0 meson are a large background for high momentum electron candidates, due to misidentification of kaons. The direct production of π^+ mesons is an important background for muon candidates.

The yield of each component is varied by 10% and the yield extraction fit is performed. The differences in the yield when the contribution from the ith component is varied are summed in quadrature:

$$\sigma^2 = \sum_i \left(\frac{N_i^2 - N_{default}}{N_{default}} \right)^2 \tag{9.6}$$

where N_i is the signal yield when the ith component is weighted (by either 90% or 110%, whichever gives the larger change in yield, where the 10% difference is of

Table 9.4: Corrections applied to the Monte Carlo simulation to better model the D_s branching fractions. († this value was obtained by multiplying a Particle Data Group decay with K^0_S in the final state by 2 to obtain the branching fraction with a K^0 in the final state.) (Amsler 2008*b*)

Decay mode	Value in Monte Carlo simulation	Particle Data Group world average
$D_s \to \eta\pi^+$	2.1%	$(1.58 \pm 0.21)\%$
$D_s \to \eta'\pi^+$	4.7%	$(3.8 \pm 0.4)\%$
$D_s \to \omega\pi^+$	0.34%	$(0.25 \pm 0.09)\%$
$D_s \to f_0\pi^+$	1%	$(0.6 \pm 0.24)\%$
$D_s \to f_2\pi^+$	0.23%	$(0.11 \pm 0.06)\%$
$D_s \to \phi\pi^+\pi^-\pi^+$	0.8%	$(1.20 \pm 0.22)\%$
$D_s \to K^0K^\dagger$	4.4%	$(2.98 \pm 0.18)\%$
$D_s \to K^{\star 0}K^\dagger$	4.0%	$(5.2 \pm 0.8)\%$
$D_s \to K^0K^+\pi^+\pi^{-\dagger}$	0.1%	$(1.92 \pm 0.26)\%$
$D_s \to K^+K^-\pi^+\pi^-\pi^+$	0.43%	$(0.09 \pm 0.07)\%$
$D_s \to \eta K^+$	0.02%	$(0.141 \pm 0.031)\%$
$D_s \to \eta' K^+$	0.02%	$(0.16 \pm 0.05)\%$
$D_s \to K^+K^-K^+$	0.02%	$(0.049 \pm 0.017)\%$
$D_s \to K^{\star 0}\pi^{+\dagger}$	0.79%	$(0.30 \pm 0.052)\%$

the order of magnitude of the uncertainties stated by the Particle Data Group) and $N_{default}$ is the signal yield when all the components are weighted by 100%.

The branching fractions in the Monte Carlo simulation are known to not match the most up to date measurements provided by the Particle Data Group. To estimate the uncertainty this introduces the Monte Carlo events are reweighted where a D_s is present and where the D_s decay is known to be in disagreement with the Particle Data Group world average by at least one standard deviation. The list of decays and their corrections is outlined in table 9.4. The difference is given by the difference of the branching fractions divided by the uncertainty provided in the Particle Data Group. Only differences in excess of (equal to) 1σ are reported. Events with leptonic decays are not corrected. The sum of branching fractions in the Monte Carlo simulation is 99.996% and in the Particle Data Group is $(94.7^{+5.3}_{-17.5})\%$, where the upper uncertainty has been constrained such that the sum of the branching fractions do not exceed 100%.

The uncertainty due to the statistical limitations of the generic Monte Carlo is

Table 9.5: Uncertainties associated with selection criteria.

Decay mode	Statistical uncertainty	Variational uncertainty	Total uncertainty
$D_s \to e\nu_e$	0.3%	2.5%	2.5%
$D_s \to \mu\nu_\mu$	0.1%	1.8%	1.8%
$D_s \to \tau\nu_\tau; \tau \to e\nu_e\nu_\tau$	0.2%	2.8%	2.8%
$D_s \to \tau\nu_\tau; \tau \to \mu\nu_\mu\nu_\tau$	0.1%	2.0%	2.0%

estimated by propagating the statistical uncertainties through during the yield extraction fit which minimises the χ^2/n of the fit, and comparing this to the result where these uncertainties are not propagated.

9.3.6 Selection criteria

For the $D_s \to \mu\nu_\mu$, $D_s \to \tau\nu_\tau; \tau \to e\nu_e\nu_\tau$ and $D_s \to \tau\nu_\tau; \tau \to \mu\nu_\mu\nu_\tau$ modes reconstructions are required to satisfy $E_{extra} < 1\text{GeV}$. The uncertainties on the efficiencies of this criterion are estimated by varying the size of the selection region by 10% and determining the changes in the efficiencies. 100 MeV in the E_{extra} variable corresponds to the addition or omission of three clusters in the electromagnetic calorimeter. $0.5\,\text{GeV}^2\text{c}^{-4}$ in the m_m^2 variable accounts for a mis-modelling of the radiative tail in the m_m^2 spectrum. The particle identification is applied to the samples before the uncertainty are estimated and the uncertainty has two components associated with it. The first component arises from the statistical limitations of the Monte Carlo sample. The second component arises from the change in the efficiency. These uncertainties are added in quadrature.

The statistical uncertainty is simply the binomial error associated with the selection criterion, $\epsilon_{stat} = \sqrt{\varepsilon(1-\varepsilon)/n}$, where ε is the efficiency of the selection criterion and n is the number of entries in the Monte Carlo distribution. The uncertainty associated with the variation of the selection criterion, ϵ_{var}, is given by the relative change in efficiency: $\epsilon_{var} = (\varepsilon_{varied} - \varepsilon_{central})/\varepsilon_{central} = \Delta\varepsilon/\varepsilon$.

The uncertainties of the selection criteria are shown in table 9.5. Figures 9.9-9.11 show the selection criteria, and the legend is provided again in figure 9.8.

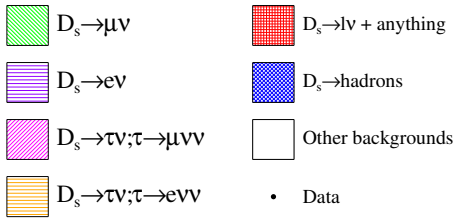

Figure 9.8: Legend for the background components for the $D_s \to \ell\nu_\ell$ reconstruction.

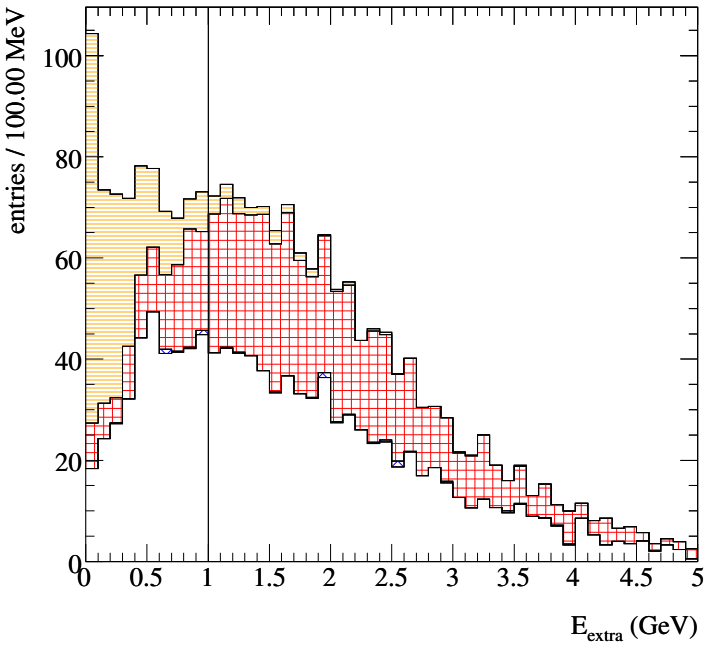

Figure 9.9: E_{extra} selection criterion for the $D_s \to e\nu_e$ mode. ($E_{extra} < 1\,\mathrm{GeV}$)

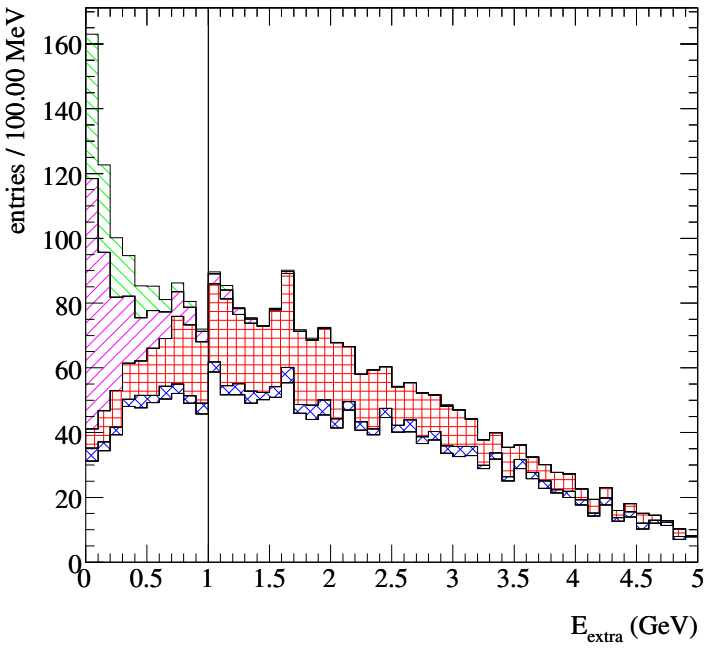

Figure 9.10: E_{extra} selection criterion for the $D_s \to \mu\nu_\mu$ mode. ($E_{extra} < 1\,\mathrm{GeV}$) Note: Aside from the vertical line marking the selecion criteria, this plot is identical to the plot shown in figure 8.17.

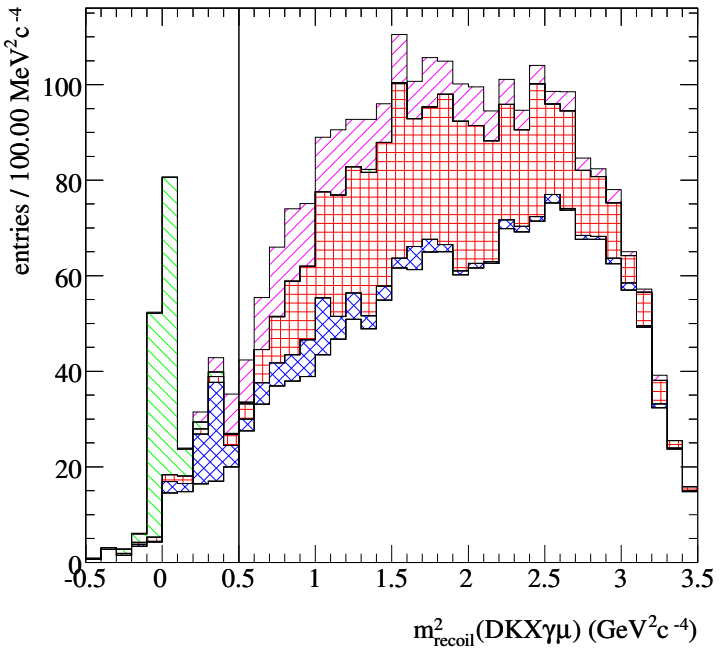

Figure 9.11: m_m^2 selection criterion for the $D_s \to \tau\nu_\tau; \tau \to \mu\nu_\mu\nu_\tau$ mode. ($m_m^2 > 0.5\,\mathrm{GeV}^2\mathrm{c}^{-4}$)

9.4 Total systematic uncertainties

The systematic uncertainties for each mode are outlined in table 9.6. For the $D_s \to e\nu_e$ mode the quoted uncertainties for the $D_s \to e\nu_e$ signal and background models are the absolute uncertainties in terms of numbers of reconstructions. The total uncertainty for this mode is not quoted at this stage, as the upper limit estimation depends upon both relative and absolute uncertainties which cannot be summed in quadrature. For all other modes the quoted uncertainties are relative uncertainties. For the $D_s \to e\nu_e$ mode the dominant sources of systematic uncertainties appear to arise from the estimate of the yield of D_s mesons. For the $D_s \to \mu\nu_\mu$ mode the systematic uncertainties show a fair range of contributions, with no single contribution dominating the uncertainty. For the $D_s \to \tau\nu_\tau$ modes the dominant sources of uncertainty arise from the signal and background probability density functions used to estimate the yield of $D_s \to \tau\nu_\tau$ events. This is understood when the variable E_{extra} is considered in more detail. The processes which lead to depositions of extra energy in the electromagnetic calorimeter (including beam-gas interactions, Bhabha scattering, radiative decays, electronic noise and Bremsstrahlung radiation) are poorly understood and poorly modelled. As a result the Monte Carlo samples can only provide a fair description of the data.

Table 9.6: Summary of systematic uncertainties for each mode. (For the $D_s \to e\nu_e$ mode some of the uncertainties are quoted as absolute errors and used in the estimation of an upper limit.)

Source of uncertainty	Contribution to uncertainty for $D_s \to e\nu_e$	$D_s \to \mu\nu_\mu$	$D_s \to \tau\nu_\tau$ $(\tau \to e\nu_e\nu_\tau)$	$D_s \to \tau\nu_\tau$ $(\tau \to \mu\nu_\mu\nu_\tau)$
Right sign/wrong sign components	0.99%	0.99%	0.99%	0.99%
D_s signal model	1.55%	1.55%	1.55%	1.55%
D_s background model	0.05%	0.05%	0.05%	0.05%
D_s peaking backgrounds	2.08%	2.08%	2.08%	2.08%
X crossfeed	1.74%	1.74%	1.74%	1.74%
Signal photon	2.46%	2.46%	2.46%	2.46%
Track reconstruction	0.83%	0.83%	0.83%	0.83%
Particle identification	0.16%	1.86%	0.16%	1.88%
$D_s \to \ell\nu_\ell$ signal model	3.97	1.92%	9.93%	0.39%
$D_s \to \ell\nu_\ell$ background model	0.82	2.21%	8.31%	9.34%
$D_s \to \ell\nu_\ell$ selection criteria	2.48%	0.13%	0.02%	1.74%
Total	–	5.43%	13.60%	10.56%

Table 9.7: Uncertainties associated with the masses of the particles relevant to this thesis. (Amsler 2008*b*)

Particle	Mass (GeVc^{-2})
m_{D_s}	1.96849(34)
m_e	0.000510998910(13)
m_μ	0.105658367(4)
m_τ	1.77684(17)

9.5 Theoretical uncertainties on physical constants

The expression for f_{D_s} in terms of the branching fraction $\mathcal{B}(D_s \to \ell\nu_\ell)$ is given by equation 3.1. Inverting this equation gives

$$f_{D_s^+} = \frac{1}{G_F m_\ell \left(1 - \frac{m_\ell^2}{M^2_{D_s^+}}\right) |V_{cs}|} \sqrt{\frac{8\pi B(D_s^+ \to \ell\nu)}{M_{D_s^+}\tau_{D_s^+}}} \tag{9.7}$$

where the physical constants have their usual meanings. The uncertainty introduced by using physical constants are quoted separately, as future experiments are likely to improve the precision of these constants, thereby increasing the precision of the estimation of f_{D_s}.

9.5.1 D_s meson lifetime, τ_{D_s}

The lifetime of the D_s meson contributes the most significant source of uncertainty of all the physical constants. Current estimates give $\tau_{D_s} = (500 \pm 7) \times 10^{-15}\,\mathrm{s}$ (Amsler 2008*b*).

9.5.2 Particle masses

The uncertainties associated with the particle masses are listed in table 9.7. These are found to be negligible when compared to other uncertainties.

9.5.3 Cabibbo-Kobayashi-Maskawa element, $|V_{cs}|$

For this analysis unitarity in the light quark sector is assumed, so that $|V_{cs}| = |V_{ud}| = 0.97418(27)$ is used (Amsler 2008*b*). This improves the precision of the constant

substantially and as outlined in section 2.7 it is a reasonable assumption to adopt (up to the fourth power of the Wolfenstein parameter, λ).

It should be noted that if unitarity is not respected in decays of mesons then this violation of unitarity cannot account for the difference between experiment and theory. If the value of V_{cs} is responsible for the difference then the value would have to satisfy $|V_{cs}| > 1$, which is not internally consistent with the definition of the unitary matrix, V. (If $|V_{cs}|$ happens to be smaller than unity then a violation of unitarity would indicate new physics beyond the Standard Model. However, a value of $|V_{cs}|$ greater than unity indicates a probability greater than 1 for some processes.)

The `CKMFitter` group provide an estimate of $|V_{cs}|$ which appears to be as precise as the estimate of $|V_{ud}|$ provided by the Particle Data Group. However this estimate cannot be used as it is determined using a global fit for which previous measurements of $\mathcal{B}(D_s \to \ell\nu_\ell)$ are used to constrain the Cabibbo-Kobayashi-Maskawa matrix elements.

9.5.4 Fermi coupling constant, G_F

The Fermi coupling constant, G_F, is currently estimated to be $G_F = 1.16637(1)\times10^{-5}$ (Amsler 2008*b*).

9.5.5 Total uncertainty

The total uncertainties introduced by these physical constants are outlined in table 9.8. The most dominant source of systematic uncertainty arises from the uncertainty on the lifetime of the D_s meson. As this uncertainty may be decreased by later experiments the theoretical uncertainties are quoted separately.

9.6 Summary

There are many sources of systematic uncertainty associated with the branching fraction calculations. Many of these uncertainties cancel out exactly when the ratio of yields is taken. Therefore this thesis presents only the systematic uncertainties which contribute to the overall ratio. The systematic uncertainties presented concern the yields of the D_s mesons and $D_s \to \ell\nu_\ell$ events, as well as the uncertainties needed to estimate the value of f_{D_s}.

Table 9.8: Uncertainties associated with the physical constants. The uncertainties are the relative uncertainties on the value of f_{D_s}. (Amsler 2008*b*)

	Contribution to uncertainty for			
Constant	$D_s \to e\nu_e$	$D_s \to \mu\nu_\mu$	$D_s \to \tau\nu_\tau$ ($\tau \to e\nu_e\nu_\tau$)	$D_s \to \tau\nu_\tau$ ($\tau \to \mu\nu_\mu\nu_\tau$)
τ_{D_s}	7×10^{-3}	7×10^{-3}	7×10^{-3}	7×10^{-3}
m_{D_s}	4.3×10^{-4}	4.3×10^{-4}	4.3×10^{-4}	4.3×10^{-4}
m_e	7.6×10^{-8}	-	-	-
m_μ	-	2.6×10^{-7}	-	-
m_τ	-	-	2.9×10^{-4}	2.9×10^{-4}
$\lvert V_{cs}\rvert$	2.8×10^{-4}	2.8×10^{-4}	2.8×10^{-4}	2.8×10^{-4}
G_F	8.6×10^{-6}	8.6×10^{-6}	8.6×10^{-6}	8.6×10^{-6}
Total	7.0×10^{-3}	7.0×10^{-3}	7.0×10^{-3}	7.0×10^{-3}

Chapter 10

Results

10.1 Overview

With the measurements of the branching fractions complete it is necessary to extract several values of interest. The results are outlined for each mode separately, with values of f_{D_s} estimated for each non-zero branching fraction. The results are also combined, where appropriate, to reduce uncertainties.

10.2 Limit of $\mathcal{B}(D_s \to e\nu_e)$

The Standard Model expectation for the value of $\mathcal{B}(D_s \to e\nu_e)$ is so small that no observation of signal events is expected in the BaBar data set. A maximum likelihood analysis is performed to determine the most likely probability density function for $\mathcal{B}(D_s \to e\nu_e)$, which is then integrated to obtain a 90% confidence limit on the branching fraction.

The total relative efficiency, $\bar{\varepsilon}$, is a function of the relative efficiencies for each value of n_X^T and the relevant weights, w_j:

$$\bar{\varepsilon}(\beta,\gamma) = \frac{\sum_j w_j(\beta,\gamma)\varepsilon_j}{\sum_k w_k} \tag{10.1}$$

where $w_j(\beta,\gamma) = (j-\alpha)^\beta e^{-\gamma j} / \sum_k (k-a)^\beta e^{-\gamma k}$, and $\sum_k w_k = 1$ by construction. The uncertainty for the efficiency for a given value of n_X^T is determined using Monte Carlo samples, and is the Gaussian error ($\sqrt{1/N_j}$, where N_j is the number of $D_s \to e\nu_e$ events in the sample.)

The expected number of events in the data sample is given by

$$\mu = BN_{D_s}\bar{\varepsilon} \tag{10.2}$$

where B is the branching fraction $\mathcal{B}(D_s \to e\nu_e)$.

To estimate the upper limit on the branching fraction a likelihood function is defined in terms of the product of the number of the D_s mesons and the signal efficiency, $\lambda = N_{D_s} \times \bar{\varepsilon}$, and the branching fraction, B. (The product $N_{D_s}\bar{\varepsilon}$ must be taken as the uncertainties on the estimates of these numbers are correlated as they are both determined from the D_s yield extraction fit):

$$\mathcal{L}(B, \lambda; n, \hat{\lambda}) = exp\left(-\frac{(\mu - n)^2}{2\sigma_n^2} e^{-\frac{(\lambda-\hat{\lambda})^2}{2\sigma_{\hat{\lambda}}^2}}\right) \tag{10.3}$$

where $\hat{\lambda}$ is the estimation of the λ, σ_λ is the uncertainty of this estimation, μ is the true number of $D_s \to e\nu_e$ events in the data sample, n is the yield of $D_s \to e\nu_e$ events returned by the fit, and σ_n is the statistical error on this number. This likelihood function assumes uniform prior distributions in the unknown parameters.

The uncertainty for λ, is

$$\sigma_\lambda^2 = \sum_{a,b} \frac{\partial\lambda}{\partial x_a}\frac{\partial\lambda}{\partial x_b} V_{ab} \tag{10.4}$$

where V_{ab} is the covariance matrix element for the parameters a and b, and $V_{ab}^2 = \rho(a,b)\sigma_a\sigma_b$, where $\rho(a,b)$ is the correlation between a and b, and σ_a and σ_b are the uncertainties on these parameters. Variation in α is not included in this expression because the fit is found to be insensitive to this parameter, as discussed in section 9.2.1. The derivatives are

$$\frac{\partial\lambda}{\partial N_{D_s}} = \frac{\lambda}{N_{D_s}} \tag{10.5}$$

$$\frac{\partial\lambda}{\partial\varepsilon_j} = N_{D_s} w_j \tag{10.6}$$

$$\frac{\partial\lambda}{\partial\beta} = \lambda\frac{\sum_j w_j\varepsilon_j \ln(j-\alpha)}{\sum_k w_k\varepsilon_k} \tag{10.7}$$

$$\frac{\partial\lambda}{\partial\gamma} = \lambda\frac{\sum_j w_j\varepsilon_j j}{\sum_k w_k\varepsilon_k} \tag{10.8}$$

The yield of D_s mesons obtained from section 8.2.3 is $67,000$ and the total relative

efficiency is 0.71. The value of λ is

$$\lambda = 47,362 \pm 2,832 \tag{10.9}$$

and the contributions to the uncertainties are outlined in table 10.1.

Table 10.1: Summary of the sources of systematic uncertainties for $\hat{\lambda}$.

Source of uncertainty	Absolute contribution to uncertainty	Relative contribution to uncertainty
Right sign/wrong sign components	1611	3.40%
D_s signal model	696	1.47%
D_s background model	355	0.75%
D_s peaking backgrounds	674	1.42%
X crossfeed	993	2.10%
Signal photon	1081	2.28%
Track reconstruction	372	0.83%
Particle identification	63	0.16%
$D_s \to \ell\nu_\ell$ selection criteria	1170	2.47%
D_s Statistical uncertainty	832	1.76%
Total	2832	5.98%

The value of σ_n is determined by adding the statistical uncertainty and the uncertainties due to the $D_s \to e\nu_e$ signal and background models in quadrature. These contributions are outlined in table 10.2.

Table 10.2: Summary of the sources of uncertainties for n.

Source of uncertainty	Contribution to uncertainty
Statistical uncertainty of fit	1.87
Background model uncertainty	0.16
Signal model uncertainty	2.78
Total	3.35

This likelihood function is then integrated over the parameter, λ, in order to obtain a likelihood function in terms of just B:

$$\mathcal{L}(B; n, \hat{\lambda}) = \int \mathcal{L}(B, \lambda; n, \hat{\lambda}) \mathrm{d}\lambda \tag{10.10}$$

The 90% confidence interval is found using the ratio of integrals:

$$90\% = \frac{\int_0^{B_{CI}} \mathcal{L}(B; n, \hat{\lambda}) \mathrm{d}B}{\int_0^1 \mathcal{L}(B; n, \hat{\lambda}) \mathrm{d}B} \tag{10.11}$$

where B_{CI} is the branching fraction at the 90% confidence interval. σ_n is the sum in quadrature of the absolute statistical and systematic uncertainties.

This integration is performed using a Monte Carlo method with 1×10^8 iterations. A three dimensional space is defined in terms of $\mathcal{L}(B, \lambda; n, \hat{\lambda})$, B, and λ within the limits $0 < \mathcal{L}(B, \lambda; n, \hat{\lambda}) < 1$, $\hat{\lambda} - 5\sigma_\lambda < \lambda < \hat{\lambda} + 5\sigma_\lambda$, and $0 < B < 5 \times 10^{-5}$. A point, $p_i = (L_i, \lambda_i, B_i)$, is randomly generated by taking coordinates from random uniform distributions in each dimension. The integral is incremented by 1 if $L_i < \mathcal{L}(B, \lambda; n, \hat{\lambda})$. The resulting likelihood function is shown in figure 10.1. The method outlined is stable as the fitted yield is fractional or negative.

Using $\hat{\lambda} = 47,362$, $\sigma_\lambda = 2,832$, $n = 1.94$, and $\sigma_n = 3.35$ the upper limit in Monte Carlo is estimated as $\mathcal{B}(D_s \to e\nu_e) < 1.46 \times 10^{-4}$. Using the Particle Data Group world average for $\mathcal{B}(D_s \to \mu\nu_\mu) = (6.3 \pm 0.5) \times 10^{-3}$ (Amsler 2008*b*) and noting that according the Standard Model the ratio of branching fractions is

$$\frac{\mathcal{B}(D_s \to e\nu_e)}{\mathcal{B}(D_s \to \mu\nu_\mu)} = \frac{m_e^2 \left(M_{D_s}^2 - m_e^2\right)^2}{m_\mu^2 \left(M_{D_s}^2 - m_\mu^2\right)^2} \tag{10.12}$$

(where m_e is the mass of the electron, m_μ is the mass of the muon, and M_{D_s} is the mass of the D_s meson) the estimate for the branching fraction is $\mathcal{B}(D_s \to e\nu_e) = (1.5 \pm 0.1) \times 10^{-7}$, where uncertainties on the masses of the particles has been ignored. The result for $\mathcal{B}(D_s \to e\nu_e)$ presented in this work is consistent with the Standard Model expectation, based on the world average value for $\mathcal{B}(D_s \to \mu\nu_\mu)$.

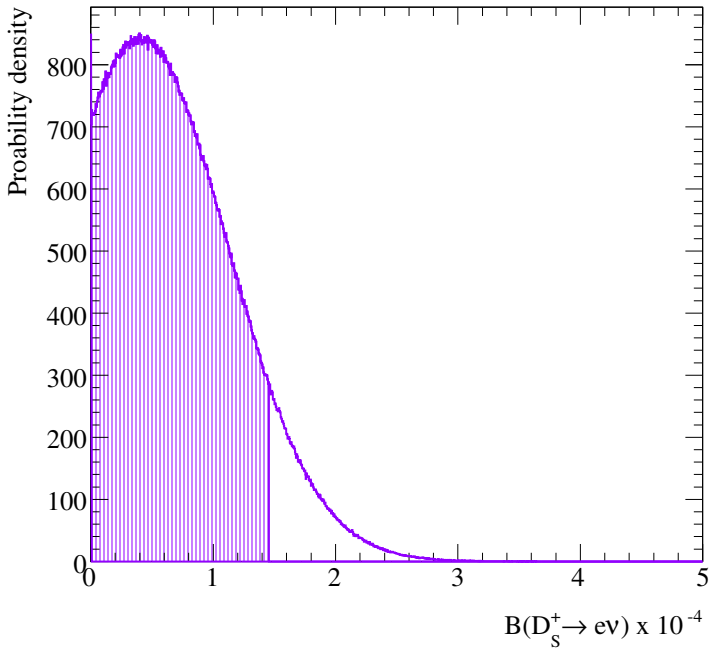

Figure 10.1: The 90% confidence interval for an upper limit on the branching fraction, if no signal candidates are observed. The plots show the likelihood function as a function of the branching fraction, B, in arbitary units. The shaded region encloses 90% of the cumulative likelihood function.

10.3 Measurements of $\mathcal{B}(D_s \to \mu\nu_\mu)$, and $\mathcal{B}(D_s \to \tau\nu_\tau)$

The values of $\mathcal{B}(D_s \to \mu\nu_\mu)$, $\mathcal{B}(D_s \to \tau\nu_\tau; \tau \to e\nu_e\nu_\tau)$ and $\mathcal{B}(D_s \to \tau\nu_\tau; \tau \to \mu\nu_\mu\nu_\tau)$ are found by taking the ratios of efficiency corrected $D_s \to \ell\nu_\ell$ and inclusive D_s yields. The efficiencies are determined for each value of n_X^T using Monte Carlo samples and the overall efficiencies are then the weighted average of these efficiencies, as described in equation 8.6. To obtain the value of $\mathcal{B}(D_s \to \tau\nu_\tau)$, the ratios of branching fractions are taken:

$$\mathcal{B}(D_s \to \tau\nu_\tau) = \frac{\mathcal{B}(D_s \to \tau\nu_\tau; \tau \to \ell\nu_\ell\nu_\tau)}{\mathcal{B}(\tau \to \ell\nu_\ell\nu_\tau)} \tag{10.13}$$

10.3.1 $\mathcal{B}(D_s \to \tau\nu_\tau)$

The value of $\mathcal{B}(D_s \to \tau\nu_\tau)$ can be estimated by combining the measurements of $\mathcal{B}(D_s \to \tau\nu_\tau; \tau \to \mu\nu_\mu\nu_\tau)$ and $\mathcal{B}(D_s \to \tau\nu_\tau; \tau \to \mu\nu_\mu\nu_\tau)$. The uncertainties due to the denominator are common to both measurements, so they are only added once. The uncertainties due to the numerator are weighted and added in quadrature. The expression for the branching fraction is:

$$\begin{aligned} \mathcal{B}(D_s \to \tau\nu_\tau) \quad = \quad & \frac{N_\mu}{N_\mu + N_e} \frac{\mathcal{B}(D_s \to \tau\nu_\tau; \tau \to \mu\nu_\mu\nu_\tau)}{\mathcal{B}(\tau \to \mu\nu_\mu\nu_\tau)} \\ & + \frac{N_e}{N_\mu + N_e} \frac{\mathcal{B}(D_s \to \tau\nu_\tau; \tau \to e\nu_e\nu_\tau)}{\mathcal{B}(\tau \to e\nu_e\nu_\tau)} \end{aligned} \tag{10.14}$$

where N_μ is the number of $D_s \to \tau\nu_\tau; \tau \to \mu\nu_\mu\nu_\tau$ events and N_e is the number of $D_s \to \tau\nu_\tau; \tau \to e\nu_e\nu_\tau$ events.

The uncertainty is:

$$\sigma(D_s \to \tau\nu_\tau)^2 = \left(\frac{N_\mu}{N_\mu + N_e+}\right)^2 \sigma_\mu^2 + \left(\frac{N_e}{N_\mu + N_e}\right)^2 \sigma_e^2 + \sigma_D^2 \tag{10.15}$$

where σ_μ is the uncertainty from the $D_s \to \tau\nu_\tau; \tau \to \mu\nu_\mu\nu_\tau$ mode, σ_e is the uncertainty from the $D_s \to \tau\nu_\tau; \tau \to e\nu_e\nu_\tau$ mode and σ_D is the uncertainty from the denominator.

The measurements of the branching fraction for the processes $\mathcal{B}(D_s \to \ell\nu_\ell)$ with the statistical and systematic uncertainties are outlined in table 10.3.

Table 10.3: Summary of results (or limits, where appropriate) for $\mathcal{B}(D_s \to \ell\nu_\ell)$ decays, including statistical and systematic uncertainties. Where given, the first uncertainty is statistical and the second uncertainty is systematic.

Decay	$\mathcal{B}(D_s \to \ell\nu_\ell)$	Yield
$D_s \to e\nu_e$	$< 1.46 \times 10^{-4}$	1.94
$D_s \to \mu\nu_\mu$	$(6.11 \pm 0.38 \pm 0.33) \times 10^{-3}$	274.1
$D_s \to \tau\nu_\tau(\tau \to e\nu_e\nu_\tau)$	$(5.38 \pm 0.51 \pm 0.57) \times 10^{-2}$	433.4
$D_s \to \tau\nu_\tau(\tau \to \mu\nu_\mu\nu_\tau)$	$(4.82 \pm 0.46 \pm 0.66) \times 10^{-2}$	334.1
$D_s \to \tau\nu_\tau$ combined	$(5.06 \pm 0.34 \pm 0.50) \times 10^{-2}$	767.5

10.4 Calculation of f_{D_s}

The value of f_{D_s} is determined using the expression for the branching fraction as outlined in equation 3.1. Inverting this equation and noting that $\mathcal{B}(D_s \to \ell\nu_\ell) = \tau_{D_s^+}\Gamma(D_s \to \ell\nu_\ell)$, where $\Gamma(D_s \to \ell\nu_\ell)$ is the partial width of the decay $D_s \to \ell\nu_\ell$ gives

$$f_{D_s^+} = \frac{1}{G_F m_\ell \left(1 - \frac{m_\ell^2}{M^2_{D_s^+}}\right) |V_{cs}|} \sqrt{\frac{8\pi\mathcal{B}(D_s \to \ell\nu_\ell)}{M_{D_s^+}\tau_{D_s^+}}} \tag{10.16}$$

where the terms have the usual meanings, defined previously. The values of f_{D_s} determined from the decays $D_s \to \tau\nu_\tau; \tau \to e\nu_e\nu_\tau$ and $D_s \to \tau\nu_\tau; \tau \to \mu\nu_\mu\nu_\tau$ can be combined to provide a single value of f_{D_s} for $D_s \to \tau\nu_\tau$, where $\mathcal{B}(D_s \to \tau\nu_\tau)$ is taken from equation 10.14. The calculations for the values of f_{D_s} are given in table 10.4.

Table 10.4: Summary of results for f_{D_s} for non-zero branching fraction decays, including statistical, systematic and theoretical uncertainties. Where given, the first uncertainty is the statistical uncertainty, the second uncertainty is the systematic uncertainty and the third uncertainty is the theoretical uncertainty.

Decay	f_{D_s}
$D_s \to \mu\nu_\mu$	$(267.7 \pm 8.3 \pm 7.2 \pm 1.9)$ MeV
$D_s \to \tau\nu_\tau; \tau \to e\nu_e\nu_\tau$	$(254.4 \pm 12.1 \pm 13.5 \pm 1.8)$ MeV
$D_s \to \tau\nu_\tau; \tau \to \mu\nu_\mu\nu_\tau$	$(240.8 \pm 8.5 \pm 12.5 \pm 1.7)$ MeV
$D_s \to \tau\nu_\tau$ combined	$(246.7 \pm 8.3 \pm 12.2 \pm 1.7)$ MeV

10.5 Combined results for $D_s \to \ell\nu_\ell$

The results for the values of f_{D_s} can be combined to provide a single estimate for the parameter, assuming no effects beyond the Standard Model. The combined result is

$$f_{D_s} = \frac{N_\mu}{N_\mu + N_\tau} f_{D_s}(D_s \to \mu\nu_\mu) + \frac{N_\tau}{N_\mu + N_\tau} f_{D_s}(D_s \to \tau\nu_\tau) \tag{10.17}$$

where N_μ is the number of $D_s \to \mu\nu_\mu$ events and N_τ is the number of $D_s \to \tau\nu_\tau$ events.

The uncertainty is:

$$\sigma(f_{D_s})^2 = \left(\frac{N_\mu}{N_\mu + N_\tau +}\right)^2 \sigma^2_{f_{D_s}(D_s \to \mu\nu_\mu)} + \left(\frac{N_\tau}{N_\mu + N_e\tau}\right)^2 \sigma^2_{f_{D_s}(D_s \to \tau\nu_\tau)} \tag{10.18}$$

This gives the value of f_{D_s} to be

$$f_{D_s} = 252.2 \pm 5.7 \pm 7.0 \pm 1.0\,\text{MeV} \tag{10.19}$$

where the first uncertainty is statistical, the second uncertainty is systematic and the third uncertainty is theoretical (assuming only Standard Model processes contribute to the leptonic decays of the D_s meson.) The results for f_{D_s} are shown in figure 10.2.

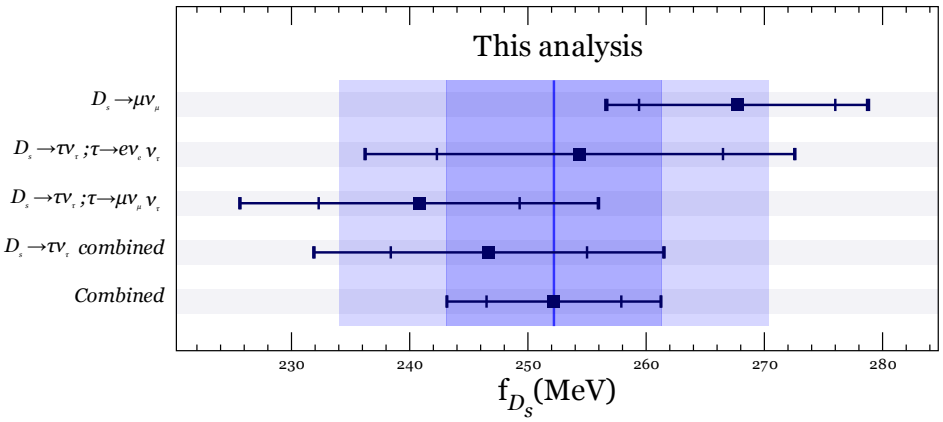

Figure 10.2: Summary of results for f_{D_s} for the $D_s \to \mu\nu_\mu$, $D_s \to \tau\nu_\tau; \tau \to e\nu_e\nu_\tau$, $D_s \to \tau\nu_\tau; \tau \to \mu\nu_\mu\nu_\tau$ modes, and their averages.

10.6 Summary

The estimation of $D_s \to e\nu_e$ returns an upper limit, with a sensitivity comparable to the world average. The $D_s \to \mu\nu_\mu$, $D_s \to \tau\nu_\tau; \tau \to e\nu_e\nu_\tau$, and $D_s \to \tau\nu_\tau; \tau \to \mu\nu_\mu\nu_\tau$ modes return branching fractions consistent with previous results. The results presented here show an average value of f_{D_s}, which is lower than the current world average, and may reconcile the perceived discrepancy between experimental results and unquenched lattice chromodynamical expectations. The results for the branching fractions and f_{D_s} are given for each mode separately and combined, as physics beyond the Standard Model may affect different final states to different degrees. The results show no evidence of such effects.

Chapter 11

Conclusion

This thesis has provided three new measurements of branching fractions of leptonic decays of the D_s meson, and an upper limit on the branching $\mathcal{B}(D_s \to e\nu_e)$. The measurement of $\mathcal{B}(D_s \to \tau\nu_\tau; \tau \to \mu\nu_\mu\nu_\tau)$ is the first such measurement since 2000 (Alexandrov 2000).

11.1 Test of lepton universality

According to the Standard Model, the ratio of the branching fractions $\mathcal{B}(D_s \to \mu\nu_\mu)$ and $D_s \to \tau\nu_\tau$ should have a well known value. Using equation 3.1:

$$
\begin{aligned}
R_{SM} &= \frac{\mathcal{B}(D_s \to \mu\nu_\mu)}{\mathcal{B}(D_s \to \tau\nu_\tau)} && (11.1)\\
&= \frac{\frac{m_{D_s}}{8\pi} f_{D_s}^2 G_F^2 |V_{cs}|^2 m_\mu^2 \left(1 - \frac{m_\mu^2}{m_{D_s}^2}\right)^2}{\frac{m_{D_s}}{8\pi} f_{D_s}^2 G_F^2 |V_{cs'}|^2 m_\tau^2 \left(1 - \frac{m_\tau^2}{m_{D_s}^2}\right)^2} && (11.2)\\
&= \frac{m_\mu^2 \left(1 - \frac{m_\mu^2}{m_{D_s}^2}\right)^2}{m_\tau^2 \left(1 - \frac{m_\tau^2}{m_{D_s}^2}\right)^2} && (11.3)\\
&= 0.10 && (11.4)
\end{aligned}
$$

Using the values $\mathcal{B}(D_s \to \mu\nu_\mu) = (6.11 \pm 0.38 \pm 0.33) \times 10^{-3}$ and $\mathcal{B}(D_s \to \tau\nu_\tau) = (5.06 \pm 0.34 \pm 0.50) \times 10^{-3}$ one obtains the ratio, R:

$$R = 0.12 \pm 0.01 \pm 0.01 \qquad (11.5)$$

which is consistent with R_{SM}, indicating no evidence of lepton universality violation.

This result can be used to constrain models of physics beyond the Standard Model (Doršner 2009).

11.2 Current global experimental sensitivity

Figure 11.1 compares the sensitivities of various experiments from around the world for the values of f_{D_s} to the work presented in this thesis. The figure shows that the combined result presented in this thesis is more sensitive than any other current measurement.

Figures 11.2-11.5 compare the sensitivities of various experiments from around the world for the branching fractions $\mathcal{B}(D_s \to \ell\nu_\ell)$ to the work presented in this thesis, on a per mode basis.

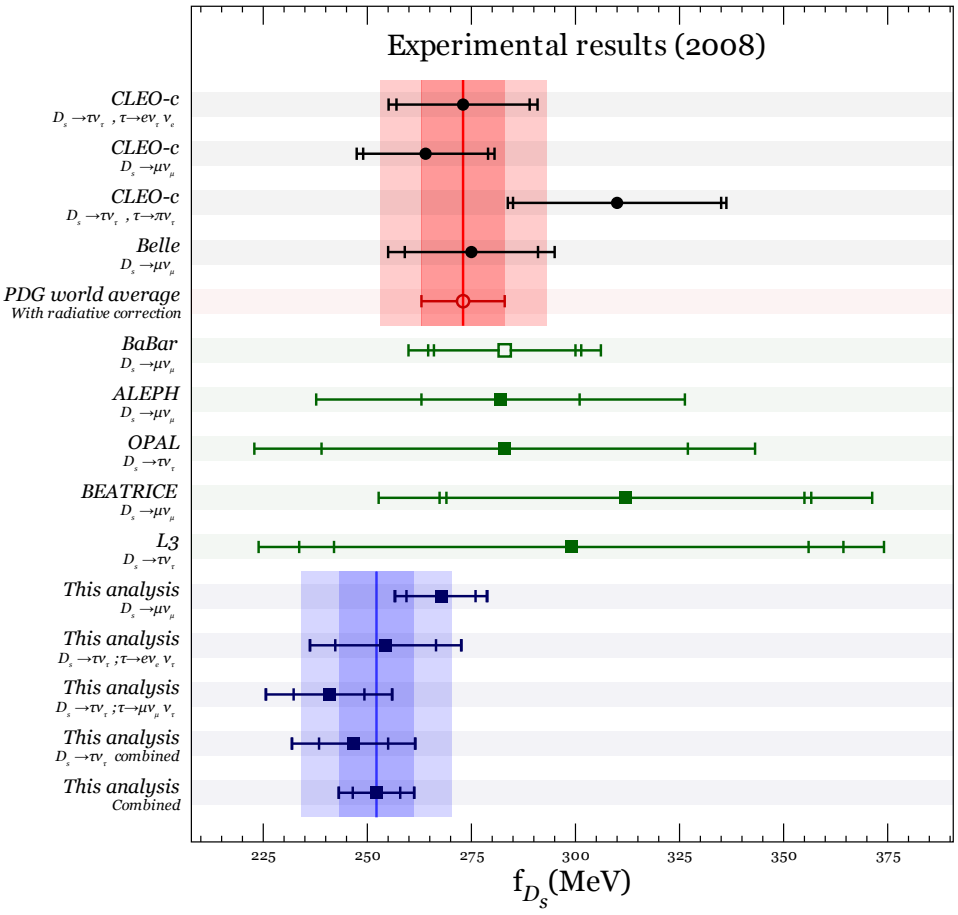

Figure 11.1: Comparison of sensitivities for f_{D_s} for different experiments. The Particle Data Group world average is shown in the vertical pink bands. The inner band indicates one standard deviation around the mean value and the outer band indicates two standard deviations around the mean value. Measurements contributing to the world average are shown with solid circles. The world average is shown with a hollow circle. Other measurements are shown with squares. The previous BaBar measurement (which this result supercedes) is shown with a hollow square. The first error bars show the statistical uncertainties for the measurements. The second error bars show the statistical and systematic uncertainties, added in quadrature for the measurements. The third error bars for results other than those presented in this thesis (where present) show the statistical, systematic and normalisation uncertainties, added in quadrature for the measurements. The results presented in this thesis are shown with blue squares, with the blue bands delimiting two standard deviations around the mean value. (Ecklund 2008) (Artuso 2007) (Widhalm 2008) (Aubert 2007) (Heister 2002) (Abbiendi 2001) (Alexandrov 2000) (Acciarri 1997)

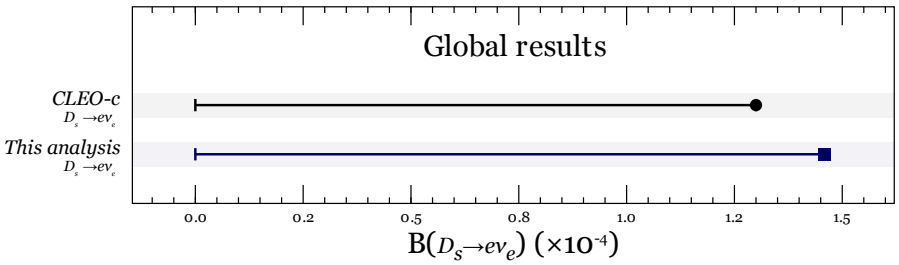

Figure 11.2: Comparison of sensitivities for $\mathcal{B}(D_s \to e\nu_e)$ for different experiments. Measurements contributing to the world average are shown with solid circles. The result presented in this thesis is shown with a blue square. (Pedlar 2007)

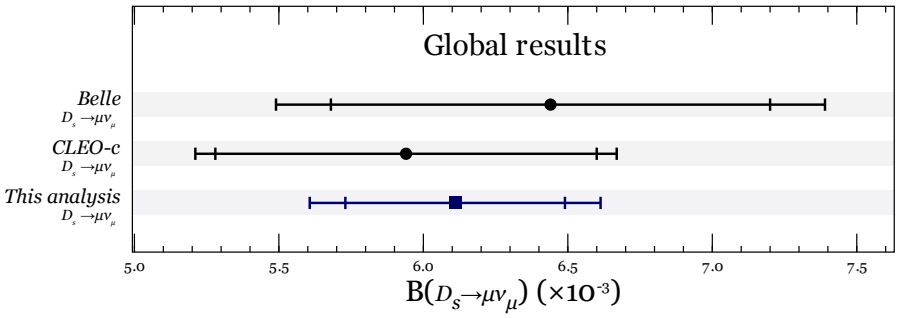

Figure 11.3: Comparison of sensitivities for $\mathcal{B}(D_s \to e\nu_e)$ for different experiments. Measurements contributing to the world average are shown with solid circles. The first error bars show the statistical uncertainties for the measurements. The second error bars show the statistical and systematic uncertainties, added in quadrature for the measurements. The result presented in this thesis is shown with a blue square. (Artuso 2007) (Widhalm 2008)

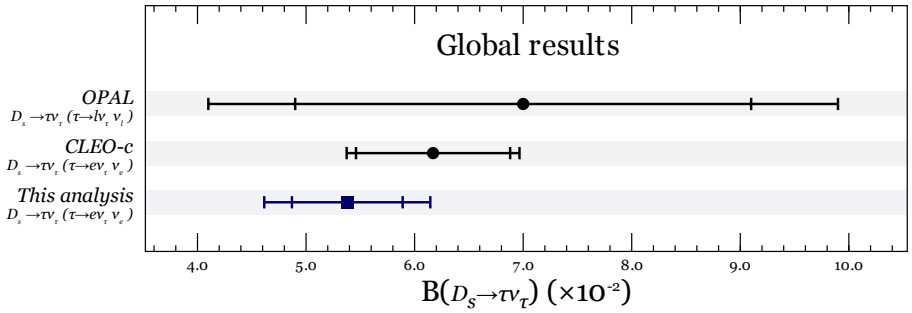

Figure 11.4: Comparison of sensitivities for $\mathcal{B}(D_s \to \tau\nu_\tau; \tau \to e\nu_e\nu_\tau)$ for different experiments. Measurements contributing to the world average are shown with solid circles. The first error bars show the statistical uncertainties for the measurements. The second error bars show the statistical and systematic uncertainties, added in quadrature for the measurements. The result presented in this thesis is shown with a blue square. (Abbiendi 2001) (Pedlar 2007)

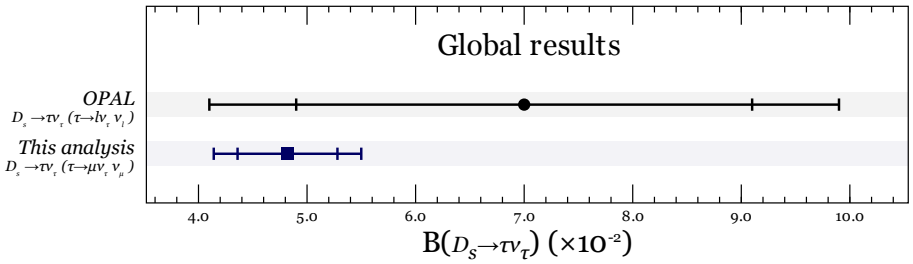

Figure 11.5: Comparison of sensitivities for $\mathcal{B}(D_s \to \tau\nu_\tau; \tau \to \mu\nu_\mu\nu_\tau)$ for different experiments. Measurements contributing to the world average are shown with solid circles. The first error bars show the statistical uncertainties for the measurements. The second error bars show the statistical and systematic uncertainties, added in quadrature for the measurements. The result presented in this thesis is shown with a blue square. (Abbiendi 2001)

11.3 Comparison with theory

The results presented in this thesis appear to agree with unquenched-lattice quantum chromodynamical expectations, as shown in figure 11.6. This indicates a downward movement of the world average towards the most current and precise unquenched-lattice quantum chromodynamical expectation. However this may not resolve the disagreement between this expectation and the world average, as the uncertainties will also decrease.

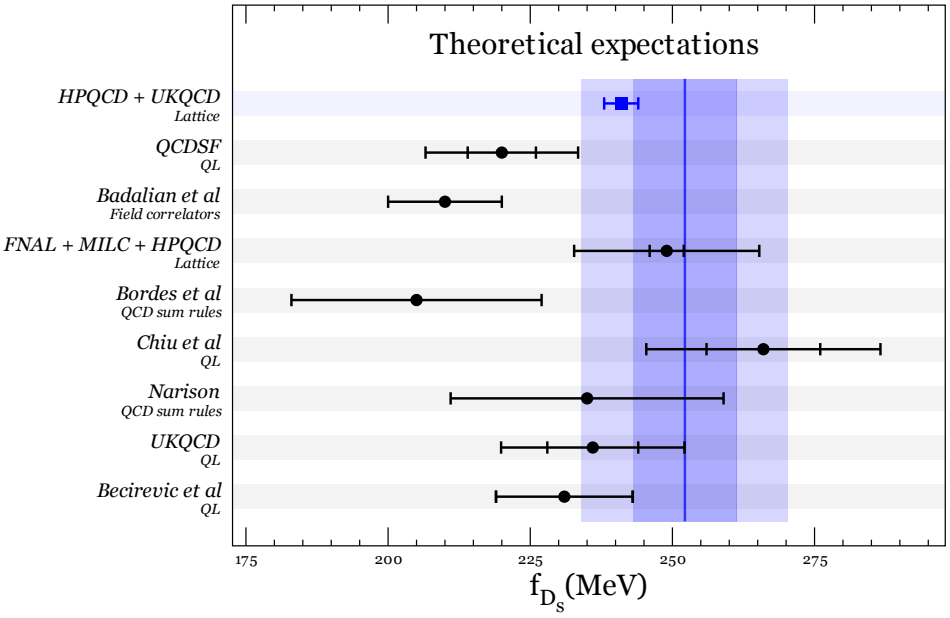

Figure 11.6: Comparison of these results to current theoretical expectations for the value of f_{D_s} from various collaborations. The average of these results is shown in the vertical blue bands. The inner band indicates one standard deviation around the mean value and the outer band indicates two standard deviations around the mean value. Older expectations are shown with circles. The expectation shown with a blue square denotes a recent result from Follana *et al*, which agress with these results to within one standard deviation. (Follana 2007) (Khan 2007) (Badalian 2007) (Aubin 2005) (Bordes 2005) (Chiu 2005) (Narison 2000) (Lellouch & Lin 2001) (Becirevic 1999)

11.4 f_{D_s} in context

The necessity of a precise measurement of f_{D_s} is motivated by many considerations. With experiments such as BaBar, Belle and LHCb examining CP violating parameters of the Standard Model it is important to determine the Cabibbo-Kobayashi-Maskawa matrix elements with high precision. However such measurements require good knowledge of the internal structure of hadrons, and in particular B mesons. Poor understanding of the quantum chromodynamical processes which take place in such mesons will continue to limit knowledge of these CP violating processes. Therefore it seems unlikely that an experimental determination of f_{D_s} alone will be sufficient to resolve the disagreement between theory and experiment, or to explain from where the difficulties in current theories arise. Further work should be carried out on additional probes, such as the leptonic decays of the $D^{\pm}$ meson. The leptonic decays of charm mesons are theoretically well constrained decay modes which offer an excellent opportunity to probe understanding of mesons.

With the Large Hadron Collider starting to acquire data it is important to constrain new physics. In the near future BaBar and similar experiments will be able to provide stringent limits on new physics beyond the Standard Model which will inform searches and discoveries at the Large Hadron Collider.

11.5 Summary

This thesis has presented competitive limits and measurements of the branching fractions $\mathcal{B}(D_s \to \ell\nu_\ell)$. The average value of f_{D_s} is more sensitive than the current world average, providing the world's most precise measurements of $\mathcal{B}(D_s \to \mu\nu_\mu)$, $\mathcal{B}(D_s \to \tau\nu_\tau)$, and f_{D_s}. This value also shifts the world average lower, decreasing the disagreement between experiment and theory.

References

Abbiendi, G. *et al.* 2001. "Measurement of the Branching Ratio for $D_s \to \tau\nu_\tau$ Decays." *Physics Letters B* 516(236). OPAL Collaboration.

Acciarri, M. *et al.* 1997. "Measurement of $D_s^- \to \tau^-\bar{\nu}_\tau$ and a new limit for $B^- \to \tau^-\bar{\nu}_\tau$." *Physics Letters B* 396:327–337. L3 Collaboration.

Alexandrov, Y. *et al.* 2000. "Measurement of the $D_s \to \mu\nu_\mu$ branching fraction and of the D_s decay constant." *Physics Letters B* 478:31–38. BEATRICE Collaboration.

Allison, J. *et al.* 2006. "`GEANT4` Developments and Applications." *IEEE Transactions on Nuclear Science* 53(1):270–278.

Amsler, C. *et al.* 2008*a*. "Decay constants of charged pseudoscalar mesons." *Physics Letters B* 667(1).

Amsler, C. *et al.* 2008*b*. "Particle Data Group." *Physics Letters B667, 1* .

Amsler, C. *et al.* 2008*c*. "Pentaquarks." *Physics Letters B* 667(1).

Anderson, C. 1933. "The Positive Electron." *Physics Review* 43(6):491–494.

Artuso, M. *et al.* 2007. "Measurement of the decay constant f_{D_s} using $D_s^+ \to \ell^\nu$." *Physics Review Letters* 99(071802). CLEO Collaboration.

Aubert, B. *et al.* 2002. "The BaBar detector." *Nuclear Instruments and Methods in Physics Research* A(479):1–116.

Aubert, B. *et al.* 2006. "A Search for $B^+ \to \tau^+\nu$ Recoiling against $B^- \to D^0\ell^-\bar{\nu}X$." *International Conference on High-Energy Physics* .

Aubert, B. *et al.* 2007. "Measurement of the Pseudoscalar Decay Constant f_{D_s} Using Charm-Tagged Events in e^+e^- Collisions at $\sqrt{s} = 10.58\,\mathrm{GeV}$." *Physics Review Letters* 98(141801). BaBar Collaboration.

Aubin, C. *et al.* 2005. "Charmed-Meson Decay Constants in Three-Flavor Lattice QCD." *Physics Review Letters* 95(122002). MILC Collaboration.

Badalian, A. *et al.* 2007. "Decay constants of the heavy-light mesons from the field correlator method." *Physics Review D* 75(116001).

Bauer, J. 2003. "Absolute Energy Calibration with the Neutron-Activated Liquid-Source System at BaBar's $CsI(Tl)$ Calorimeter." 50^{th} *IEEE Nuclear Science Symposium and Medical Imaging Conference* . BaBar Collaboration electromagnetic calorimeter group.

Becirevic, D. *et al.* 1999. "Nonperturbatively improved heavy-light mesons: Masses and decay constants." *Physics Review D* 60(174501).

Benitez, J. 2010. "Personal communication.".

Bethe, H. 1930. "Zur Theorie des Durchgangs schneller Korpuskularstrahlen durch Materie." *Annalen der Physik* 397:325–400.

Bogdan, A. *et al.* 2008. "Accumulating evidence for nonstandard leptonic decays of D_s mesons." *Physics Review Letters* 100(241802).

Bona, M. *et al.* 2007. "SuperB: A High-Luminosity Asymmetric e+ e- Super Flavor Factory. Conceptual Design Report." *SLAC* R(856).

Bordes, J. *et al.* 2005. "D and D_s decay constants from QCD duality at three loops." *JHEP* 0511(014).

Boutigny, D. *et al.* 2003. "BaBar Technical Design Report.".

Brooks, M. *et al.* 1999. "New limit for the family number nonconserving decay $\mu^+ \rightarrow^+ \gamma$." *Physics Review Letters* 83:1521–1524.

Brun, R. *et al.* 2010. "ROOT — A Data Analysis Framework.". `http://root.cern.ch/drupal/`.

Camanzi, B. *et al.* 2001. "The dose mapping system for the electromagnetic calorimeter of the BaBar experiment at SLAC." *Nuclear Instruments and Methods in Physics Research* A(457):476–486.

Chadwick, J. 1932. "Possible Existence of a Neutron." *Nature p. 312 Feb. 27* .

Charles, J. *et al.* 2005. "CKMfitter Group." *European Physical Journal* C(41):1–131. [hep-ph/0406184].

Chiu, T. *et al.* 2005. "Pseudoscalar decay constants f_D and f_{D_s} in lattice QCD with exact chiral symmetry." *Physics Letters B* 624(31-38).

Cowan, C. *et al.* 1956. "Detection of the Free Neutrino: a Confirmation." *Science* 124(3212).

Dirac, P. 1928. "The Quantum Theory of the Electron." *Proc.R.Soc.Lond.* A117 610-624; ibid(A118):351–361.

Doršner, I. *et al.* 2009. "Can scale leptoquarks explain the f_{D_s} puzzle?" *Physics Letters B* (682):67–73.

Ecklund, K. *et al.* 2008. "Measurement of the Absolute Branching Fraction of $D_s^+ \to \tau^+\nu_\tau$ Decay." *Physics Review Letters* 100(161801). CLEO Collaboration.

Feynman, R. 1969. "Proceedings of the 3rd Topical Conference on High Energy Collision of Hadrons." *Stony Brook,* .

Follana, E. *et al.* 2007. "High Precision determination of the π, K, D and D_s decay constants from lattice QCD." *Physics Review Letters* 200(062002). HPQCD and UKQCD Collaborations.

Harrison, P. *et al.* 1999. "The BaBar Physics Book." *SLAC* R(504).

Hayasaka, K. *et al.* 2006. "New search for $\tau \to \mu\gamma$ and $\tau \to e\gamma$ decays at Belle." *Physics Letters B* 666.

Hayasaka, K. *et al.* 2008. "Search for lepton flavor violation in the decay $\tau \to e\gamma$ decays." *Physics Review Letters* 96:16–22.

Heister, A. *et al.* 2002. "Leptonic decays of the D_s meson." *Physics Letters B* 528(1). ALEPH Collaboration.

Holmes-Siedle, A. *et al.* 1986. "RADFET: A review of the use of metal-oxide-silicon devices as integrating dosimeters." *International Journal of Radiation Applications and Instrumentation. Part C. Radiation Physics and Chemistry* 28(2):235–244.

Hou, W. 1993. "Enhanced charged Higgs boson effects in $B^- \to \tau\bar{\nu}, \mu\bar{\nu}$ and $b \to \tau\bar{\nu} + X$." *Physics Review D* 48(5).

Hrynova, T. 2003. "EMC radiation damage studies." *BaBar-PEP-II Background Workshop* . BaBar Collaboration.

Jackson, G. 2010. "Personal communication.".

Kalman, R. 1960. "A New Approach to Linear Filtering and Prediction Problems." *Transactions of the ASME - Journal of Basic Engineering* 82(Series D):35–45.

Khan, A. *et al.* 2005. "The Radiation Dose Measurement System for the BaBar Elecromagnetic Calorimeter." *Nuclear Science Symposium Conference Record IEEE* Volume I.

Khan, A. *et al* Ali. 2007. "Decay constants of charm and beauty pseudoscalar heavy-light mesons on fine lattices." *Physics Letters B* 652(150). MILC Collaboration.

Kobayashi, M. & T. Maskawa. 1973. "CP Violation in the Renormalizable Theory of Weak Interaction." *Progress of Theoretical Physics* 49:652–657.

Kobel, M. *et al.* 1992. "Measurement of the decay of the $\Upsilon(1S)$ and $\Upsilon(2S)$ resonances to muon pairs." *Zeitschrift fur Physik* C53.

Lee, T. 1956. "Question of Parity Conservation in Weak Interactions." *Physics Review* 104:254–258.

Lellouch, L. & C. Lin. 2001. "Standard model matrix elements for neutral B-meson mixing and associated decay constants." *Physics Review D* 64(094501). UKQCD Collaboration.

Narison, S. 2000. "Light and heavy quark masses, Flavour breaking of chiral condensates, Meson weak leptonic decay constants in QCD." *[hep-ph/0202200]* .

Narsky, I. 2005. "StatPatternRecognition: A C++ Package for Statistical Analysis of High Energy Physics Data." *arXiv:physics/0507143v1 [physics.data-an]* .

Narsky, I. 2006. "StatPatternRecognition.". `http://statpatrec.sourceforge.net/`.

Noether, E. 1918. "Invariante Variationsprobleme." *Math-phys.* Klasse:235–257.

Pedlar, T. *et al.* 2007. "Measurement of $\mathcal{B}(D_s^+ \to \ell^+\nu)$ and the decay constant $f_{D_s}^+$." *Physics Review D* 76(072002). CLEO Collaboration.

Rutherford, E. 1919. "Collisions of alpha Particles with Light Atoms. IV. An Anomalous Effect in Nitrogen'." *The London, Edinburgh and Dublin Philosophical Magazine and Journal of Science 6th series* 37(581).

Seeman, J. 2008. "Last year of PEP-II B-factory operation." *Proceedings of EPAC08 Genoa* .

Street, J. *et al.* 1937. "New Evidence for the Existence of a Particle Intermediate Between the Proton and Electron." *Physics Review* 52(1003).

The BaBar Collaboration. 2010. `http://www.slac.stanford.edu/BFROOT`.

Thomson, J.J. 1897. "Cathode Rays." *Philosophical Magazine* 44(293).

Verkerke, W. & D. Kirby. 2006. "The Roofit Toolkit for Data Modeling.". `http://roofit.sourceforge.net/`.

Widhalm, L. *et al.* 2008. "Measurement of $\mathcal{B}(D_s^+ \to \mu^+\nu_\mu)$." *Physics Review Letters* 100(241801). Belle Collaboration.

Wolfenstein, L. 1983. "Parametrization of the Kobayashi-Maskawa Matrix." *Physics Review Letters* 51(1945).

Wu, T. *et al.* 1964. "Phenomenological Analysis of Violation of CP Invariance in Decay of K^0 and $\bar{K}^0$." *Physics Review Letters* 13:380–385.